STATISTICAL MODELING AND INFERENCE IN BIOLOGICAL DATA: FROM BRAIN NETWORKS TO VIRUS HETEROGENEITY

A Dissertation

Presented to the Faculty of the Graduate School

of Cornell University

in Partial Fulfillment of the Requirements for the Degree of

Doctor of Philosophy

by

Nan Xu

May 2017

STATISTICAL MODELING AND INFERENCE IN BIOLOGICAL DATA:
FROM BRAIN NETWORKS TO VIRUS HETEROGENEITY

Nan Xu, Ph.D.
Cornell University 2017

In my dissertation, advanced theoretical approaches and algorithms are developed to investigate the two primary applications, (1) functional MRI (fMRI) and (2) structural virology. These new techniques provide novel insights in (i) brain functions and (ii) the heterogeneity of virus particles.

Resting-state functional magnetic resonance imaging (rs-fMRI) examines the low frequency spontaneous fluctuations in blood oxygen level dependent (BOLD) signals. It is widely used to investigate the brain activity at resting state, which is the state consuming the majority brain energy metabolism. Over the past two decades, the established correlation method has been successful in delineating the large-scale brain networks. However, it cannot characterize the spatial and temporal causal relations in these networks. Other methods provide some information of the causal relations, but are not successful at detecting the underlying networks.

To overcome these limitations, we introduce a new concept named prediction correlation (p-correlation) to replace the traditional methods for estimating brain networks from rs-fMRI. In particular, the correlation between two BOLD signals is replaced by a correlation between one BOLD signal and a prediction of this signal via a causal system driven by another BOLD signal. The advantages of the p-correlation approach include that (1) it is a generalization of correlation and is able to identify previously characterized large-scale brain networks, and

(2) it determines more reliable patterns of directed network connectivity, and (3) it can estimate the duration of directed interactions in brain networks.

By using p-correlation, for the first time, we are able to characterize the most and the least rapid information propagations in brain networks. For example, we found that the most rapid information flows are propagated from all other regions to the memory regions in human brain. This discovery agrees with the current understanding of brain functions at resting state, and provides novel insight into brain functions from a different dimension (e.g., the temporal scale).

In addition, a realistic simulator for BOLD signals is developed with customized selection on mathematical models of brain activity and parameters. As a result, the new simulator simplified and enhanced the existing simulators by expanding customer options, especially allowing customers to integrate different components from different simulators into a single calculation.

The structure of virus particles is central to understanding their function. Cryo electron microscopy (cryo EM) is a major experimental method for determining structure by measuring noisy randomly-oriented projection images, one image from each of 103-106 virus particles, which are then combined by reconstruction algorithms. Because each particle is individually imaged, unlike in x-ray crystallography, it is possible to gain information about the continuous heterogeneity, e.g., flexibility, of the virus particle. Symmetry is an important aspect of virus particles and our work has focused on particles with polyhedral symmetry which includes symmetry of tetrahedral, octahedral and icosahedral point groups.

Traditional methods of characterizing heterogeneity assume that each particle has the full symmetry. This is probably not realistic. We have generalized this viewpoint so that individual particles lack symmetry, but the first and sec-

ond order statistics of the particles have symmetry. In other words, the symmetry appears in the expectation and the covariance, rather than in each realization, of the random process.

We represent the electron scattering intensity of the virus as a linear combination of basis functions where the coefficients are random variables. First, we derived and computed real-valued vector basis functions for square integrable functions on the surface of the sphere in 3-D where each vector basis function transforms as one of the irreducible representations of the point group symmetry. In particular, a new theorem in group representation theory was proven to guarantee the existence of such basis functions. Second, we derived conditions on the mean vector and covariance matrix of the coefficients that multiply the basis functions such that the linear combination of basis functions has the desired symmetry properties. Using this approach, we have been able to eliminate long-standing distortions in heterogeneity calculations associated with symmetry axes and demonstrate for the first time the space-varying anisotropy of the fluctuations in the virus' electron scattering intensity.

BIOGRAPHICAL SKETCH

Nan Xu was born in Beijing, China. She is currently a sixth year Ph.D. student in School of Electrical and Computer Engineering with a minor in Applied Mathematics and a minor in Cognitive Neuroscience at Cornell University. Nan received her Master of Science degree in May 2015. Before joining Cornell, she received double Bachelor's degrees in Electrical and Computer Engineering (BS) and Mathematics (BA) with a minor in Music at the University of Rochester in Rochester NY.

Nan had been interested in a broad research topics, including percolation theory, wireless sensor networks, VLSI circuits test algorithms, group representation theory, etc. Nan's current research interests are in statistical modeling and inference in biological data. Advised by Prof. Peter C. Doerschuk, she is investigating two primary applications: brain network estimation and reconstruction of the statistical characteristics of ensembles of heterogeneous virus particles.

This thesis is dedicated to my parents and my husband for all of their companion, support and sacrifice.

ACKNOWLEDGEMENTS

I am grateful to Prof. Peter C. Doerschuk for initiating these two great and interesting research projects. Especially, my project of studying virus heterogeneity is established on Peter's knowledge and experiences in viruses accumulated in the past twenty years. Under Peter's guidance, I became fascinated that a biological phenomenon can be explored from several different dimensions, which includes solving fundamental mathematical problems to interpret phenomenon, establishing statistical models to integrate mathematical properties, and realizing these models through algorithmic tools, and the most important, bringing novel insights into biological facts. Peter is the person who led me to bring abstract mathematics to the real world. I am also thankful to Peter for his concrete suggestions on presentations and career establishment.

I am also grateful to Prof. R Nathan Spreng for working with me and introducing me to his field of brain science. Over the past four years, his guidance and encouragement and his intelligent insights in my work have been critical for my discovery of the brain functions. I thank my committee member, Prof. John (Jack) E. Johnson, for introducing me to his world of structural virology, and teaching me everything I know about viruses. I thank my committee member, Prof. Lang Tong, for his instruction on statistical signal processing. The knowledge of signal estimation and detection which I learned from him had been the fundamental of all my research work. I am also thankful for his thoughtful discussions and insightful advices on the career establishment.

I am thankful to my collaborators Prof. David Veesler (University of Washington) and Prof. Reza Khayat (The City College of New York) for their virus data and the helpful discussions. I am also thankful to Prof. Mert Sabuncu for his critiques and suggestions on my discovery of brain science.

I am especially grateful to Prof. Dan Mihai Barbasch for his willingness of discussing my group theory problem with me and leading me to the right direction of solving my representation theory problem as well as for his critiques on my applied math paper. I am also grateful to my friends Dr. Hung Tran and Dr. Chenxi Wu from Department of Mathematics for their helpful discussions on group theory. Hung is the person who led me to talk to everyone in Math Department about my problem until we finally reached Dan. I would like to thank my friend Dr. Chaoxu Tong from ORIE for his helpful discussion on linear algebra, especially on finding a desired basis of a random matrix. I would also like to thank my best friend Ms. Yuguang Gao from ECE for her consistent support, as well as her critiques on writing the applied math paper.

I thank the alumni as well as the current member of the Doerschuk Lab, in particular, Dr. Yibin Zheng, Dr. Zhye Yin, Dr. Kang Wang, Dr. Yili Zheng, Dr. Qiu Wang and Ms. Yunye Gong. I learned so much from all of them, either before they graduated from the lab, or afterwards through the works they have accomplished. I thank the members of the Spreng Lab, in particular, Dr. Michael Ferguson, Ms. Elizabeth DuPre, Ms. Anne Laurita, Ms. Amber Lockrow, Ms. Laetitia Mwilambwe-Tshilobo and Ms. Roni Setton, for their critques on my discovery of brain functions and presentations.

Moreover, I am full of gratitude to my husband, Dr. Andy Sun, for his sacrifice and all his support on my PhD work and life. His critiques on an early version of my applied math paper motivated me to explore further in representation theory, which inspired me to develop the current Lemma 6 in Section 5.5. My discussion with him helped me make the whole story of my applied math paper more complete with no logic holes. In addition, his sharp comments and brilliant suggestions have been very helpful for me to improve my research as

well as my presentations.

Finally, I thank my parents and my friends for all of their support and encouragement in my whole PhD life. I thank my parents for their patience of listening to all of my problems and their willingness to understand and to make comments on my research from a different perspective. The experience of explaining my work to them has inspired me to present my research work in various ways. I thank Dr. Xinrui Pan, who has been my best friend since college, for her consistent companion and encouragement. Xinrui came to Cornell law school as a visiting scholar in my fourth year of Ph.D. study, when I was having difficulty with the group theory problem. Xinrui's absolute trust in my research ability, and her encouragement and companionship while studying in the law school library, inspired me to finally solve the most critical piece of the group representation theory problem. I thank Ms. Fumi-san, the owner of cafe pacific restaurant, for all her care and encouragement. Fumi-san not only provided me the warmest food even after shutting down the kitchen at 1am, but also gave me plenty good advices in handling all kinds of life crises. From her guidance, I learned how to be perceptive, and I gained the strength to handle all issues and difficulties in my Ph.D. work and life.

TABLE OF CONTENTS

LIST OF TABLES

LIST OF FIGURES

CHAPTER 1

INTRODUCTION

Statistical modeling has been an important technique to make inference in biological data. In this dissertation, two different biological objects are investigated: human brain (Chapter 2–4) and virus (Chapter 5–7). Specifically, new theory and algorithms are developed to investigate the two primary applications, (1) functional MRI (fMRI) (Chapter 2), and (2) structural virology (Chapter 5–6). With the use of biological data, novel insights in (i) brain functions (Chapter 3) and (ii) the functions of virus particles (Chapter 7).

1.1 Advances in functional brain networks analysis

Resting-state functional magnetic resonance imaging (rs-fMRI), which examines the low frequency spontaneous fluctuations in blood oxygen level dependent (BOLD) signals [15], is widely used to investigate the brain activity at resting state. Resting-state brain activity persistently supports the neuronal signaling at the resting state, and consumes the majority brain energy metabolism in contrast to task-related brain activities [26].

Network functional connectivity is often estimated by calculating the time-series correlation between BOLD signals from different regions of interest. Using standard correlation, substantial progress has been made in delineating large-scale functional brain networks, which are the brain networks that exhibit correlated fluctuations and provide indirect information about structural connectivity patterns that define brain systems (e.g. [15, 141, 97]). However, it is also noticed by researchers that standard correlation cannot characterize the

direction of information flow between regions, which is called the "effective connectivity" in brain networks.

In Chapter 2, we introduce a novel concept, prediction correlation (p-correlation), to estimate both functional and effective connectivity from rs-fMRI. In this new statistical measure, the correlation between two BOLD signals is replaced by a correlation between one BOLD signal and a prediction of this signal via a causal system driven by another BOLD signal. Three validations are shown: (1) Prediction correlation performed well on simulated data where the ground truth was known, and outperformed four other methods. (2) On simulated data designed to display the "common driver" problem, prediction correlation did not introduce false connections between non-interacting driven ROIs. (3) On experimental data, prediction correlation recovered the previously identified network organization of human brain. Prediction correlation scales well to work with hundreds of ROIs, enabling it to assess whole brain interregional connectivity at the single subject level. These results provide an initial validation that prediction correlation can capture the direction of information flow and estimate the duration of extended temporal delays in information flow between regions of interest based on BOLD signal. This approach not only maintains the high sensitivity to network connectivity provided by the correlation analysis, but also performs accurately in the estimation of causal information flow in the brain.

In Chapter 3, p-correlation is used to investigate the spatial and temporal causal interactions between regions in the resting-state brain networks. For the first time, we are able to characterize the most and least rapid information propagations in brain networks. In particular, a more rapid information flow has a

shorter duration. Our discovery in the resting brain includes that (1) the least rapid information flows are discovered in the visual, the motor and the attention brain systems, and (2) the most rapid information flows are dominated by the activity that the medial temporal lobe collects information from the cortex, and (3) a ranking of the average duration of information flow from the well-known resting state functional networks is determined, which suggests that the frontal parietal, the limbic, and the default networks propagate information more rapidly than the others. These results agree with the current understanding of brain functions at resting-state, and provide novel insights in brain functions from a different dimension (e.g., the temporal scale).

In Chapter 4, a realistic simulator for BOLD signals is developed with customized selection on several well recognized mathematical models for brain activity. The new simulator simplified the existing simulators for neuron and BOLD signals, and enhanced them by expanding customer options, especially allowing customers to integrate different components from different simulators into a single calculation. simulators into a single calculation.

1.2 Advances in structural virology

In virology, determining the structure of the virus particles is a fundamental problem for understanding a virus, as the structure determines the functions of a virus particle, e.g., being infectious or not. A large class of plant and animal viruses is called "spherical" viruses, in which the particle has a shell of protein, called a "capsid", surrounding a cavity containing the viral genome. Typical sizes and molecular weights of the virus particles are 10^2–10^3 Å and 10

MDa. The geometry of capsid of these spherical viruses is important to their lifecycles. Single-particle cryo electron microscopy (cryo EM) [11, 24, 23], which has become an important technique for determining the geometry of a particle, leads to 3-D image reconstruction problems for these biological nano-machines Specifically, $10^3 - 10^6$ virus particles are flash frozen to cryogenic temperatures and imaged. Each image is basically a highly-noisy (SNR < 0.1) 2-D projection of the 3-D electron scattering intensity distribution of the particle. Only one such image can be taken per particle and its projection orientation is random. Therefore, the information from many such images is fused to compute a 3-D reconstruction [66].

Symmetry is sometimes an important feature of a biological object. The capsid of spherical virus particles, in the most common case, exhibits rotational symmetry of a platonic solid [29]. In cryo-electron microscopy, the 3-D structure of each virus particle is characterized by the 3-D electron scattering intensity function, denoted by $\rho(\cdot)$. Standard reconstruction approaches [36, 142, 113, 77] assume that the virus particles of the same type[1] are identical. An improved reconstruction method introduced in [133, 148] assumes that particle are different from each other (for example, due to the inherent flexibility of such a large molecular complex) but they all obey the same symmetry.

In contrast to this previous work, we consider a more realistic and sophisticated view: particles are different and it is the *statistics* of the ensemble of all particles that obey the symmetry not the individual particles. In particular, the mean and covariance of the 3-D electron scattering intensity distribution of the

[1] In biological applications, they are called particles in the same class based on the stage of their maturation processes.

particle are invariant under rotations [137]:

$$\bar{\rho}(R_g^{-1}\mathbf{x}) = \bar{\rho}(\mathbf{x}) \text{ and } C_\rho(R_g^{-1}\mathbf{x}_1, R_g^{-1}\mathbf{x}_2) = C_\rho(\mathbf{x}_1, \mathbf{x}_2), \tag{1.1}$$

where $\bar{\rho}(\cdot)$ is the mean function and $C_\rho(\cdot,\cdot)$ is the covariance function of the electron scattering intensity $\rho(\cdot)$, $R_g \in \mathbb{R}^{3\times3}$ is the gth rotation matrix of certain symmetry group, and $\mathbf{x}, \mathbf{x}_1, \mathbf{x}_2 \in \mathbb{R}^3$ are real-space coordinates. In the 3D reality, each particle can be described as a linear combination of basis functions where the weights in the linear combination are Gaussian random variables [133, 148]:

$$\rho(\mathbf{x}) = \sum_\zeta F_\zeta(\mathbf{x}) c_\zeta \tag{1.2}$$

where $F_\zeta(\mathbf{x})$ is the basis function and c_ζ is the weight. Because $\rho(\cdot)$ is real, it is convenient to have real-valued basis functions and weights. To describe the situation in which particles have non-symmetric structures but symmetric statistics, the basis functions and the weights with special properties are required.

In Chapter 5, a novel methodology based on a group-theoretic approach is developed to generate the appropriate basis functions. Basis functions which are invariant under the operations of a rotational polyhedral group G are able to describe any 3-D object which exhibits the rotational symmetry of the corresponding Platonic solid. In particular, they are sufficient to describe the situation assumed in the previous reconstruction methods. However, in order to characterize the spatial statistics of an ensemble of objects in which each object is different but the statistics exhibit the symmetry, a larger set of basis functions is required. In particular, for each irreducible representation (irrep) of G, it is necessary to include basis functions that transform according to that irrep. This larger set of basis functions is a basis for square-integrable functions on the surface of the sphere in 3-D. Because the objects are real-valued, i.e., $\rho(\cdot) \in \mathbb{R}$, it is convenient to have real-valued basis functions. In this Chapter, the existence of

such real-valued bases is proven and an algorithm for their computation is provided for the icosahedral I and the octahedral O symmetries. Furthermore, it is proven that such a real-valued basis cannot exist for the tetrahedral T symmetry because some irreps of T are essentially complex. The importance of these basis functions to computations in single-particle cryo electron microscopy is described.

In Chapter 6, a new reconstruction approach is developed to incorporate the realistic assumption of symmetrical statistics into expectation-maximization algorithms for the maximum likelihood solution of $\bar{\rho}$ and C_ρ in Eq. 1.1. In particular, constraints on the weights (c_ζ in Eq. 1.2) are derived based on Eq. 1.1 through tools in group theory such as the Schur's Lemma. Applying the appropriate basis functions, a maximum likelihood (ML) reconstruction algorithm is used to estimate the constrained weights c_ζ, which is a generalization of classical ML Gaussian mixture parameter estimation [104]. This new reconstruction approach is called "heterogeneous reconstruction with symmetrical statistics" (HRSS). HRSS is demonstrated on bacteriophage HK97 and is contrasted with former algorithms [148, 133]. Reconstruction results show that HRSS provides estimates that make more biological sense than former algorithms. In particular, the variance map of $\rho(\mathbf{x})$ computed by HRSS eliminates the artificial spikes laid on the symmetry axes of the platonic solids, which has been a well-known problem existed in all the previous reconstruction solutions of spherical virus particles [82, p. 173].

In Chapter 7, this new reconstruction algorithm HRSS is used to investigate the heterogeneity of virus structures for the maturation-intermediates, Prohead I of bacteriophage HK97 with the viral protease packaged ($\text{PhI}^{\text{Pro+}}$) and with-

out (PhI^{Pro-}). Through the realistic assumption of statistical symmetries on the ensemble of virus particles, HRSS enables analysis on both variance and covariance. For the first time, we are able to characterize how events on the inner surface of the capsid are related to the remainder of the capsid. The results are compared with the previous reconstruction solutions computed by former algorithms [51]. In the variance analysis, PhI^{Pro-} demonstrates a greater heterogeneity than PhI^{Pro+} which is consistent with the previous result [51]. The primary discovery includes that (1) the variance map displays a detailed annular structure agreeing with the biological structure of HK97 particles, and (2) the inner surface (disordered δ-domain) of the capsid actively interacts with the central core of DNA nucleic acid, and (3) the greatest heterogeneity of PhI^{Pro-} occurs between the disordered δ-domain and the central core of genome. In addition, through the covariance analysis, we numerically validate the transition in the orderedness of materials in different domains of the capsid. In particular, as the radius increases from the inner to the outer surface of the capsid, the structure of the protein in the capsid transits from a disordered form to an ordered form. This transition appears to be continuous along the radius. Furthermore, comparing to the rest of the particle, the selected regions in the capsid are strongly correlated to regions in the same annulus. These findings validate the annular structure in the capsid of a virus particle.

In summary, the thesis develops novel approaches to investigate the two different applications, fMRI and structural virology. In fMRI, a new statistical measure is proposed to replace the traditional methods for estimating brain networks, which overcomes the limitation of characterizing the causal information flows in brain networks and provides novel insights in brain functions. In structural virology, a realistic view on the ensemble of virus particles is pro-

posed. Two components are essential to describe such a realistic situation. 1) A complete set of real-valued basis functions are required to describe all possible heterogeneous objects in 3D real space. A new theorem in group representation theory is proven to guarantee the existence of such basis functions. 2) The weights of basis functions need to be constrained to realize the assumption of symmetrical statistics. The reconstruction solution is the statistics of the ensemble of virus particles. The new reconstruction algorithm developed eliminates the well-known problem in the existing reconstruction algorithms, and provides numerical validations for the hypothesis on the puzzling structure and functions of a biological mechanism in the nano world.

CHAPTER 2

INITIAL VALIDATION FOR THE ESTIMATION OF RESTING-STATE FMRI EFFECTIVE CONNECTIVITY BY A GENERALIZED CORRELATION APPROACH

2.1 Introduction

This chapter has been published in [140].

Resting-state functional MRI (rs-fMRI) has been widely used to study the intrinsic functional architecture of the human brain based on spontaneous oscillations of the blood oxygen level dependent (BOLD) signals [117, 15, 141, 97]. One fruitful approach has been to examine the correlations between rs-fMRI timeseries at pairs of regions of interest (ROIs) and use the correlations as a measure of connectivity strength between each pair [134, 118]. The correlation method, though simple, plays a fundamental role in evaluating functional connectivity in the human brain for both task-evoked networks [109, 26] and resting-state networks [58, 109, 98]. The relationships between correlation and the topological properties, including small-world organization, modular structure, and highly connected hubs, has been studied in [143]. However, the direction of information flow between pairs of ROIs and the causality of information flow cannot be derived from standard correlation methods. Reliable insight into the direction and causality of functional connections in the brain from BOLD signals would provide substantial breakthroughs in characterizing large-scale brain network dynamics.

The BOLD signal is an indirect and sluggish measure of neuronal activity.

Despite this, substantial insights have been gleaned by examining patterns of BOLD signals as proxies for functional connectivity in the brain, and these are consistent with more direct and invasive observations [39]. At every level of analysis, the brain demonstrates an organized network structure [14]. So, even though neuronal activation occurs on the millisecond time scale, organized and structured activation patterns are also observed on the level of seconds, which is within the range of BOLD signals and is important for understanding cognition. Causal information about the flow of information in the brain may be detected and estimated from the BOLD signals. It remains critical, however, to evaluate methods of investigation against ground truth simulation in order to validate these methods.

Numerous methods for estimating functional or effective connectivity [127, 43] have recently been evaluated against ground truth networks using simulated rs-fMRI data [117]. Functional connectivity can be quantified with a measure of statistical dependence such as correlation, whereas effective connectivity measures the directed causal influence [43]. In [117], performance of both types of methods across a range of measures was mixed. Standard and partial correlation excelled at detecting the presence of a connection. Other methods for estimating the direction of a connection varied from chance (Granger) to greater than 50% accuracy (Patel's Tau and pairwise LiNGAM). These results suggest that novel methods are needed to estimate directed connectivity from rs-fMRI data, particularly with a large number of ROIs, which are necessary for full coverage of cortical and sub-cortical areas in the human brain. In this paper, we introduce a new method, prediction correlation, to the neuroimaging community and provide an initial validation of the approach.

Methods for estimating functional connectivity can be oriented toward estimating a real number describing strength of connectivity, which might be quite small, versus estimating a binary connectivity, which is present or absent, with possibly the addition of a strength of connectivity, in the form of a real number, for the case where a connection is present. Correlation and prediction correlation, which is a generalization of correlation that we propose in this paper, are methods that estimate a real number that describe strength of connection. Subsequent processing can then be applied to remove week connections and/or organize the complete network into modular networks.

As is described in the following sections, testing on simulated rs-fMRI data with known ground-truth networks [117] demonstrates that prediction correlation is not only sensitive to detected network connections, as identified by standard correlation, but also achieves the highest accuracy on estimation of connection directionality among all approaches used in [117] (Section 2.3). In a "common driver" phenomena, when ROI 1 drives ROIs 2 and 3 but ROIs 2 and 3 do not directly interact, prediction correlation correctly detects strong 1→2 and 1→3 connections but not 2→3 or 3→2 connections (Section 2.4). Finally, extending [139], we demonstrate the robustness of this method on experimental data and that prediction correlation recovers previously identified brain network organization from experimental data (Section 2.5).

2.2 Prediction correlation

2.2.1 Fundamental method

In what follows, we describe a methodology for analyzing rs-fMRI data using a generalization of the well-established correlation approach, which is to correlate the timeseries at two ROIs. The generalization, denoted by "p-correlation" ("p" for "prediction") is to replace correlation between the BOLD timeseries at two ROIs by correlation between the BOLD timeseries at one ROI and a prediction of this timeseries. The prediction is the output of a mathematical dynamical system that is driven by the timeseries at the other ROI. More generally, the prediction could be based on several, spatially discrete, ROIs. In this paper, we focus on the case where only one other ROI is used. We assume that the dynamical system is linear and has finite memory and that the memory duration and parameters may be estimated from the BOLD timeseries. If the prediction of the timeseries is restricted to use only the current value of the timeseries that drives the dynamical system, then p-correlation is the same as standard correlation. Therefore p-correlation is a generalization of correlation. Features of p-correlation include (1) the ability to indicate the directionality of the interaction between two ROIs, (due to the fact that this prediction correlation is asymmetrical between two signals), and (2) the ability to evaluate the interaction based on casual information.

In the remainder of this section, we provide more detail on the p-correlation approach. Consider the ordered pair of ROIs (i, j) and let x_i (x_j) denote the rs-fMRI timeseries at the i^{th} (j^{th}) ROI. Both timeseries have duration N_x. The x_j

signal is predicted from the x_i signal by a linear time-invariant causal dynamical model with x_i as the input and the prediction $\hat{x}_{j|i}$ as the output. This model can be described by an impulse response, denoted $\mathbf{h}_{j|i}$, which is zero for negative times. We assume that the impulse response is of finite duration, with duration denoted by $N_{h_{j|i}}$. In summary,

$$\hat{x}_{j|i}[n] = \sum_{m=0}^{N_{\mathbf{h}_{j|i}}} \mathbf{h}_{j|i}[m] x_i[n-m]. \tag{2.1}$$

The basic approach to estimate the coefficients of $\mathbf{h}_{j|i}$ is to minimize the least squares cost

$$\mathcal{J}(\mathbf{h}_{j|i}) = \sum_{n=0}^{N_x-1} (x_j[n] - \hat{x}_{j|i}[n])^2. \tag{2.2}$$

We estimate the value of $N_{h_{j|i}}$ and the values of the impulse response at the same time by restating the least squares problem as a Gaussian maximum likelihood estimator (MLE) with a known variance for the measurement errors. The MLE allows a trade off of the accuracy of predicting the current data (i.e., minimizing $\mathcal{J}$), which is best done by large values of $N_{h_{j|i}}$, with the accuracy of predicting when presented with new data, which is best done by smaller values of $N_{h_{j|i}}$. There are several approaches to quantifying this trade off including Akaike information criteria (AIC) [4, 3, 121, 61, 62, 21], Bayesian information criteria (BIC) [114], restricted maximum likelihood (REML) [125, 94], minimum description length [105] and minimum message length [131]. We have focused on AIC because it leads to easily computed problem formulations (Eq. 2.3). AIC realizes this balancing goal by minimizing the sum of two terms, one term that characterizes the prediction error of the dynamic system through the least squares cost $\mathcal{J}(\mathbf{h}_{j|i})$ and a second term that depends on the durations $N_{h_{j|i}}$ and

N_x:

$$\text{AIC} = \begin{cases} N_x \log(\frac{2\pi}{N_x - N_{h_{j|i}}} \mathcal{J}(\mathbf{h}_{j|i})) + N_x + N_{h_{j|i}} & \text{if } N_x/N_{h_{j|i}} \geq 40 \\ N_x \log(\frac{2\pi}{N_x - N_{h_{j|i}}} \mathcal{J}(\mathbf{h}_{j|i})) + N_x^2 + \frac{N_{h_{j|i}}^2 - N_x + N_{h_{j|i}}}{N_x - N_{h_{j|i}} - 1} & \text{otherwise} \end{cases} . \quad (2.3)$$

Simultaneous minimization of Eq. 2.3 with respect to both $\mathbf{h}_{j|i}$, which occurs only in the $\mathcal{J}(\mathbf{h}_{j|i})$ term, and $N_{h_{j|i}}$ determines the duration and the value of the impulse response. The integer minimization over $N_{h_{j|i}}$ is computed by testing each value in a predetermined range of values, i.e., 1,2, ..., D seconds. Then, for each value of $N_{h_{j|i}}$, the minimization with respect to $\mathbf{h}_{j|i}$ involves only minimizing $\mathcal{J}(\mathbf{h}_{j|i})$. Since the dynamical system describing how x_i influences x_j is separate from the dynamical system describing how x_j influences x_i, the approach described here can lead to a directed rather than undirected graph of interactions between ROIs.

Once $\mathbf{h}_{j|i}$ and $N_{j|i}$ are estimated, the output of the dynamical system, which is the prediction $\hat{x}_{j|i}$, can be computed, and then the correlation of x_j and $\hat{x}_{j|i}$, which is the so-called p-correlation, denoted by $\rho_{j|i}$, can be computed. We use "correlation" and $\rho_{j,i}$ for the standard approach (i.e., the standard correlation between x_j and x_i).

Let the total number of ROIs be denoted by N_{ROI}. P-correlation is an asymmetric $N_{\text{ROI}} \times N_{\text{ROI}}$ matrix, where the asymmetry follows the $\rho_{j|i} \neq \rho_{i|j}$. Furthermore, p-correlation includes lags of the x_i signal since the dynamical system output at time n, $\hat{x}_{j|i}[n]$, depends on the input at its current and previous times, i.e., $x_i[n]$, $x_i[n-1]$, ..., $x_i[n - N_{h_{j|i}} + 1]$. If $N_{h_{j|i}} = 1$ (i.e., no lags) and $h_{j|i}[0] \geq 0$ then $\rho_{j|i}$ is the correlation between x_j and x_i so that $\rho_{j|i} = \rho_{j,i}$ and the approach of this paper exactly reduces to the standard approach. In Section 2.2.2, we describe a constraint such that $h_{j|i}[0] \geq 0$ is always achieved. The entire algorithm is shown

in Fig. 2.1. The Matlab software of implementing p-correlation is available upon request.

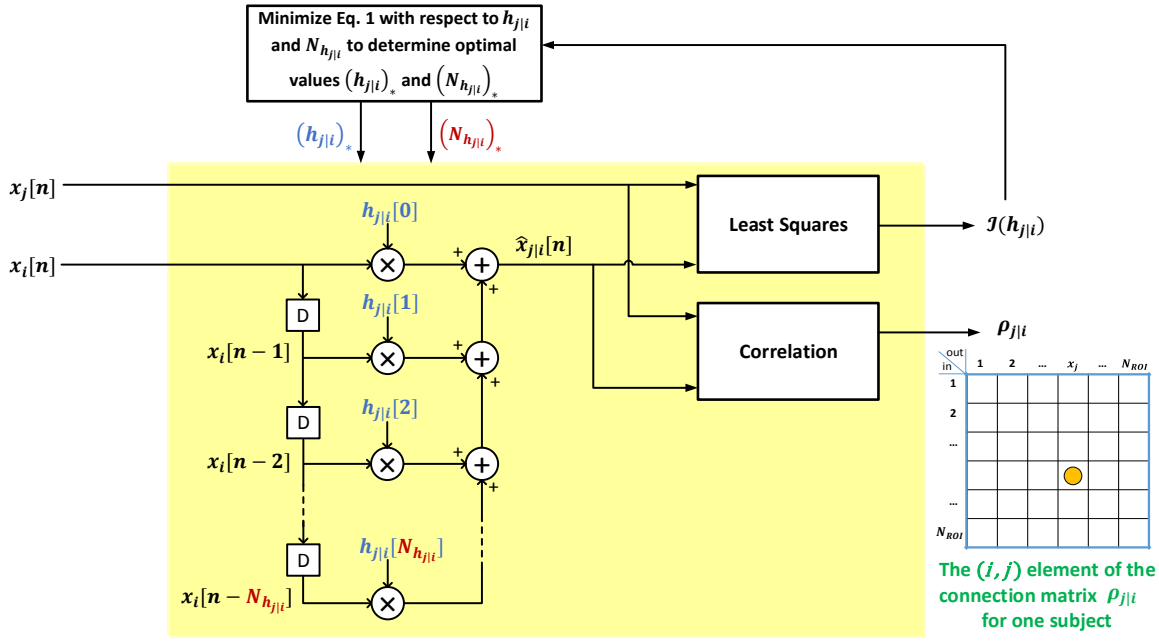

(a) Flow chart describing the computational method.

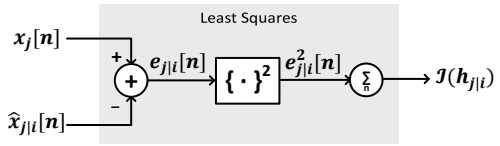

(b) "Least Squares" Sub-block.

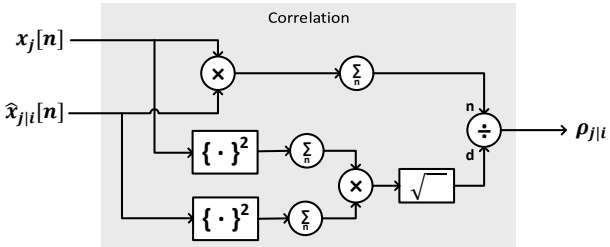

(c) "Correlation" Sub-block.

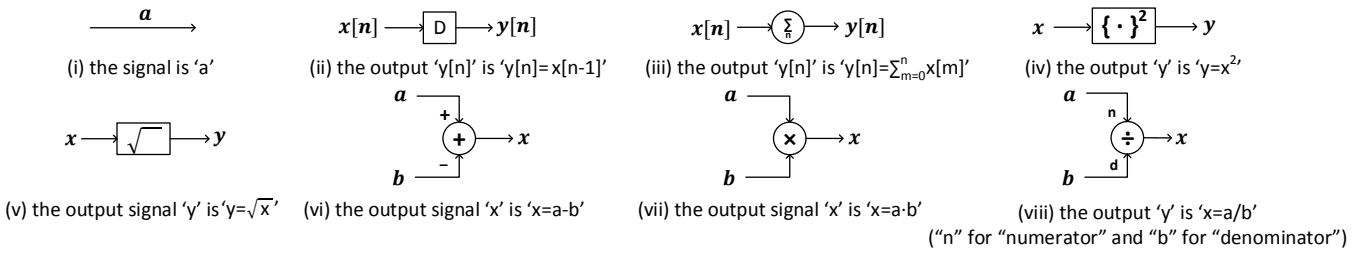

(d) Operators used in the block diagrams of Panels (a)-(c). Lines that intersect in the form ⊣⊢, do not connect at the intersection while other intersections imply connections.

Figure 2.1: Block diagrams describing the computation of p-correlation for one pair of ROIs.

2.2.2 Specializations of the fundamental method

Thus far, we have proposed a method to computing p-correlation, which constructs a full asymmetric matrix of correlation values for each subject. The proposed method also constructs a second full asymmetric matrix, which provides the temporal causal relation in the form of lagged impulse response between any pair of ROIs. This fundamental method can be specialized for particular applications, often based on user's interests and what the user knows about the details of the applications. Several such specializations are described in the following paragraphs.

Constraints on the least squares problems

If the user has information on the type of interactions that are present, then this information can be used as a constraint on the least square problem that determines the impulse response which is the basis of the prediction. For example, as in the simulated data of Smith et al. [117], the interactions are all positive. Constraining the impulse response values $\mathbf{h}_{j|i}[n]$ to be nonnegative has implications for the values of $\rho_{j|i}$. Let $R_{j|i}$ be the covariance of x_j and $\hat{x}_{j|i}$. $R_{j|i}$ is related to the covariance of $x_j[n]$ and $x_i[n-m]$ (i.e., the m-lagged covariance of the two signals, denoted by $R_{j,i}[m]$) by $R_{j|i} = \sum_{m=0}^{N_{h_{j|i}}-1} R_{j,i}[m]h_{j|i}[m]$. The covariance $R_{j|i}$ is the numerator of $\rho_{j|i}$. Therefore, if all the lagged covariances are positive and we require the estimated values of $h_{j|i}[m]$ to be positive then we are assured of getting a nonnegative value for $R_{j|i}$ and for the p-correlation $\rho_{j|i}$. In the traditional functional connectivity analysis, when global signal regression is applied to rs-fMRI timeseries data, the valid inference of negative correlations cannot be

made [91, 108], and only positive correlations are interpreted. In this situation, the nonnegative "constrained" estimation approach is appropriate.

Thresholding $\rho_{j|i}$

Three natural methods for thresholding $\rho_{j|i}$ are described in this section.

Even with $h_{j|i}[n] \geq 0$, it may be that p-correlation is not positive because one or more of the m-lagged covariance values are negative. Therefore, if nonnegativity is required, we replace all negative $\rho_{j|i}$ values by zeros. One reason for seeking to have $\rho_{j|i}$ non negative is mean signal regression in the preprocessing of the fMRI data which makes it difficult to interpret negative correlations. However, alternative preprocessing which omits mean signal regression [67] removes this requirement.

The previous paragraph concerned thresholding at value 0. Higher data-dependent minimum thresholds are often used for correlation and the same approach can be applied to p-correlaton. A standard approach [97] is to order the values of correlation and leave the top s percent of values unchanged and set the remaining values to zero. In other words, the threshold $\gamma(s)$ is set to be the 100-s percentile of all values in the p-correlation matrix.

In some problems the interactions are known to be unidirectional, e.g., in the simulated data of Smith [117]. In this situation, a third thresholding method, which makes p-correlation unidirectional, is natural. The threshold is to consider the two transpose related elements of the matrix and set the smaller to zero and leave the larger unchanged.

All of the thresholding methods are nonlinear operation applied to the ma-

trix of $\rho_{j|i}$ coefficients. Each can be applied to any matrix M to give an output matrix N, in particular, in the order of the previous three paragraphs,

$$N_{ij} = \begin{cases} M_{ij}, & \text{if } M_{ij} \geq 0 \\ 0, & \text{otherwise} \end{cases}, \tag{2.4a}$$

$$N_{ij} = \begin{cases} M_{ij}, & \text{if } M_{ij} \geq \gamma(s) \\ 0, & \text{otherwise} \end{cases}, \tag{2.4b}$$

where $\gamma(s)$ is the $100 - s$ percentile of all values in M, and

$$N_{ij} = \begin{cases} M_{ij}, & \text{if } M_{ij} \geq M_{ji} \\ 0, & \text{otherwise} \end{cases}. \tag{2.4c}$$

The thresholding approach forms a $N_{\text{ROI}} \times N_{\text{ROI}}$ matrix of thresholded connection weights, from which the network is computed.

Averaging over subjects

Some investigations, e.g., [117, 76], are interested in estimating individual-level nuances, but in many other investigations on functional networks of human brain using experimental data, e.g., [97, 98, 110, 53], there is averaging over subjects in order to improve the SNR. Just as the thresholding methods (Section 2.2.2), which are nonlinearities that can be applied to any matrix, the averaging we use can be applied to any family of matrices M_k ($k \in \{1, \ldots, K\}$, where K is the number of subjects) to give an output matrix N via $N = \frac{1}{K} \sum_{k=1}^{K} M_k$. The functional network estimated by the averaged p-correlation matrix can be further clustered into sub-networks through a graphic theoretic analysis.

2.2.3 Extension on multi-subject processing

There is a recent interest in estimating effective networks from multiple subjects while accommodating the heterogeneity of the group [116, 102, 47]. Specifically, the IMaGES algorithm [102] estimates one generalized network from a group by assuming all subjects are homogeneous, and the GIMME algorithm [47] can further refine the estimate for each individual subject from the general information estimated from the whole group. IMaGES and GIMME are based on existing single-subject methods, specifically GES for IMaGES and uSEM and euSEM for GIMME and, when applied to groups of appropriate size, both GIMME and IMaGES provide more accurate estimates of effective connectivity than the single subject methods on which they are based [101, 47].

Information concerning groups of subjects could also be used in p-correlation. One approach would be to replace the $\mathbf{h}_{j|i}$ in Eq. 2.1 by $\mathbf{h}^g_{j|i} + \mathbf{h}^l_{j|i}$, where $\mathbf{h}^g_{j|i}$ is the group component common to all subjects, and $\mathbf{h}^l_{j|i}$ is the component unique to the specific subject l. In this approach, Eq. 2.1 would be generalized to

$$\hat{x}^l_{j|i}[n] = \sum_{m=0}^{N_{\mathbf{h}^g_{j|i}}} \mathbf{h}^g_{j|i}[m] x^g_i[n-m] + \sum_{k=0}^{N_{\mathbf{h}^l_{j|i}}} \mathbf{h}^l_{j|i}[k] x^l_i[n-k]^l \tag{2.5}$$

where $N_{\mathbf{h}^g_{j|i}}$ and $N_{\mathbf{h}^l_{j|i}}$ are the probably different durations of the two components of the causal finite-duration impulse response. There are two issues when using Eq. 2.5. First the AIC analysis must be generalized in order to determine two impulse response durations where one is common to the entire group of subjects. Second, in order to require the least squares to use the group impulse response and not just set it to zero, a regularizer such as $\sum_{m=0}^{N_{\mathbf{h}^l_{j|i}}} (\mathbf{h}^l_{j|i}[m])^2$ must be added to the least squares cost. While both of these issues can be addressed, in the

current paper, we only focus on the individual analysis, which may be the only meaningful option under certain circumstances, i.e., a clinical environment.

2.3 Application on simulated Data

2.3.1 Data source: simulated BOLD timeseries

Simulated fMRI timeseries from the laboratory of S. M. Smith are documented [117] and available on-line (`http://www.fmrib.ox.ac.uk/analysis/netsim/`), which has been used as a benchmark simulated fMRI data for testing effective connectivity [117, 47, 101, 63]. The simulations are based on a variety of underlying networks of different complexity and can be described as having three levels. First there is a neural level which is a stochastic linear vector differential equation which produces a neural timeseries for each ROI. Second, for each ROI, there is a nonlinear balloon model driven by the corresponding neural timeseries which produces a vascular timeseries. Third, for each ROI, the fMRI timeseries is the vascular timeseries plus thermal noise. To simulate preprocessing of fMRI data, a highpass filtered at a cutoff frequency of 1/200s was applied to each simulation (lastly revised on Aug. 24, 2012 from the website `www.fmrib.ox.ac.uk/analysis/netsim`). The current paper considers the first four sets of simulations from [117], $Sim1 - Sim4$, which are the four most "typical" network scenarios provided in [117], and which are based on different underlying networks with sizes 5, 10, 15, and 50 ROIs, respectively.

These synthetic fMRI timeseries were sampled every 3s (TR= $3s$) and the total duration is N_x = 60 mins. All four simulations have 1% thermal noise and

the hemodynamic response function (HRF) used in the second step has standard deviation of 0.5 s. The simulation is repeated for each of 50 subjects.

2.3.2 Specialization on p-correlation for the processing of the simulated data

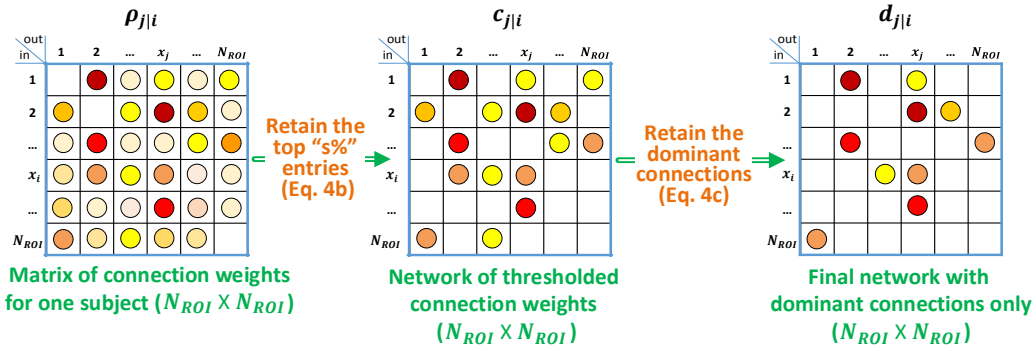

Figure 2.2: Block diagram describing the specialization of p-correlation for simulated data. Nonzero entries are filled by colored dots with higher values represented by "hotter" colors and lower values represented by "colder" colors, and zero entries are left as blank in the above matrices.

The algorithm is shown in Figure 2.2. Given that the interactions are all positive in the simulated data, it is natural to apply the nonnegative constraint on the least square problem so that no negative impulse responses are allowed. Through unconstrained p-correlation is also computed on the simulated data, looking forward to Section 2.3.5, the numerical results indicate that the constrained version is more appropriate.

As is described above, the integer minimization over the impulse function duration, $N_{h_{ji}}$, is computed by testing from 1 second up to D seconds. Assuming

that knowledge of the behavior of a ROI over the past 15 seconds is sufficient to describe its effect on a second ROI, we restricted the temporal window for directional influence between ROIs to no more than 15s, i.e. $D = 15s$.

Next, we consider the choice of threshold, s in Eq. 2.4b. We use this method in order to exploit all of the a priori knowledge about the simulated data. Since the underlying ground truth networks for the simulated fMRI timeseries, denoted by $a_{j|i}$, are given, the threshold value s is among our prior knowledge as is described below. We denote ROIs that are involved in the connections of the ground truth network as active ROIs. All connections involving the active ROIs are connections of interest (COIs), including connections that are actually absent such as the reverse connection in an unidirectional interaction. The value of s is then the ratio of the number of COIs and the number of all possible connections, which gives $s = 40,\ 22,\ 16$ and 4 percent for the four simulations, respectively. An example of computing s for a 5-node network is shown in Fig. 2.3.

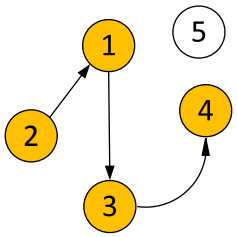

A 5-node ground truth network,
25 possible pairs of connections.
ROIs={1, 2, 3, 4, 5},
Activated ROIs={1, 2, 3, 4}.

(a) A 5-node ground truth network.

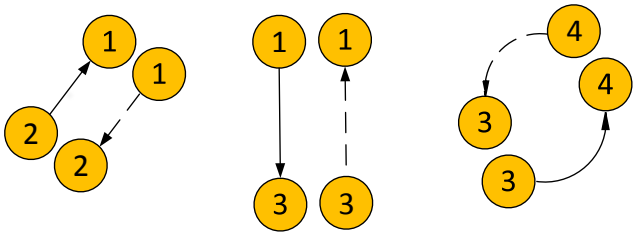

COIs={(1, 2), (2, 1), (1, 3),
(3, 1), (3, 4), (4, 3)}.

(b) 6 pairs COIs.

Figure 2.3: Example calculation of the threshold s for a 5-node network. (a) The network with activated ROIs shown in orange. The number of all possible connections is $5^2 = 25$. (b) The 6 COIs, where the dashed lines are connections that do not existed in the ground truth but still are considered interesting. Therefore, $s = 6/25$ for this network.

For the Smith simulated data, we have additional prior knowledge that the networks contain only unidirectional connections. Therefore, as is also done in [117], we compare our estimated network $d_{j|i}$, which includes the unidirectional condition, with the ground truth network $a_{j|i}$. The estimated network $d_{j|i}$ is the output of Eq. 2.4c where the input is the thresholded network $c_{j|i}$.

2.3.3 Performance Criteria

To compare the computed and ground truth networks, we define "accuracy", denoted by $\mathcal{A}$. In particular, $\mathcal{A}$ is defined to be the mean fractional rate of detecting the correct directionality of true connections. Specifically, it is defined to be

$$\mathcal{A} = \frac{\sum_{i=1}^{N_{\text{ROI}}} \sum_{j=1}^{N_{\text{ROI}}} 1\{a_{j|i} > 0\} 1\{d_{j|i} > 0\}}{\sum_{i=1}^{N_{\text{ROI}}} \sum_{j=1}^{N_{\text{ROI}}} 1\{a_{j|i} > 0\}}, \tag{2.6}$$

where $1\{L\}$ is 1 if L is true, and 0 otherwise. Like the computation of the "d-accuracy" introduced in [117], $\mathcal{A}$ evaluates the percentage of the correct directionality. The threshold operation introduced above (Section 2.3.2) differentiates the performance of directional analytical methods based on their sensitivity. The more sensitive the method is, the more true connections it can detect. Notice that application of the threshold s leads to $d_{j|i}$ values that are almost certainly far from zero or exactly zero. Computing the accuracy $\mathcal{A}$ after the threshold operation tells the directionality after knowing the presence of the connections, which enable us to evaluate the overall performance of sensitivity and directionality of a directional analytical method.

2.3.4 Alternative methods for effective networks estimation

P-correlation and four alternative methods from [117], specifically, "Granger B1", "Gen Synch S1", "LiNGAM" and "Patel's conditional dependence measure", were compared by the accuracy criteria ($\mathcal{A}$), since under both synthetic and experimental scenarios, these methods have been tested and have relatively good performances among all the others [117, 34]. The computation of

these methods were done by software provided by Prof. S.M. Smith. Granger B1, a pairwise Granger causality estimation method which provides the best performance among Granger causality approaches [117, 34], uses the Bayesian Information Criterion to estimate the lag up to 1 TR. Gen Synch S1 is a non-linear synchronization method with respect to the time lag 1 TR. It "evaluates synchrony by analyzing the interdependence between the signals in a state space reconstructed domain" [32, p. 671]. The LiNGAM (Linear, Non-Gaussian, Acyclic causal Models) algorithm is a global network model utilizing higher-order distributional statistics, via independent component analysis, to estimate the network connections. Patel's conditional dependence measure investigates the causality from the imbalance between two conditional probabilities, $P(x_j|x_i)$ and $P(x_i|x_j)$. P-correlation, Granger B1, Gen Synch S1 and LiNGAM all compute an asymmetric matrix filled with real-number connection weights, analogous to our $c_{j|i}$. In all cases, the unidirectional prior knowledge is applied analogous to our transformation from $c_{j|i}$ to $d_{j|i}$. For the Patel method implemented by [117], the thresholding operation was applied on "Patel's κ bin 0.75" matrix, while the directionality was determined by "Patel's τ bin 0.75" matrix.

In addition to the algorithms included in [117], IMaGES [102] and uSEM [70] which is the estimation method for resting-state fMRI employed by GIMME algorithm, have also been tested on the same set of simulated data [101, 47]. Results reported in [101, 47] show that their estimation based on the single subject is either similar to or less good than the best-performing method provided in [117].

Comparing p-correlation with alternative methods of estimating effective connectivity, p-correlation provides an full asymmetric matrix for each indepen-

dent individuals directly, in which each entry, like correlation, predict a connection strength between two ROIs. This full asymmetric matrix of p-correlations can be thresholded as desired and/or further processed as desired using another algorithm, i.e., a graph analytic algorithm, and is therefore potentially useful in a experimental/clinical environment. In addition, p-correlation can process networks with hundreds on ROIs while GIMME is limited to 3-25 ROIs (Page 3 of GIMME Manual (Version 12)). Furthermore, p-correlation estimates the temporal causal relation in the form of lagged impulse response in addition to the spatial causal relation between any pair of ROIs. In contrast, some alternatives algorithms (e.g. IMaGES) estimate a sparse graph of interactions, and thus solve a somewhat different problems than the p-correlation method. Other algorithms have been developed as post-processing algorithms, which cannot detect connections, but only estimate direction if connections are detected by other methods, e.g., correlation. Among them, pairwise LiNGAM [63] achieved success on Smith data. Several algorithms, such as Patel's τ, LiNGAM and pairwise LiNGAM, chose one of the two possible directions for each pair of ROIs. Such unidirectionality may be appropriate in some situations. Alternative algorithms, including p-correlation, provide strengths for both directions, where the two strengths may be quite different when one direction is dominant.

2.3.5 Results on simulated data

The methods described in this paper were implemented in Matlab software, which is available upon request, and were applied to four of Smith's fMRI simulations [117]. The four simulations are $Sim1 - Sim4$ which have a variable number of ROIs (5, 10, 15, 50) but no confounding variables.

The p-correlation method is based on estimation of a linear time-invariant causal dynamic model. The sample means of the duration of either constrained or unconstrained impulse responses are 3.34s, 3.58s, 3.64s and 3.76s for the 4 simulations, respectively. By limiting the impulse response duration to 1 TR, it was verified that p-correlation with constraint on Least Squares is equivalent to the standard correlation as is described in Section 2.1. After thresholding the p-correlations computed with the nonnegative constraint on the coefficients of the linear system, an asymmetric matrix of connection weights $c_{j|i}$ for each subject was obtained.

The same specifications for processing of the simulated data, in particular, the same choice of the s threshold (Eq. 2.4b) and the knowledge of unidirectionality (Eq. 2.4c), have also been applied to the results of four alternative methods introduced in Section 2.3.4. The performance of all five methods was evaluated by the accuracy criteria $\mathcal{A}$ (Eq. 2.6) for each subject. Fig. 2.4 shows the input to the accuracy criteria $\mathcal{A}$, i.e., $a_{j|i}$ and $d_{j|i}$, for Subject 14 of $Sim2$.

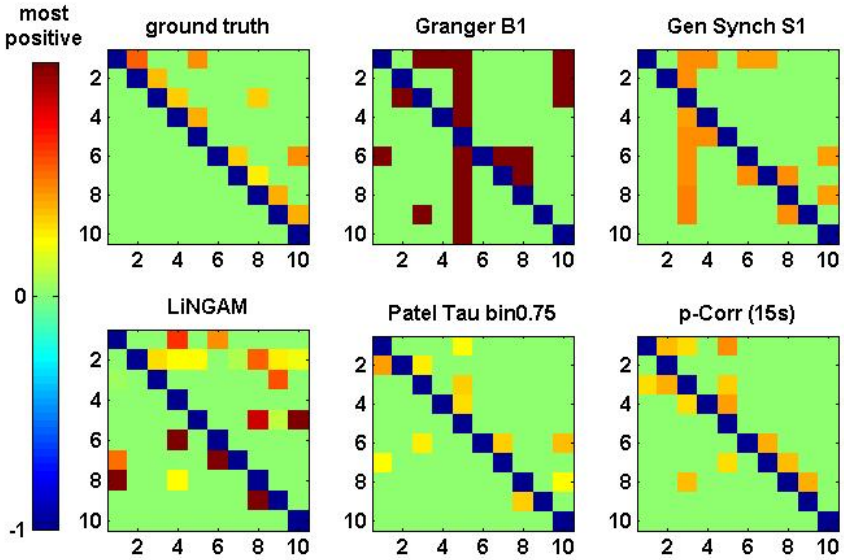

Figure 2.4: Images of $a_{j|i}$ (for ground truth) and $d_{j|i}$ (for constrained p-correlation), and quantities analogous to $d_{j|i}$ (for Granger B1, Gen Synch S1, LiNGAM, and Patel) for Subject 14 of $Sim2$. Each image uses the same ordering of colors, but has different range of numerical values.

Simulation	1	2	3	4
# of ROIs	5	10	15	50
# of COI pairs	10	22	36	122
Granger B1	.440±.206	.295±.127	.262±.088	.130±.044
Gen Synch S1	.472±.201	.405±.139	.379±.079	.285±.056
LiNGAM	.372±.229	.435±.177	.301±.106	.119±.037
Patel	.528±.193	.491±.101	.446±.099	.366±.048
p-Corr (constrained)	.532±.192	.502±.114	.457±.126	.405±.065
p-Corr (unconstrained)	.520±.218	.467±.123	.439±.109	.371±.058

Table 2.1: Comparison of the mean and standard deviation of accuracy over 50 subjects among different methods. The standard deviation tend to be larger on the smaller netowrks ($Sim1$-$Sim4$ have 5, 10, 15, 50 ROIs, respectively) because one error is proportionally of larger impact in a smaller network.

The mean and standard deviation of accuracy for each simulation, i.e., the

average and square root of the sample variance of $\mathcal{A}$ (Eq. 2.6) over all 50 subjects, were computed and the results are tabulated in Table 2.1. For all four simulations, constrained p-correlation achieved the highest accuracy compared to the others. The unconstrained p-correlation is less appropriate when applied to a network with all positive connection weights. We also computed the mean and standard deviation of $\mathcal{A}$ for pairwise LiNGAM, which gives .566±.138, .656±.206, .510±.119 and .506±.056 for four simulations, respectively. The result shows the highly accurate directionality that pairwise LiNGAM can achieve in this particular unidirectional network setting. Histograms displaying the distribution of accuracy for the five methods for each simulation are shown in Fig. 2.5. The superior performance of p-correlation is demonstrated by the fact that the bulk of the histogram is further to the right, and the left tail is less massive.

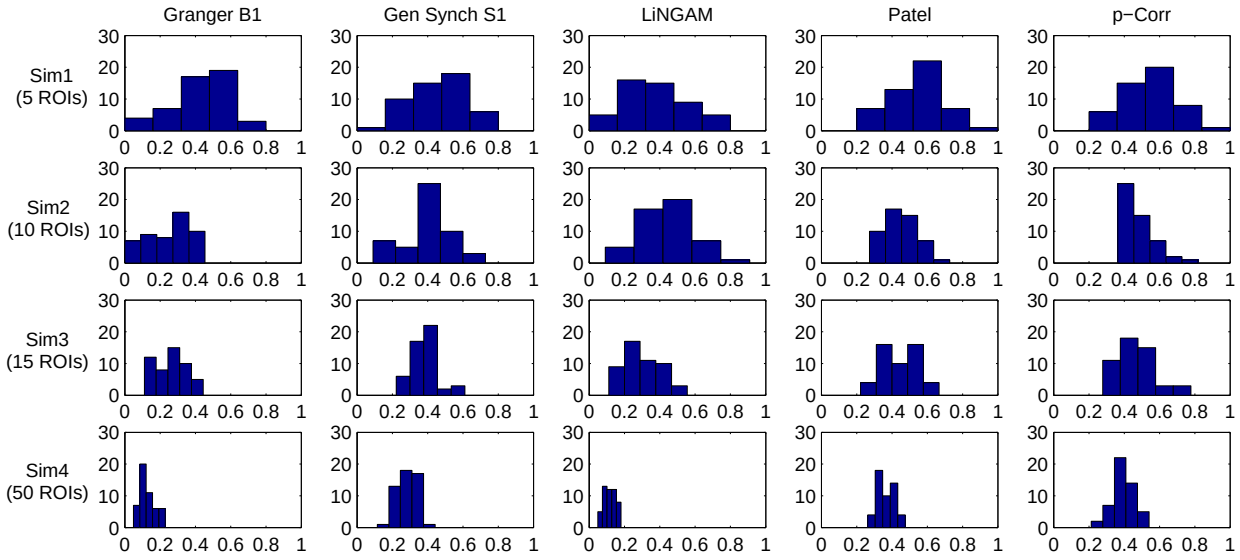

Figure 2.5: Accuracy histogram for Granger B1, Gen Synch S1, LiNGAM, Patel and constrained p-correlation.

2.4 The performance of correlation and p-correlation on common drivers

A "common driver" situation is the case where ROI 1 drives ROIs 2 and 3 but ROIs 2 and 3 do not directly interact. The challenge is to correctly detect the 1→2 and 1→3 connections without detecting 2→3 or 3→2 false connections. In order to focus exclusively on this situation, we have computed synthetic data from the three-ROI network shown in Fig. 2.6 and defined by

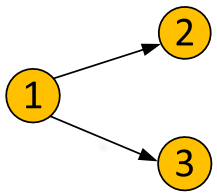

Figure 2.6: The common driver problem.

$$x_1[n+1] = a_1 x_1[n] + b_1 w_1[n] \tag{2.7}$$

$$x_2[n+1] = a_2 x_2[n] + a_{21} x_1[n] + b_2 w_2[n] \tag{2.8}$$

$$x_3[n+1] = a_3 x_3[n] + a_{31} x_1[n] + b_3 w_3[n] \tag{2.9}$$

where $w[n] = [w_1[n], w_2[n], w_3[n]]^T$ is an independent and identically distributed Gaussian stochastic process with mean 0 and variance I_3 (the 3×3 identity matrix). [143] consider mathematical models of this type and give theoretical results for correlations. The system is initialized in the steady state and simulated for 1000 steps, $N_x = 1000$. We consider only $a_1 = a_2 = a_3 = .8$ (so that all ROIs

have the same intrinsic memory duration) and $b_1 = b_2 = b_3 = .2$ (so that all ROIs have the same intrinsic noise power, and the intrinsic noises are all independent). We consider the following cases: (1) no driving: $a_{21} = a_{31} = 0$, (2) weak driving: $a_{21} = a_{31} = .1$, (3) strong driving: $a_{21} = a_{31} = .4$, and (4) asymmetrical strong driving: $a_{21} = .4$, and $a_{31} = .1$.

Each simulation was repeated for 50 subjects. Let the maximum allowable duration of the impulse response be 3 samples. By using the specialization of p-correlation for Smith simulated data, as is described in Section 2.3.2, a directed graph $d_{j|i}$ is estimated by p-correlation (Fig. 2.2) and the correlation matrix is computed for each subject. The steady state covariance of Eqs. 2.7-2.9 is the correlation matrix. In Case (1), the mean and standard deviation of nonzero entries of $\rho_{j|i}$ with constrained least squares (Section 2.2.2) are 5.384e-04±0.072. This number becomes 0.058±0.043 when unconstrained least squares is applied. The smaller magnitude of the results using constrained least squares indicates that taking advantage of the prior knowledge that the weights are positive (i.e., $a_1 = a_2 = a_3 = .8$) provides improved performance in this case. In Cases (2) and (3), both the constrained and the unconstrained least squares achieve a 100% accuracy (Eq. 2.6) for each subject. In the fourth case, the constrained or the unconstrained least squares gives an average of .800±.247 accuracy over all 50 subjects. We also tested N_x =200, 500, 5000 for all four cases. Notice that as N_x goes large, correlations become closer to the steady state and the accuracy computed by the p-correlation method increases as well.

In addition, p-correlation estimated the correct hierarchy on the three pairs of connection weights, which are consistent with "strong", "weak" and "non-" connections in the ground truth network. It also shows the correct direction of

connections in a pair by a stronger weight. The constrained least squares (Section 2.2.2) provides a slightly superior result than the unconstrained approach. Specifically, larger numerical differences between the zero and nonzero entries, as well as between the asymmetric strong weights, were shown. On average across all 50 subjects, p-correlation used an impulse response duration of 1.007 samples for all four cases for both constrained and unconstrained approaches. In addition, in Case (3) (asymmetric strong weights), correlation mis-detected the connection between node 2 and 3, specifically the 2-3 correlation was the highest correlation value among the three pairs, whereas p-correlation, for both the constrained and unconstrained approaches, estimated this value as the lowest of the three pairs thereby avoiding the error in the correlation results.

2.5 Performance on experimental fMRI data

While the tools described in this paper can be assembled into many algorithms, we use only one algorithm, which is shown in Figure 2.7, to further characterize [139], a cohort of 132 subjects from the 1000 Functional Connectomes Project (`http://www.nitrc.org/projects/fcon_1000/`) [16]. We combine our p-correlation ideas with the widely-used [97, 96, 73, 53] Infomap graph analytical algorithm [74] to determine networks within the set of 264 ROIs.

As a function of the value of the threshold s, Infomap creates a variable number of networks. Following [97, Fig. 1], the network stability over a range of threshold $s \in \{2, \ldots, 10\}$ using correlations and p-correlations are shown in Fig. 2.8, in which different networks are represented by different colors. Similar to [97] (the first figure in Fig 2.8), we note that the assignment of ROIs to networks remains relatively constant over all values of the threshold s, illustrated

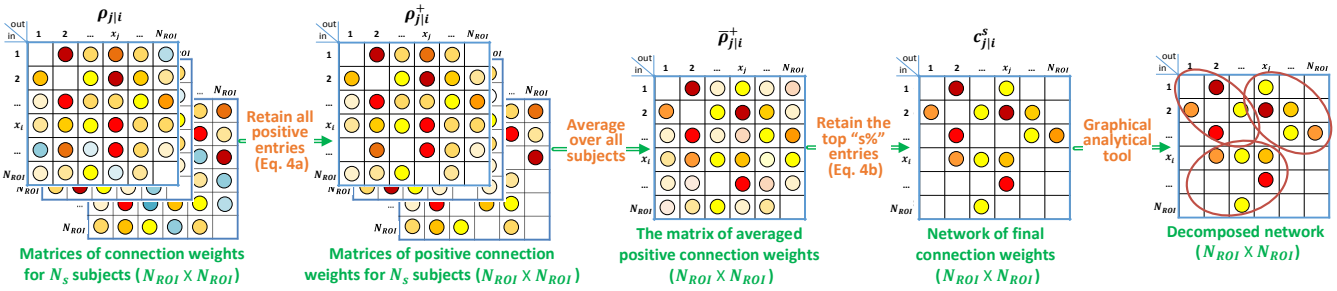

Figure 2.7: Block diagram describing the specialization of p-correlation for the experimental data. Nonzero entries are filled by colored dots with higher values represented by "hotter" colors and lower values represented by "colder" colors, and zero entries are left as blank in the above matrices.

by the constant horizontal bands in different colors. Also, networks are hierarchically refined as s rises. In summary, the number of networks increases as the value of s decreases, and p-correlation replicated the brain network organizations that were detected by correlation. The network results are consistent with the network organizations detected in [97].

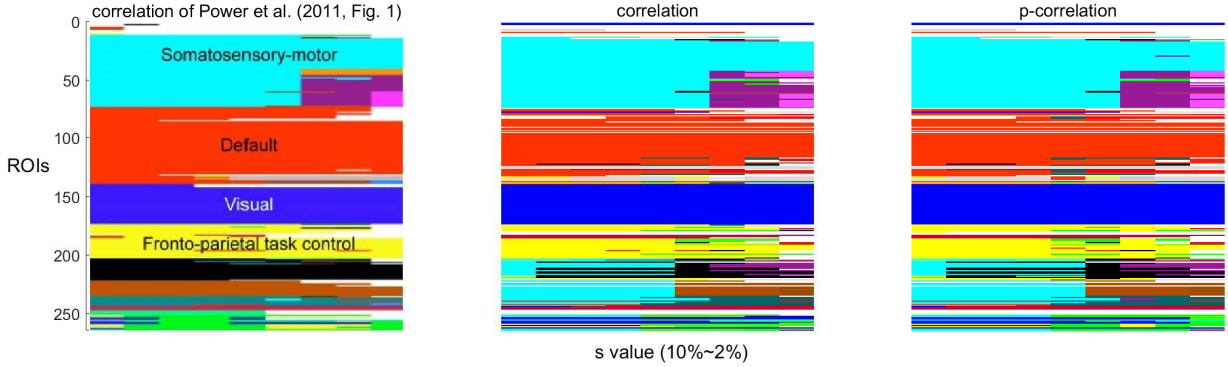

Figure 2.8: The stability of networks across various thresholding criteria (s). The white regions indicate ROIs that belong to networks with less than four ROIs.

1085

In order to test the robustness of the p-correlation calculation, all 132 subjects were randomly divided into two equal cohorts, and each cohort was separately processed. The average of p-correlation connection strength $\rho^+_{j|i}$ across all sub-

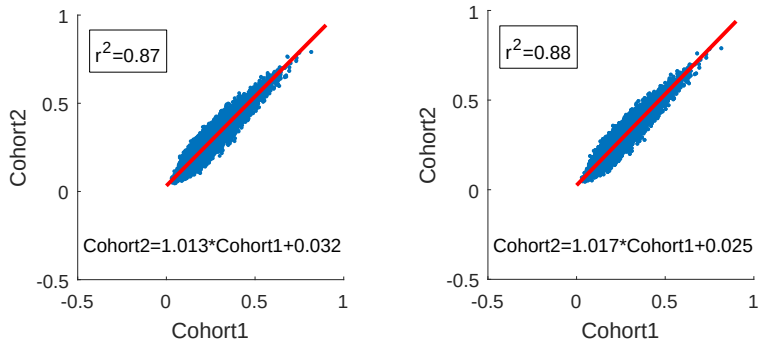

(a) p-correlation (b) correlation

Figure 2.9: Scatter plot of p-correlation and correlation for the two cohorts. The red line is the Least Squares fit for predicting Cohort 2 from Cohort 1. Only positive values are used in the Least Squares calculation and shown in the plot.

jects in the cohort, which is denoted by $\bar{\rho}^{+}_{j|i}$, is shown as a scatter plot in Fig. 2.9 (a) (in Fig. 2.9, all (0,0) points are removed). The linear least squares prediction of Cohort 2 from Cohort 1 is a close fit to the data (r^2 = .87) and is nearly a 45° diagonal line ($\bar{\rho}^{\text{Cohort 2}}_{j|i}$=1.013$\bar{\rho}^{\text{Cohort 1}}_{j|i}$+.032), thereby indicating the robust nature of p-correlation. Following the same procedure, the average of correlation connection strength $\rho^{+}_{i,j}$ across all subjects in the cohort, which is denoted by $\bar{\rho}^{+}_{i,j}$, is shown in Fig. 2.9 (b). Comparing Fig.2.9 (a) and (b) indicates that the p-correlation achieves the same robustness as correlation. Additional plots in which no points are removed are included in the supplemental material Fig. 2.

2.6 Discussion

Standard correlation has been widely used to analyze functional connectivity from rs-fMRI timeseries between prespecified ROIs. Prior work has shown its high sensitivity for detecting the existence of network architectures under both

simulated and experimental scenarios [117, 34]. This paper describes methodology for analyzing rs-fMRI data using a generalization of well-established correlation ideas. The generalization, denoted by "p-correlation" ("p" for "prediction"), is to compute the correlation between the j^{th} signal and an optimal linear time-invariant causal estimate of the j^{th} signal based on the i^{th} signal. In this way, it captures additional features concerning the interaction between two ROIs, specifically, the causality and directionality of the information flow on which the interaction depends. Based on the finite-memory linear time-invariant causal model, p-correlation allows the memory duration to be different in the two directions for one pair of ROIs and also to be different for different pairs of ROIs. In contrast, structural vector autoregressive models [70, 22] are assumed to have the same memory duration across all ROIs. P-correlation is a generalization of standard correlation ideas because, if the estimate of the j^{th} signal based on the i^{th} signal is restricted to use only the current value of the i^{th} signal, then p-correlation and standard correlation have the same magnitude.

Testing p-correlation on simulated fMRI data provided in [117], the greater performance accuracy of p-correlation, which uses lagged information from the BOLD timeseries, demonstrates the importance of causal information which is missing in standard correlation. In our results, the mean duration of the impulse response estimated by AIC using a search limited to a maximum duration of 15s was roughly 4s. In these data, a search extending to 15s is not a restriction on the maximum duration. As is described in Table 1, the accuracy of p-correlation on the simulated data of Smith is about 0.5 (0.405 to 0.532). While higher levels are desirable, this performance exceeds the performance of many alternative algorithms on all four sets of simulations.

Many approaches have been introduced to assess functional or effective connectivity of rs-fMRI data. [117] evaluated the validity of 38 approaches [117, Fig. 4] using simulated BOLD signals and a variety of performance measures. The methods tend to have different levels of performance for different measures, e.g., detection of a connection versus determination of the direction of a connection. The p-correlation approach introduced in this paper depends on causal dynamical models and so we focus on this particular aspect of previous work. Dynamic Causal Modeling (DCM) has been used with some success to assess causal dynamics in fMRI data by relying on sophisticated models of neural dynamics. As discussed in [117, p. 878], most existing DCM algorithms require knowledge of external inputs (which are not known for rs-fMRI) although some variations may not [31]; all versions tend to be mathematically poorly conditioned; and all versions fail to scale to networks with large numbers of ROIs which are necessary for experimental studies. In contrast, the p-correlation approach described in this paper scales similarly to a correlation approach for which hundreds of ROIs are not a challenge [139].

Several versions of Granger causality analysis, based on multivariate vector autoregressive modeling, have been tested and performed poorly [117]. Granger causality relies on regression and comparison of two predictions. The first prediction is based purely on an autoregressive model of the signal at the ith ROI based on the past of the same signal. The second prediction is based on regression of the signal at the ith ROI based on the past of the signal at the jth ROI and, possibly, an autoregression as in the first case. The sample covariances of the prediction errors are then combined, essentially by taking the ratio of the sample covariances scaled by integers describing the amounts of data, to yield a statistic that is distributed according to the Fisher-Snedecor F distribution. This

statistic, indexed by i and j, is used to fill an asymmetric matrix. Although both are based upon lagged information there are important differences between p-correlation and Granger causality. P-correlation is not a statistic comparing two possible dependencies but rather is a statistic measuring the accuracy of prediction using a particular dependency. The motivation for the Granger causality statistic is dependent on the original Gaussian assumptions on the errors when linear regression is used to describe the ROI time series. P-correlation is based on just the sample variance of the prediction error and does not have a Gaussian motivation which is advantageous if the BOLD signals lack Gaussian structure. Multivariate autoregressive processes have been used as the basis for generative models for complete sets of ROIs. Such models, which focus on the effect of the past on the present, can be combined with structural equation modeling (SEM) models, which focus on contemporaneous effects [22].

Multivariate autoregressive processes (MVAR) have been successfully used in neuroscience outside of fMRI, e.g., in order to describe signals from EEG experiments [72, 17, 35, 10, 78, 71, 136]. Both MVAR, e.g., Eq. 1 in [72], and the linear regression model used in this paper (Eq. 2.1) are regression models which predict one timeseries from either all timeseries which include oneself (MVAR) or from the past of another timeseries (Eq. 2.1). Both predictions are characterized by impulse responses. The method introduced in [72] determines the connection strength based on the impulse response, whereas p-correlation determines the functional connectivity based on both the impulse response and the original timeseries. Existing literature, e.g., [126] and [33], has shown the robust estimation of the MVAR model by introducing sparse regression techniques, and the success of estimating functional connectivity through the sparse MVAR models. In addition, a conditional MVAR model, e.g., Ch 17.3 in [111], may also

be used to address the common driver problem. Other approaches to examining BOLD signal propagation using lags, as is done in p-correlation, have been highly reproducible [86]. In this paper, a linear regression model (Eq. 2.1) is used as the predictor in p-correlation to estimate the causal relation between a pair of BOLD signals. Other lag-based predictors, e.g., MVAR based models, can also be adapted into the p-correlation concept, however, they would not have the result that duration of 1 sample (e.g., no lags) gives standard correlation.

In addition to the algorithms used in [117], which estimate the directional connectivity for single subject data sets, the IMaGES [102, 101] and GIMME [47] algorithms use a group of subjects. While these algorithms provide better performance in situations where groups of subjects can be analyzed collectively, both algorithms have challenges. The sparse graph estimated by IMaGES for a group of subjects does not tell the strengths of the connectivity and "will not reflect the variation of a group" [90, p.571]. Similar to DCM's limitation on scalability, small networks with less than 25 ROIs are well analyzed by the GIMME algorithm. However, its performance on large-scale functional networks is not known. As p-correlation can work with hundreds of ROIs, it can be used in evaluating large-scale brain networks. Furthermore, p-correlation can work on individual subjects so it potentially could be applied to patient clinical data. Other algorithms that estimate direction after a connection is already detected also exist (Section 2.3.4). While such algorithms may be useful in some circumstances, they do not allow for situations where both directions are present but of different strengths.

The [117] simulated data has lower dimensionality than experimental brain data. For instance, in the simulation, connections are all unidirectional while

most neural connections are bidirectional. Additionally, in the simulations, most connections had a value of exactly zero. Furthermore, it introduces unrealistic noise and it has a large number of parameters that must be set and which influence the resulting simulation [132]. While the [117] simulated data is not completely realistic and it is not a perfect test of p-correlation, this data continues to be used [117, 47, 101, 63, 107], and the results continue to be discussed [48]. In this paper, we leveraged the same data used in [117] for comparison with other published metrics, providing a broader context for these findings. We hope to use a broader range of simulated data to further validate p-correlation in our future work.

In order to focus on the challenges of a "common driver", we have produced additional synthetic data for the three ROI network of Fig. 2.6 in which one ROI drives two other ROIs but the two other ROIs do not directly interact. Using p-correlation in this network we found that p-correlation can identify the existence and direction of the interactions between the driving ROI and the other two ROIs (even when the two interactions are of different strengths). Furthermore, p-correlation did not introduce false interactions between the two driven ROIs.

We have applied p-correlation to experimental data from the 1000 Functional Connectome Project [16]. The p-correlation approach successfully replicated the modular architecture of the local and distributed networks previously reported using standard correlation [139] (see Section 2.5 Fig. 2.8). Highly correlated p-correlation values on the two different cohorts also demonstrated that the p-correlation is highly reproducible and thus robust on experimental data. A current limitation of the p-correlation approach is that missing nodes cannot be accommodated, thereby limiting an extension of this approach to lesioned

populations.

Here we introduce a novel concept, the p-correlation, to estimate brain connectivity within well-characterized large-scale functional networks. The replication of previously observed network architectures in experimental data and the performance against the ground truth in simulated data, both suggest that the p-correlation approach may hold promise for future investigations of the brain's dynamic functional architecture.

2.7 Supplemental

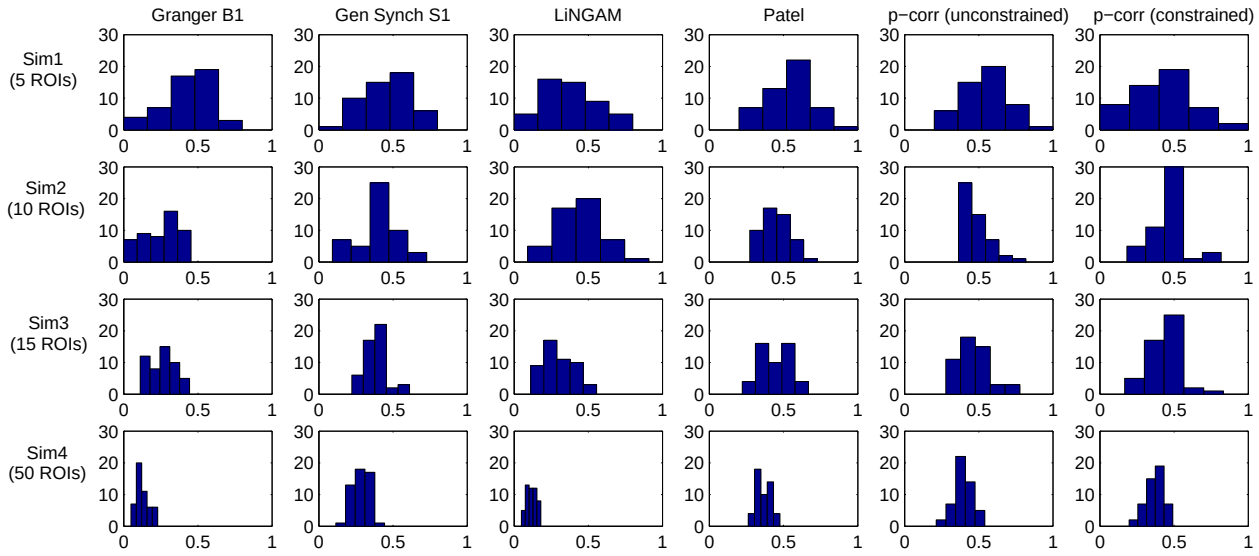

Figure 2.10: Accuracy histogram for Granger B1, Gen Synch S1, LiNGAM, Patel and p-correlation with unconstrained and constrained Least Squares.

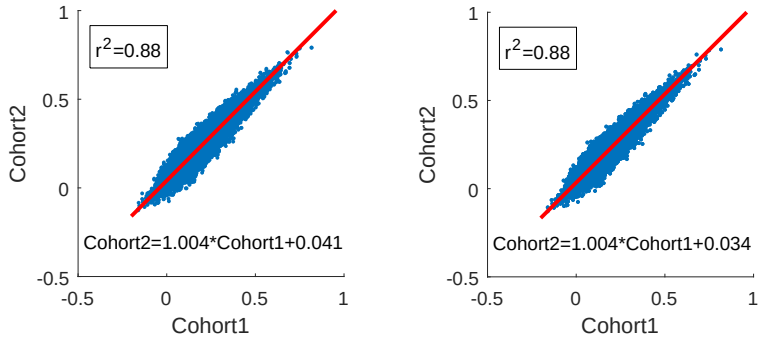

(a) p-correlation (b) correlation

Figure 2.11: Scatter plot of p-correlation and correlation for the two cohorts. The red line is the Least Squares fit for predicting Cohort 2 from Cohort 1.

CHAPTER 3

THE SPATIAL AND TEMPORAL INTERACTIONS IN RESTING STATE BRAIN NETWORKS

3.1 Introduction

Resting-state functional magnetic resonance imaging (fMRI), which examines the low frequency spontaneous fluctuations in blood oxygen level dependent (BOLD) signals [15], is widely used to investigate the brain activity at resting state. Resting-state brain activity persistently supports the neuronal signaling at the resting state, and consumes the majority brain energy metabolism in contrast to task-related brain activities [26]. The human brain is a complex network comprising parallel, interacting systems of anatomically connected areas. Substantial progress has been made in delineating large-scale functional brain networks using resting-state functional connectivity MRI (RSFC) (e.g. [15, 141, 97]), a technique which investigates brain networks that exhibit correlated fluctuations and provide indirect information about structural connectivity patterns that define brain systems. One fruitful approach has been to examine the pairwise RSFC correlations among a priori determined regions of interest (ROI). These correlation matrices may then be used to model the spatial topology of functional networks and sub-networks [135, 118].

With the use of RSFC, there has been a rich literature (e.g., [54, 41, 109, 26]) in understanding the functional activity of a brain region at the resting-state versus at a state in response to cognitive demanding tasks. Regions within anatomically connected brain systems, such as the motor, and visual systems, are strongly and selectively correlated, suggesting the potential to use such cor-

relations to infer the anatomic connectivity of brain systems. Results further show that at the resting state, functional activities in certain brain regions, commonly referred as the default network, increased which suppressed the activities in the motor and visual systems [54, 41]. It is clear that the intrinsic dynamic interplay between and within these large, spatially distributed brain systems is indisputable. Therefore, assessing the intrinsic dynamic causal interactions among ROIs, or "effective" connectivity, particularly in the context of large-scale brain networks becomes a substantial interest in recent years.

The most commonly used method of assessing RSFC is to compute the correlation coefficient between low frequency BOLD signal fluctuations of two regions. Standard correlation coefficient has been demonstrated to have high sensitivity for detecting functionally connected brain regions [117]. However, it is also noticed by the researchers that this method is not sufficient to detect the directional influence of the connection. To overcome this limitation, a novel concept, the so-called prediction correlation (p-correlation) which is a generalized notion of correlation, has recently been developed to estimate resting-state effective connectivity (RSEC) (Chapter 2). The advantages of the p-correlation approach, which is introduced in Chapter 2, includes that (1) it is a generalization of correlation and is able to replicate previously characterized large-scale network organization of the human brain, and (2) it determines reliable patterns of directed network interactivity, and (3) it estimates the duration of directed interactions in brain networks.

In this Chapter, p-correlation was tested on the high resolution fMRI data to investigate both the spatial and the temporal casual interactions in large-scaled brain systems. The brain wide variability in the duration of causal influence

enables to explore the slow (long duration) and the rapid (short duration) information flow in human brain. Our results agree with the previous discovery of the strong interactions between the visual and motor systems and deepen the understanding of these interactions from the temporal scale. In particular, information flow from the ROIs in the somotormotor system to the ones in the visual systems is slow. The most rapid information propagations are dominated by the information flow from ROIs of visual, motor and attention systems to the ROIs of the limbic system (in the medial temporal lobe). This observation validates the traditional hypothesis on the resting brain activity, which is relating to memory strengthening process, known as "consolidation" [85, 120, 52, 119, 122]. Furthermore, we determined a ranking of duration of the information flow from the seven well-known functional networks [141] to all other ROIs, which suggests that the frontal parietal, the limbic, and the default networks propagate the information faster than other networks in resting brain. These findings numerically validate the current understanding of brain functions at resting-state, and provide novel insights in brain functions from a different dimension (e.g., the temporal scale).

3.2 Temporal and spatial interactions in functional human brain netwroks

3.2.1 prediction correlation method

In this section, we review prediction correlation, denoted by "p-correlation", introduced in Chapter 2. P-correlation computes the correlation between the

BOLD signal at one ROI and a prediction of this signal based on the BOLD signals at the other ROI. As an effective connectivity analytical method, p-correlation provides reliable estimates of direction of the connectivity between ROIs. In addition, it is able to estimate the duration of a directed connectivity between pairs of ROIs. Furthermore, p-correlation is a generalization of correlation method, which is able to recover the previously detected modular organizations in resting brain [97].

The mechanism of p-correlation is described in the remainder of this section. Let x_i and x_j be the BOLD signals of N_x samples which come from the ith ROI and the jth ROI, respectively. P-correlation of the ordered pair (x_i, x_j), denoted by $p-corr(x_i, x_j)$ involves two-step computations: the first is to compute a prediction of the BOLD signal x_j from the signal x_i, which is denoted by $x_{j|i}$; the second is to compute the correlation between the predicted signal $x_{j|i}$ and the original BOLD signal x_j. In other words,

$$p-corr(x_i,\ x_j) = correlation(x_{j|i},\ x_j). \tag{3.1}$$

The prediction $x_{j|i}$ in the first step is the output of a linear time-invariant causal dynamic model with x_i as the input. This linear time-invariant causal dynamic model can be described by a finite length impulse response, denoted by $h_{j|i}$, which is a vector of $N_{j|i}$ samples and has the first potentially non-zero term occurred at time of 0s. In particular,

$$x_{j|i}[n] = \sum_{m=0}^{N_{j|i}-1} h_{j|i}[m]x_i[n-m]. \tag{3.2}$$

The positively constrained vector coefficients and the length $N_{j|i}$ are jointly optimized by Least squares and the Information Criterion, respectively. Assume that the temporal directional influence between ROIs is no more than Ds. Then,

the optimal solution for $N_{j|i}$ is selected between $\{0,\ldots,\frac{D}{TR}\}$ samples, where TR is the sampling rate.

3.2.2 Model of temporal and spatial interactions in functional networks

Unlike the standard correlation, p-correlation is asymmetrical between the two signals x_i and x_j. In particular, $p-corr(x_i,x_j) \neq p-corr(x_j,x_i)$ and $N_{j|i} \neq N_{i|j}$ in general, and thus p-correlation is able to model the spatial and temporal causal influence between ROIs. The "conversation" from the ROI i to the ROI j can be characterized by p-correlations. In particular, this directed connectivity has a strength of $p-corr(x_i,x_j)$, and a duration of $TR*N_{j|i}$ seconds. The asymmetry between $p-corr(x_i,x_j)$ and $p-corr(x_j,x_i)$ leads to a directed graph between two brain regions in the spatial scale. In addition, the separate estimations for $N_{i|j}$ and $N_{j|i}$ characterize the interactions in a temporal scale.

The duration of information flow from one region to the other is the entire time length of sending and receiving the information. A shorter duration allows a more rapid information propagation. In contrast, a longer duration gives a less rapid information flow from one region to the other. We are interested in the most rapid information propagations in resting human brain which is characterized by short durations, e.g., the smallest value of $N_{j|i}$.

3.3 Performance on experimental data

3.3.1 Participants and data preprocessing

A cohort of 200 subjects was randomly selected from the 900 subjects Human Connectome (`http://www.humanconnectome.org/documentation/S900/`). The small sampling rate, i.e., $TR = 0.78s$, allows for a meaningful estimation for the duration of connectivity. For each subject. the total scan duration has 200 samples, i.e., $N_x = 200$. The whole brain data was preprocessed [128, 83]. The preprocessed rs-fMRI BOLD signals were extracted from 333 ROIs ($N_{ROI} = 333$) which were centered in 333 disjoint brain parcels provided in [53].

3.3.2 Results

For each subject, two asymmetric matrices were generated from computing the p-correlations. One is a matrix of p-correlation values that characterizes connection strengths. The second matrix includes the durations determined by the Akaike Criterion. The functional connectivity map (Fig. 3.1 (left)) is determined by computing the average of the connection strength matrix across all 200 subjects. Similarly, the duration map (Fig. 3.1 (right)) is determined by computing the average of the duration matrix across all subjects.

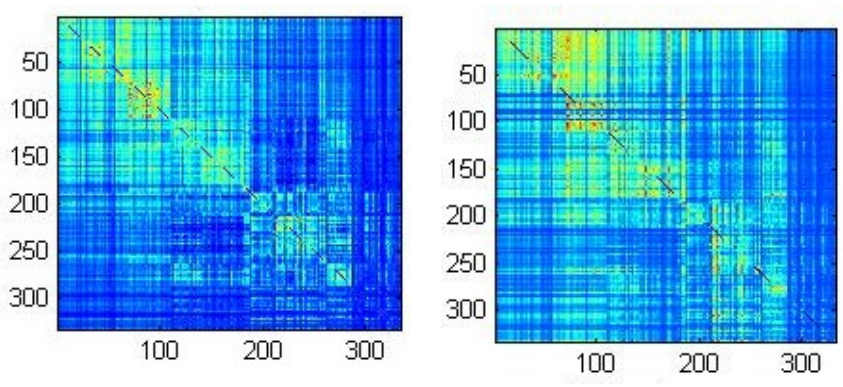

Figure 3.1: The functional connectivity map (left) and the duration map (right) determined by p-correlations. In the matrices, ROIs along the rows propagate information to the ROIs along the columns.

A graphic theoretic tool was utilized to determine the functional networks. Specifically, 333 ROIs were clustered into disjoint groups through the Informap software. Seven functional networks were identified through tuning the informap results based on the parcel community provided in [53] and to the 7 functional networks provided in [141]. Fig. 3.2 (a) shows the functional connectivity map masked by 7 sub matrices, which corresponds to the seven functional brain systems, organized along the diagonal. The seven functional brain systems are somatormotor (SM), visual, dorsal attention (dorsal), ventral attention (ventral), default, frontal parietal (FP) and limbic systems. Strong functional connectivities are interactions within the disjoint functional networks as shown in Fig. 3.2 (b). Suggested by the high values in Fig. 3.2 (c) and (d), the slowest (least rapid) information propagations are dominated by connectivities within the SM, visual and ventral systems as well as the information flow from the SM to the visual system. This result agrees with the previous results provided in [54, 41], suggesting that functional activities in the motor and visual systems are suppressed in the resting brain.

Fig. 3.2 (f) shows network connections which have the most rapid information propagations in resting brain. These connections are visualized on the cerebral cortex in Fig. 3.3. As shown, the most rapid information propagations are flowing into the limbic system. This is biologically reasonable as resting state activity supports the memory consolidation [85, 120, 52, 119, 122], in which the medial temporal lobe gathers information from the cortex [100, p. 313].

For each of the 333 ROIs, the duration of information flow from this ROI to all other ROIs are summed up. Specifically, the row's summation was computed for the duration map. This summation is then averaged over ROIs in the same functional network, which results in 7 averaged summations corresponding to the 7 resting-state functional networks as shown in Fig. 3.2 (e) and displayed on the cerebral cortex in Fig. 3.4. In such way, we determine a ranking of duration of the information flow from the seven well-known functional networks [141] to all other ROIs. The result suggests that the frontal parietal, the limbic, and the default networks propagate the information more rapid than other networks in resting brain. The ranking is tabulated in Table 3.1.

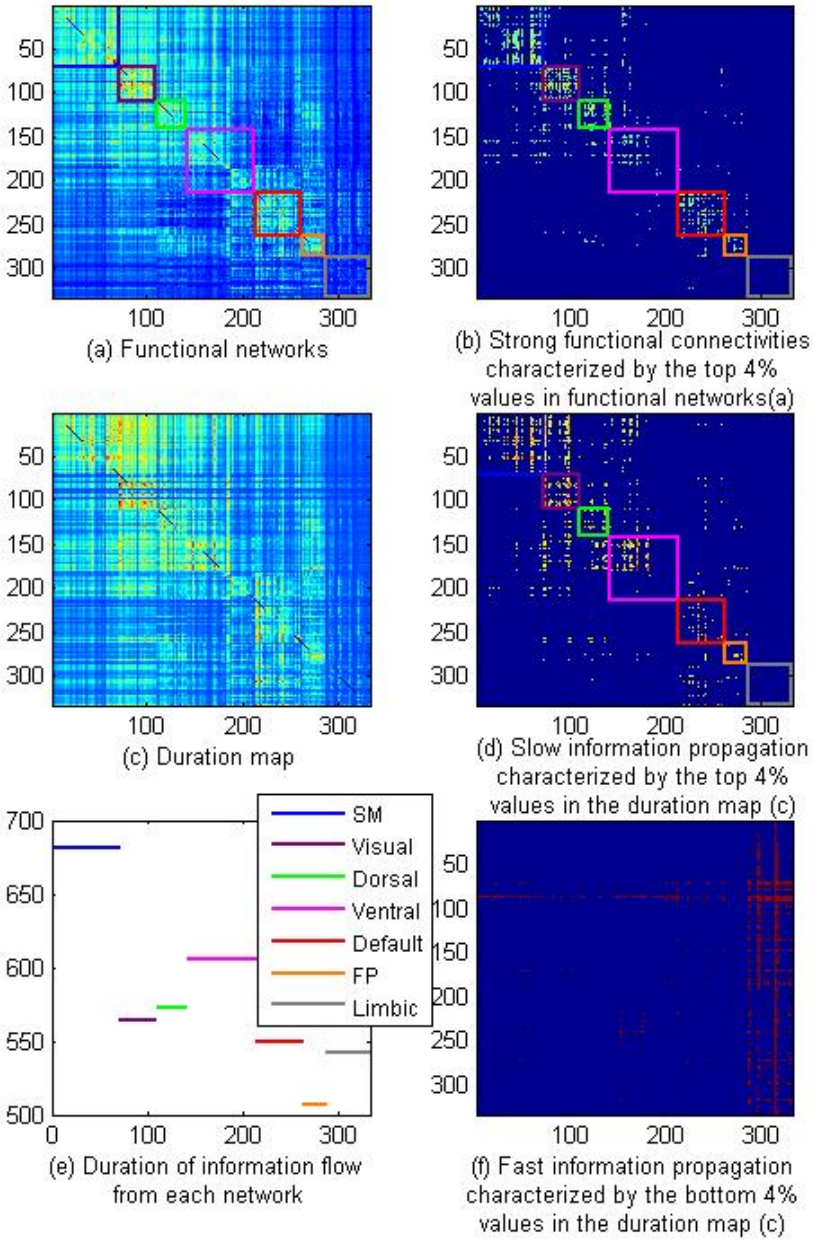

Figure 3.2: Connection weights and duration of resting state functional networks. In these matrices, ROIs along the rows propagate information to the ROIs along the columns. Strong connectivities are mostly in the diagonal blocks of (a) and (b). The duration map (c) is less diagonally oriented comparing to the connectivity map. The longest and the shortest durations are shown in (d) and (f), respectively.

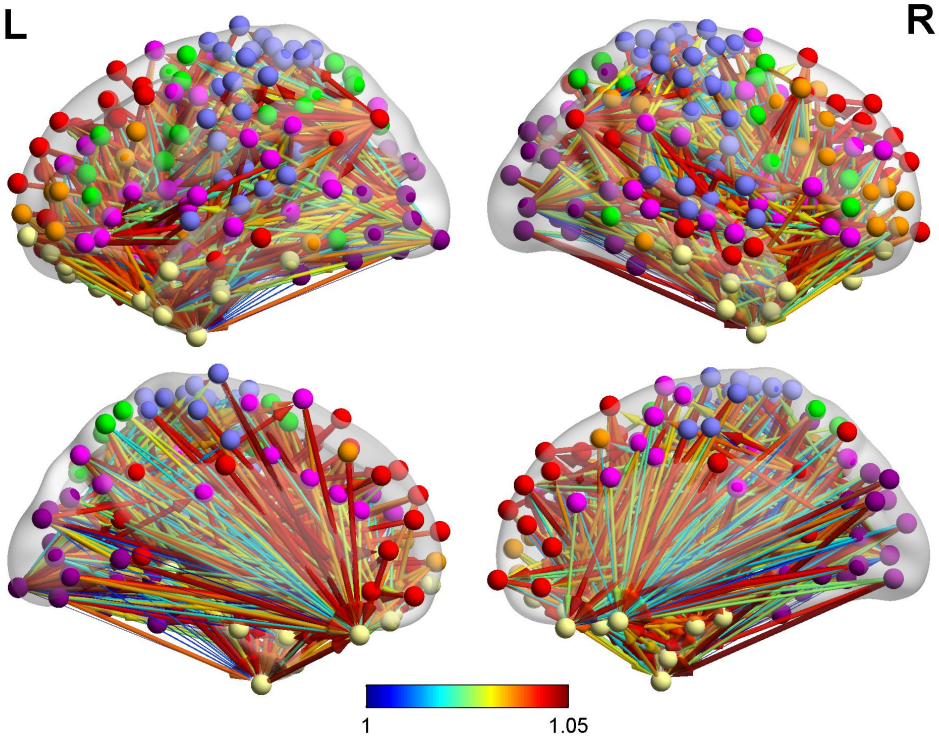

Figure 3.3: The most rapid information propagations, characterized by the top 4% N_{jli} values, in resting brain. Stronger and longer connectivity has a thicker and warmer colored arrow.

ranking	brain systems
1	Frontal Parietal
2	Limbic
3	Default
4	Visual
5	Dorsal attention
6	Ventral attention
7	Somatomotor

Table 3.1: The ranking of average duration of the information flow from the seven well-known functional networks to the rest brain.

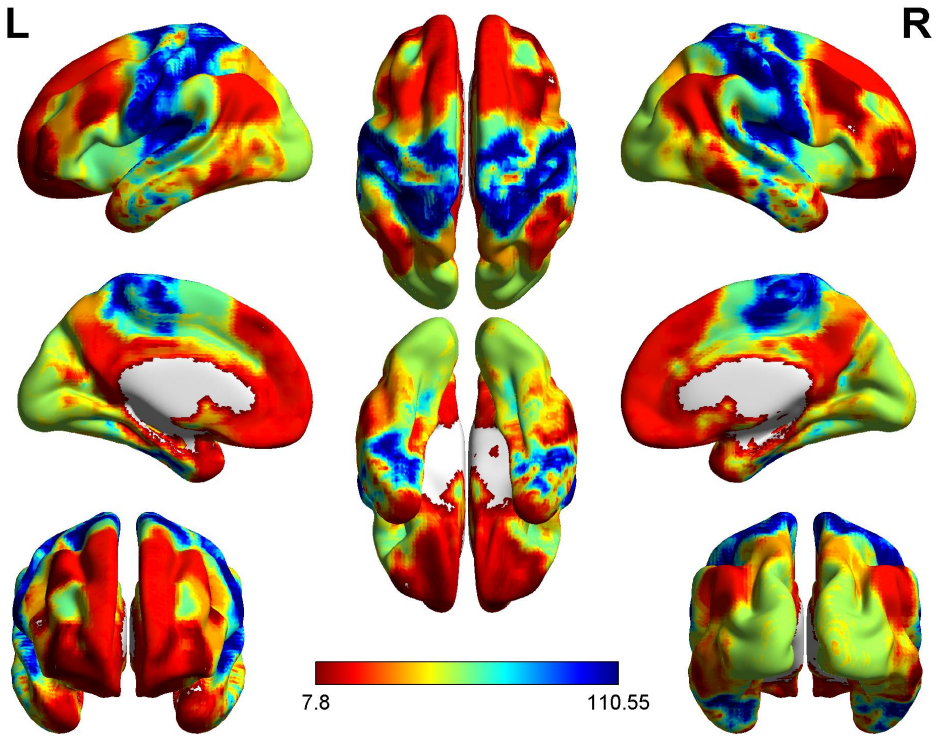

Figure 3.4: The average duration of the information flow from the seven well-known functional networks to the rest brain. The networks have warmer colors if they propagate information more rapidly.

3.4 Discussion

The p-correlation method, which estimates the duration and the direction of information flow, was used to investigate the temporal and spatial interactions in functional brain networks. Specifically, the fast and slow information propagations between different brain regions were characterized.

The results show that the slowest information propagations are dominated by connectivities within the somatomotor, the visual, and the ventral attention systems. In addition, slow and infrequent information propagations from the

somatomotor to the visual system are also recognized. These results agree with the biological facts discovered previously. That is, the activation of visual, motor and attention systems are suppressed in resting human brain [54, 41].

In addition, we provided a global information of interactions among all brain regions. In resting brain, the most rapid information propagations flow into the limbic system. For the first time, we were able to visualized the hypothesis of resting state activity, that is, the medial temporal lobe become awake and rapidly gathering the information from all other brain regions on the cortex.

Furthermore, we determined a ranking of the average duration of the information flow from the well-known resting state functional networks, which suggests that the frontal parietal, the limbic and the default networks propagate the information more rapid than the other networks. All these results numerically validate the biological facts in resting brain. The brain wide variability in the duration of causal influence provides novel insight in brain functions.

CHAPTER 4

REALISTIC SIMULATORS FOR FMRI TIMESERIES

4.1 Introduction

In this chapter, a realistic simulator of fMRI timeseries is introduced. Functional MRI timeseries capture the BOLD signals in human brain, which are generated by brain activities in first the neural level and second the vascular level. Four different mathematical models for brain activities in either the neural or the vascular level are investigated. Two existing simulators got reverse engineered in order to decipher their detailed principles of operation. A new simulator is developed with customized selection on models and parameters. As a result, the new simulator simplified and enhanced the two existing simulators by expanding customer options, especially allowing customers to integrate different components from different simulators into a single calculation.

4.2 Mathematical models of brain functional connectivity

4.2.1 Neural level: generation of neuron activity

A DCM forward model

Dynamic causal modelling (DCM) is first introduced in [44], which describes the generation of neuron timeseires. A simplified DCM forward model is used in Smith simulator [117] to generate the benchmark simulated fMRI data. Specifi-

cally, the simplified DCM model is a linear vector differential equation,

$$\frac{\mathrm{d}z}{\mathrm{d}t}(t) = Az(t) + Cu(t), \tag{4.1}$$

where $z \in \mathbb{R}^N$ is the vector of neural signals, one signal at each of the N ROIs; $A \in \mathbb{R}^{N\times N}$ describes the interconnections of the neural signals; $C \in \mathbb{R}^{N\times N}$ is the matrix of weights describing how the external inputs enter the network; and $u \in \mathbb{R}^N$ is the vector of external inputs to the ROIs.

The initial condition occurs at $t = t_0$ and has value $z(t_0) = z_0 \in \mathbb{R}^N$. For stability, it is necessary that the eigenvalues of A have negative real parts. Often $C = I_N$ where I_N is the $N\times N$ identity matrix. In [117], the matrix A is expressed in the form $A = \sigma A'$ where $\sigma \in \mathbb{R}_+$ and $A'_{i,i} = -1$ so that the within-node temporal decay is controlled by σ (nominal value $\sigma = 0.05$s).

Each of the N components of the external input $u(t)$ is the sum of a random pulse train $u_p(t) \in \mathbb{R}$ and a random Gaussian noise $u_g(t) \in \mathbb{R}$. The random pulse train $u_p(t)$ has transitions at times t_n ($n \in \{0, 1, \dots\}$) where $t_{n+1} - t_n$ are independent realizations of exponential random variables. The random pulse train $u_p(t)$ alternates deterministically between zero and non-zero values starting at zero, i.e., $u_p(t) = 0$ for $t_0 \le t < t_1$. The exponential random variables $t_{n+1} - t_n$ are specified by their rates μ_n or equivalently their means $1/\mu_n$ and have different rates for zero versus for nonzero values of $u_p(t)$:

$$\mu_n = \begin{cases} \mu_-, & n = 2m \text{ (rate when the value is 0)} \\ \mu_+, & n = 2m+1 \text{ (rate when the value is nonzero)} \end{cases} \tag{4.2}$$

where $m \in \{0, 1, \dots\}$ and the nominal values of $1/\mu_-$ and $1/\mu_+$ are 10s and 2.5s, respectively. When $u_p(t)$ is nonzero, i.e., on $t_{2m+1} \le t < t_{2m+2}$ ($m \in \{0, 1, \dots\}$), the value of $u_p(t)$ is v_m where v_m is independent and identically distributed with probability mass function (pmf) f_v. The random Gaussian noise $u_g(t) \in \mathbb{R}$

has mean zero and is white, i.e., its autocorrelation function is $E[u_g(t_1)u_g(t_2)] = \lambda^2\delta(t_1 - t_2)$ where $\delta(t)$ is the Dirac delta function so that its power spectral density is λ^2 at all frequencies. The t_n, v_m, and $u_g(t)$ stochastic processes are independent for each component of $u(t)$, independent between different components of $u(t)$, and independent of the initial condition z_0. Note that this implies that the transitions in the pulse train input to different components of $u(t)$ occur at different times.

For the purpose of computation, this continuous model is approximated by a discrete time model. In particular, approximate the derivative by $(z(t) - z(t-\delta))/\delta$ for a finite step-size δ and define $z_d[n] = z(n\delta)$ which leads to the approximate discrete-time vector difference equation

$$z_d[n] = (I_N + \delta A)z_d[n-1] + \delta C u_d[n]. \tag{4.3}$$

Assuming without loss of generality that $t_0 = 0$, the initial condition for the discrete-time system occurs at $n = 0$ and has value $z_d[0] = z_0$. The vector of external inputs $u(t)$ should also be transformed to discrete time. Since each element of $u(t)$ is the sum of a pulse and a Gaussian component, $u_d[n]$ will likewise be the sum of two components. In the pulse component the exponential random variables $t_{n+1} - t_n$ with rate μ are replaced by geometric random variables $k_{n+1} - k_n$ with parameter $q = \mu\delta$. The deterministic oscillation of μ and the amplitude of the pulses are unchanged. In the Gaussian component the continuous-time Gaussian zero-mean white noise with continuous-time autocorrelation function $E[u_g(t_1)u_g(t_2)] = \lambda^2\delta(t_1 - t_2)$ is replaced by a discrete-time Gaussian zero-mean white noise with discrete-time autocorrelation function $E[u_g(n_1)u_g(n_2)] = (\lambda^2/\delta)\delta_{n_1,n_2}$ where δ_{n_1,n_2} is the Kronecker delta function with value 1 if $n_1 = n_2$ and value 0 otherwise.

Interactive macro neurons

A different model of neuron activity is proposed in [102]. There are N_{ROI} ROIs. Each ROI contains N_{N} macro neurons. The neural signal at time t in the ηth macro neuron of the rth ROI is $z_{r,\eta}(t)$.

The output signal from the rth ROI is $y_r(t)$ which is defined by

$$\begin{aligned} z_r(t) &= \sum_{\eta=1}^{N_{\mathrm{N}}} z_{r,\eta}(t-\delta_r) && (4.4)\\ y_r(t) &= z_r(t) * h(t) && (4.5)\\ &= \int_{\tau=-\infty}^{t} z_r(\tau)h(t-\tau)\mathrm{d}\tau && (4.6)\\ &= \int_{\tau=0}^{\infty} h(\tau)z_r(t-\tau)\mathrm{d}\tau && (4.7) \end{aligned}$$

where $*$ indicates convolution and $h(t)$ is the causal double-gamma HRF, and δ_r are delays which are i.i.d. random variables randomly chosen once at the start of the simulation. The temporal evolution equation for $z_{r,\eta}(t)$ is

$$z_{r,\eta}(t) = g\tanh\left(\{[s_{r,\eta}(t-\tau) + d_{r,\eta}(t-N_\tau\tau)] + e_{1,r,\eta}(t)\}/g\right) + e_{2,r,\eta}(t) \qquad (4.8)$$

where time is discrete, $N_\tau = 4$, and $\tau = 100$ms. The probability law for $e_{1,r,\eta}(\cdot)$ and $e_{2,r,\eta}(\cdot)$ is that

1) $e_{1,r,\eta}(\cdot)$ and $e_{2,r,\eta}(\cdot)$ are independent sequences.

2) $e_{1,r,\eta}(t)$ is i.i.d. (in t) $N(0,\sigma^2_{1,r,\eta})$ where $\sigma_{1,r,\eta}$ is i.i.d. (in r and η) $U(0,30)$.

3) $e_{2,r,\eta}(t)$ is i.i.d. (in r, η, and t) $N(0,\sigma_2^2)$ where $\sigma_2 = 0.3$.

4.2.2 Vascular level: generation of BOLD signals

Both models for the vascular level are continuous time models. We use linear interpolation to transform from the discrete-time neural-level models to contin-

uous time. More specifically, if the discrete time signal is $z_d[n]$ with sampling interval δ then the interpolated continuous time signal is

$$n = \lfloor t/\delta \rfloor \tag{4.9}$$

$$\xi = (t - n\delta)/\delta \tag{4.10}$$

$$z(t) = z_d[n](1 - \xi) + z_d[n + 1]\xi. \tag{4.11}$$

Hemodynamic response function

The hemodynamic response function $h(t)$ is defined b Lindquist *et al.* in [79, Eq. A1]. Specifically,

$$h(t) = A\left(\frac{t^{\alpha_1 - 1}\beta_1^{\alpha_1}\exp(-\beta_1 t)}{\Gamma(\alpha_1)} - c\frac{t^{\alpha_2 - 1}\beta_2^{\alpha_2}\exp(-\beta_2 t)}{\Gamma(\alpha_2)}\right) \tag{4.12}$$

where $\Gamma(\cdot)$ is the gamma function, and the nominal parameter values are $\alpha_1 = 6$, $\alpha_2 = 16$, $\beta_1 = \beta_2 = 1$, $c = 1/6$ and the amplititude A is the only unknown parameter in this model.

Then the ideal BOLD signal for an ROI is the continuous-time convolution of the neural signal at that ROI (an element of $z(t)$) with the hemodynamic response function $h(t)$. Finally, the measured BOLD signal is the ideal BOLD signal plus additive white zero-mean Gaussian noise. Specifically, the BOLD signal, denoted by $s(t)$, is determined by,

$$s(t) = z(t) * h(t) + w(t), \tag{4.13}$$

where $w(t)$ is the white Gaussian noise.

Balloon model

The Balloon model is introduced in [18, 19], and get formulated in [45, 44]. The idea is that increases in flow effectively inflate a venous "balloon" such that deoxygenated blood is diluted and expelled at a greater rate. So, the input of the model is a blood flow in the blood vessel (f_{in}), which is triggered by the neuron activity.

$$\sigma u(t) = \frac{\mathrm{d}f_{in}^2(t)}{\mathrm{d}t^2} + \frac{1}{\tau_s}\frac{\mathrm{d}f_{in}(t)}{\mathrm{d}t} - \frac{f_{in}(t)-1}{\tau_f} \tag{4.14}$$

where σ is the neuronal efficacy; τ_s is the signal decay; τ_f is the autoregulation. The nominal values of these coefficients discussed in [45] are $\sigma = 0.5$, $\tau_s ln(2) = 1067ms$ and $\frac{1}{2\pi\sqrt{\tau_f}} \approx 0.101$.

The blood flow then causes a change in the normalized venous volume (v) and the normalized total deoxyhemoglobin voxel content (q).

$$\tau_0 \frac{\mathrm{d}v(t)}{\mathrm{d}t} = f_{in}(t) - v^{1/\alpha} \tag{4.15}$$

$$\tau_0 \frac{\mathrm{d}q(t)}{\mathrm{d}t} = f_{in}(t)\frac{1-(1-E_0)^{1/f_{in}}}{E_0} - v^{1/\alpha}\frac{q(t)}{v(t)} \tag{4.16}$$

where τ_0 is the transit time and α is the stiffness. The nominal values provided in [45] are $\tau_0 = 0.98s$ and $\frac{1}{\alpha} = 3.03$.

The final BOLD signal (s) is determined by the normalized venous volume (v), normalized total deoxyhemoglobin voxel content q and resting net oxygen extraction fraction by the capillary bed (E_0),

$$s(t) = V_0(k_1(1-q(t)) + k_2(1-\frac{q(t)}{v(t)}) + k_3(1-v(t))) \tag{4.17}$$

$$k_1 = 7E_0 \tag{4.18}$$

$$k_2 = 2 \tag{4.19}$$

$$k_3 = 2E_0 - 0.2, \tag{4.20}$$

where V_0 is the resting blood volume fraction. The nominal values are $E_0 = 0.34$ and $V_0 = 0.02$. The initial conditions for the above four variables are $\frac{\mathrm{d}f_{in}}{\mathrm{d}t}|_{t=0} = 0$, $f_{in}(0) = 0$, $v(0) = 0$ and $q(0) = 0$.

4.3 Results

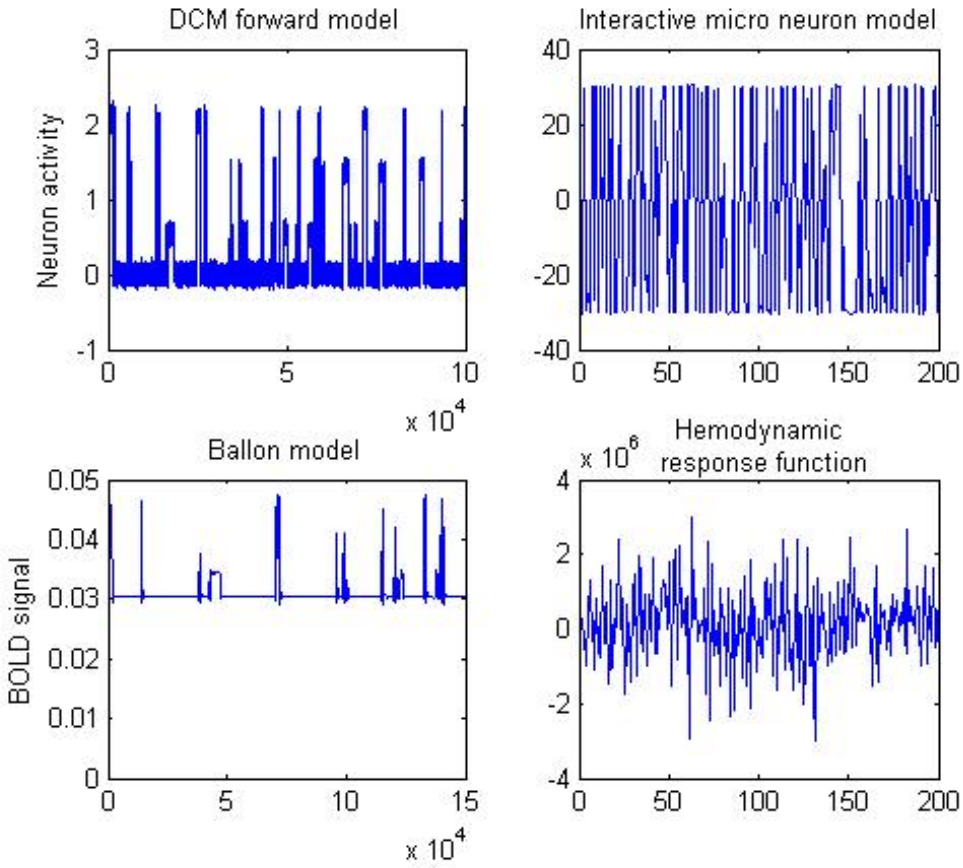

Figure 4.1: Signals generated from each of the four models.

CHAPTER 5

COMPUTATION OF REAL BASIS FUNCTIONS FOR THE 3-D ROTATIONAL POLYHEDRAL GROUPS T, O, AND I

5.1 Introduction

3-D rotational symmetry under a finite group G of rotations arises in several situations such as quasi-crystals, fullerenes, and viruses. One method for representing such objects is an orthonormal expansion in basis functions where each basis function has a specific behavior under the operations of G. If the object is invariant under the operations of G, then each basis function should transform according to the identity irreducible representation (irrep) of G ("invariant basis") and such basis functions have been extensively studied [40, 89, 5, 84, 25, 37, 57, 64, 69, 75, 27, 103, 145, 38]. In more complicated situations, the object is not invariant under the operations of G and a larger set of basis functions is needed, specifically, a set that includes functions that transform according to each of the irreps of G ("all irreps basis") and such basis functions have also been studied [25, 89, 27, 103]. Our motivating problem, a structural biology problem described in Section 2, is an example of the more complicated situation. We provide a practical computational algorithm for a set of basis functions with the following properties:

1. Each function in the basis is a linear combination of spherical harmonics[1] of a fixed degree l.

[1] Throughout this paper, spherical harmonics are denoted by $Y_{l,m}(\theta, \phi)$ where the degree l satisfies $l \in \{0, 1, \dots\}$, the order m satisfies $m \in \{-l, \dots, l\}$ and (θ, ϕ) are the angles of spherical coordinates with $0 \le \theta \le \pi$ and $0 \le \phi \le 2\pi$ [92, Section 14.30, pp. 378–379].

2. Each function in the basis is real-valued.

3. The basis functions are orthonormal.

4. Under the rotations of a finite symmetry group, each function in the basis transforms according to one row of the corresponding irreducible representation (irrep) matrices.

Because our structural biology problem includes the structure of viruses, which often exhibit the symmetry of a Platonic solid [29], we focus on the three rotational polyhedral groups, the tetrahedral T, octahedral O, and icosahedral I groups. In the cases of the octahedral and icosahedral groups, it is possible to find a set of basis functions which is complete in the space of square-integrable functions on the surface of the sphere and which satisfies Properties 1–4. However, in the case of the tetrahedral group, it is not possible to find a set of basis functions that is both complete and which satisfies Properties 1–4 (Section 5.4) and one way in which to achieve completeness is to added additional complex-valued functions which is an undesirable situation for our structural biology application (Section 5.2). The finite subgroups of SO_3 are T, O, I, the cyclic groups C_n, and the dihedral groups D_n [8, Theorem 19.2, p. 105]. The T, O, and I basis functions can naturally and efficiently be computed in spherical coordinates with spherical harmonics and that is the focus of this paper. It is likely that the C_n basis functions, and possibly the D_n basis functions, are more naturally and efficiently computed in cylindrical coordinates with cylindrical harmonics and for that reason also they are not discussed.

In the majority of existing literature, basis functions of a symmetry group have been generated as a linear combination of spherical harmonics of a single degree [5, 6, 7, 88, 99, 89, 40, 145, 147], because of the importance of ro-

tations and the relative simplicity of rotating spherical harmonics. Spherical harmonics have been widely applied in structural biology, e.g., the fast rotation function [30]. Other work express the basis functions of a rotational polyhedral group as multipole expansions in rectangular coordinates [65, 56]. Previous work uses a variety of techniques and often has a restriction on the value l of the spherical harmonics [5, 6, 7, 88, 99, 25, 89, 27, 103]. For instance, Refs. [5, 6, 7] consider a range of point groups and use the techniques of projection operators and Wigner D transformations to compute basis functions up to degree $l = 12$, while Ref. [25] uses similar techniques restricted to the icosahedral group to provide basis functions up to degree $l = 15$. Refs. [88, 99] use the method of representation transformation to compute the invariant basis functions of the cubic group up to degree $l = 30$; the work of Ref. [89] extends this computation to all irreps basis functions. Refs. [27, 103] propose a method for deriving all irreps basis functions of the cubic and the icosahedral groups for a specific degree l. However, for computation which needs all irreps basis functions for a large range of l values (e.g., from 1 to 55), the one-by-one derivation is cumbersome. Later work [40, 145, 147] release this restriction on the degree l and allow for the computation of the invariant basis functions of any rotational polyhedral group. However, the recursions in [145, 147] appear to be unstable in computational experiments.

In this paper we derive an algorithm for efficiently computing the all irreps basis functions for the tetrahedral, octahedral, and icosahedral groups for arbitrary value of l. The algorithm is not recursive, so stability is not an issue, and the most burdensome calculation in the algorithm is to determine the eigenvectors of a real symmetric matrix that is of dimension $2d_p$ where d_p is the dimension of the pth irrep which, for the groups we consider, is no larger than 5. To

compute functions satisfying Properties 1–4, we determine real-valued generalized projection operators [28, p. 93] and apply them to real-valued spherical harmonics (Section 5.4). To determine real-valued generalized projection operators, we first determine real-valued irrep matrices. Standard approaches exist, e.g., Young diagrams [46]. However, taking advantage of existing complex-valued irrep matrices [9, 80], we derive an algorithm to find a similarity matrix that transforms the potentially-real complex-valued irrep matrices to real-valued irrep matrices (Section 5.3). We also demonstrate that functions satisfying Properties 1–4 exist if and only if real-valued irrep matrices exist (Section 5.5) and provide numerical examples (Section 5.6).

The following notation is used throughout the paper. Let M be a matrix. Then M^* is the complex conjugate of M, M^T is the transpose of M, and M^H is the Hermitian transpose of M, i.e., $(M^T)^*$. $I_n \in \mathbb{R}^{n\times n}$ is the identity matrix. $\mathfrak{R}$ and $\mathfrak{I}$ are the real and imaginary parts, respectively, of their arguments. "Representation" and "Irreducible representation" are abbreviated by "rep" and "irrep", respectively. For 3-D vectors, $x = \|\mathbf{x}\|_2$ and $\mathbf{x}/x$ is shorthand for the (θ, ϕ) angles in the spherical coordinate system. Integration of a function $f : \mathbb{R}^3 \to \mathbb{C}$ over the surface of the sphere in $\mathbb{R}^3$ is denoted by $\int f(\mathbf{x})\mathrm{d}\Omega$ meaning $\int_{\theta=0}^{\pi}\int_{\phi=0}^{2\pi} f(x,\theta,\phi)\sin\theta \mathrm{d}\theta\mathrm{d}\phi$. The Kronecker delta function is denoted by $\delta_{i,j}$ and has value 1 if $i = j$ and value 0 otherwise.

5.2 Motivation

Single-particle cryo electron microscopy (cryo EM) [11, 24, 23] provides essentially a noisy 2-D projection in an unknown direction of the 3-D electron scatter-

ing intensity of a 10^1–10^2 nm biological object such as a ribosome or a virus. For studies with high spatial resolution, only one image is taken of each instance of the object because the electron beam rapidly damages the object. There are multiple software systems, e.g., Refs. [42, 81, 112], for computing a 3-D reconstruction of the object from sets of images of different instances of the object and these systems include the possibility that the instances come from a small set of classes where all instances within one class are identical (discrete heterogeneity). Not only may there be multiple classes of heterogeneity, but each instance within a class may vary due to, for example, flexibility (continuous heterogeneity). By describing the electron scattering intensity by a real-valued Fourier series with coefficients which are random variables and solving a maximum likelihood estimation problem for the mean vector and covariance matrix of the coefficients, we have a theory [148] and several examples [133, 124, 51] demonstrating the ability to characterize the continuous heterogeneity.

Symmetry is sometimes an important feature of a biological object. An important example for viruses is icosahedral symmetry [20]. If all instances are identical or if all instances within each class are identical (discrete heterogeneity), it is natural to impose the symmetry on the electron scattering intensity of the object. However, if each instance in the class is different (continuous heterogeneity) it is more natural to impose the symmetry on the *statistics* of the electron scattering intensity rather than imposing the symmetry on the electron scattering intensity itself [148, Eqs. 55–56]. A sufficient method to achieve symmetric statistics in the case of icosahedral symmetry is to use basis functions in the Fourier series such that each basis function has icosahedral symmetry. Such basis functions are known [147] and were used in the examples [133, 124, 51] referred to above. However, this is not a necessary and sufficient approach to

achieving symmetric statistics. In particular, using basis functions where each function has the symmetry implies that each instance of the object has the symmetry while it is more natural to assume that the instances lack the symmetry and the symmetry only appears in the expectations that lead to the statistics. This requires constraints on the mean and covariance of the coefficients and the constraints are simplest if each basis function transforms under rotations of the group as some row of some irreducible representation of the group (Eq. 5.7) and if all of the basis functions are real valued (Eq. 5.9) [137] and these two goals are the primary topic of this paper. Using harmonic functions (Eq. 5.8) helps characterize the spatial resolution of the estimated electron scattering intensity and leads to simple formulas for both the electron scattering intensity and the 3-D Fourier transform of the electron scattering intensity. Using orthonormal functions (Eq. 5.10) improves the numerical properties of the inverse problem.

Our focus on real-valued basis functions comes from the fact that the electron scattering intensity is real valued and therefore, if the basis functions are also real valued, then the coefficients can be real valued which simplifies the statistical estimation problem in two ways. Suppose c (a column vector containing the coefficients) must be complex. The first complication is that it is necessary to estimate both the expectation of cc^T and of cc^H. The second complication is that it is necessary to account for constraints on the allowed values of c, much like a 1-D Fourier series for a real-valued function that is periodic with period T requires that the coefficients (denoted by c_n) satisfy $c_n = c_{-n}^*$ when the basis functions for the Fourier series are $\exp(i(2\pi/T)nt)$. Our focus on real-valued basis functions which allow real-valued coefficients permits us to avoid both of these complications for the important case of the icosahedral group.

5.3 Computation of real irrep matrices

Starting from a set of matrices that make up a complex-valued unitary irrep, the goal of this section is to compute, if possible, a similarity transformation such that the similarity transformation applied to the known complex-valued unitary irrep is a real-valued orthonormal irrep. The question of existence is answered by the Frobenious-Schur theory [28, p. 129, Theorem III] as follows. Let $\Gamma_C^p(g)$ ($g \in G$) be the known matrices. Compute the Frobenious-Schur indicator, denoted by χ, which is defined by $\chi(\{\Gamma_c^p(g)\}_{g\in G}) = (1/N_g)\sum_{g\in G} \mathrm{tr}[\Gamma_c^p(g)]$ where N_g is the number of elements in G. The value of χ is 1, 0, or -1 with the following implications. If $\chi = 1$ then the irrep is potentially real meaning that there exists a unitary matrix, that is denoted by S^p, such that $(S^p)^H\Gamma^p(g)S^p$ is real for all $g \in G$. If $\chi = 0$ then the irrep is pseudo real meaning that there exists a unitary matrix, that is denoted by T^p, such that $(\Gamma^p(g))^* = (T^p)^H\Gamma^p(g)T^p$ for all $g \in G$ but no similarity transformation exists that makes the irrep real as occurs when $\chi = 1$. If $\chi = -1$ then the irrep is essentially complex meaning that there is no similarity transformation that relates Γ^p and $(\Gamma^p)^*$. The remainder of this section applies only to potentially real irreps. Because any set of matrices that make up a real-valued orthonormal irrep is satisfactory for the purposes of this paper, the question of uniqueness does not arise. In the remainder of the section, we describe a three-step algorithm to compute such a unitary matrix $S^p \in \mathbb{C}^{d_p\times d_p}$ for the case of potentially real irreps:

1. For any such unitary matrix S^p, show that the complex irrep Γ_c^p is similar to its complex conjugate $(\Gamma_c^p)^\star$ with the similarity transformation $S^p(S^p)^T$.
2. Find a matrix C^p, which is an explicit function of Γ_c^p, and is a similarity

matrix relating the two sets of matrices Γ_c^p and $(\Gamma_c^p)^\star$.

3. Factor C^p to compute a particular S^p.

Step 1 is achieved by Lemma 1.

Lemma 1. *Suppose that $\Gamma_c^p(g)$ $(g \in G)$ are complex unitary irrep matrices for the pth rep of the group G which is potentially real. Let $S^p \in \mathbb{C}^{d_p \times d_p}$ denote a unitary matrix. The following two statements are equivalent:*

$$\text{For all } g \in G,\ \Gamma_r^p(g) = (S^p)^H \Gamma_c^p(g) S^p \text{ such that } \Gamma_r^p(g) \in \mathbb{R}^{d_p \times d_p}. \tag{5.1}$$

$$\text{For all } g \in G,\ [S^p (S^p)^T]^{-1} \Gamma_c^p(g) [S^p (S^p)^T] = (\Gamma_c^p(g))^*. \tag{5.2}$$

Please see Appendix A.1 for the proof.

Step 2 computes a non-unitary symmetric matrix (Z^p) (Lemma 2), which is then normalized (C^p) to be unitary (Corollary 1).

Lemma 2. *Suppose that $\Gamma_c^p(g)$ $(g \in G)$ are complex unitary irrep matrices for the pth rep of the group G which is potentially real. Let $A^p \in \mathbb{C}^{d_p \times d_p}$ be a nonsingular transpose-symmetric matrix (i.e., $(A^p)^T = A^p$) and Z^p be defined by Eq. 5.3, specifically,*

$$Z^p = \frac{1}{N_g} \sum_{g \in G} \Gamma_c^p(g) A^p ((\Gamma_c^p(g))^*)^{-1}. \tag{5.3}$$

If Z^p is nonzero, then Z^p has the following properties:

1. $(Z^p)^T = Z^p$.
2. $(Z^p)^* Z^p = c_Z I_{d_p}$ *where* $c_Z \in \mathbb{R}^+$.
3. *For all* $g \in G$, $(\Gamma_c^p(g))^* = (Z^p)^* \Gamma_c^p(g) Z^p$.

Please see Appendix A.1 for the proof.

It is important to find a matrix A^p such that the matrix Z^p is nonzero. For the three rotational polyhedral groups that we consider in this paper, this issue is discussed in Section 5.6.1.

Corollary 1. *Define C^p by*

$$C^p = Z^p / \sqrt{c_Z}. \tag{5.4}$$

Then C^p has the following properties:

1. $(C^p)^T = C^p$.
2. $(C^p)^* C^p = I_{d_p}$.
3. *For all $g \in G$,* $(\Gamma_c^p(g))^* = (C^p)^* \Gamma_c^p(g) C^p$.

The matrix S^p in the definition of potentially real is not unique. Comparing Property 3 of Corollary 1 and Eq. 5.2, S^p can be restricted to satisfy

$$C^p = S^p (S^p)^T \tag{5.5}$$

noting, however, that even with this restriction, S^p is still not unique. Because Lemma 1 is "if and only if", any unitary matrix S^p that satisfies Eq. 5.5 is a satisfactory similarity matrix. The existence of the unitary factorization described by Eq. 5.5 is guaranteed by the Takagi Factorization (Ref. [59, Corollary 4.4.6, p. 207]).

Step 3 is to perform the factorization of C^p and a general algorithm is provided by Lemma 3 which is based on the relationship between the coneigenvectors of a unitary symmetric matrix Q and the eigenvectors of its real representation matrix B, which is defined by $B = \begin{bmatrix} \Re Q & \Im Q \\ \Im Q & -\Re Q \end{bmatrix} \in \mathbb{R}^{2n \times 2n}$.

Lemma 3. *Let $Q \in \mathbb{C}^{n\times n}$ be a unitary symmetric matrix, i.e., $Q^T = Q$ and $QQ^* = I_n$. Let $B \in \mathbb{R}^{2n\times 2n}$ be the real representation of Q, i.e., $B = \left[\begin{smallmatrix} \Re Q & \Im Q \\ \Im Q & -\Re Q \end{smallmatrix}\right] \in \mathbb{R}^{2n\times 2n}$. Then, the following properties hold:*

1. *B is nonsingular and has $2n$ real eigenvalues and $2n$ orthonormal eigenvectors.*
2. *The eigenvectors and eigenvalues of B are in pairs, specifically,*

$$B\left[\begin{smallmatrix} x \\ -y \end{smallmatrix}\right] = \lambda\left[\begin{smallmatrix} x \\ -y \end{smallmatrix}\right] \text{ if and only if } B\left[\begin{smallmatrix} y \\ x \end{smallmatrix}\right] = -\lambda\left[\begin{smallmatrix} y \\ x \end{smallmatrix}\right].$$

3. *Let $\left[\begin{smallmatrix} x_1 \\ -y_1 \end{smallmatrix}\right], \ldots, \left[\begin{smallmatrix} x_n \\ -y_n \end{smallmatrix}\right]$ be the orthonormal eigenvectors of B associated with n positive eigenvalues of $\lambda_1, \ldots, \lambda_n$. (Since B is nonsingular, there are no zero eigenvalues.) Then $x_1 - iy_1, \ldots, x_n - iy_n$ are the set of orthonormal coneigenvectors of Q associated with the n coneigenvalues of $+\lambda_k$, i.e., $Q(x_k - iy_k)^* = \lambda_k(x_k - iy_k)$ for $k = 1, ..., n$.*
4. *$\lambda_1 = \cdots = \lambda_n = 1$.*
5. *Define $u_k = x_k - iy_k$ and $U = [u_1, \ldots, u_n] \in \mathbb{C}^{n\times n}$. Then U is unitary.*
6. *$Q = UU^T$.*

Please see Appendix A.1 for the proof.

Applying Lemma 3 to C^p results in a particular matrix S^p which is the U matrix of Property 5. The complete algorithm is summarized in Theorem 1.

Theorem 1. *A unitary matrix, $S^p \in \mathbb{C}^{d_p\times d_p}$, which is a similarity transformation between the provided potentially-real complex unitary irrep and a real orthonormal irrep, can be computed by the following steps:*

1. *Compute Z^p by Eq. 5.3.*

2. *Compute c_Z by Lemma 2 Property 3 and compute C^p by Eq. 5.4.*

3. *Compute the eigenvectors and eigenvalues of*

$$B^p = \begin{bmatrix} \Re C^p & \Im C^p \\ \Im C^p & -\Re C^p \end{bmatrix} \in \mathbb{R}^{2d_p \times 2d_p}. \tag{5.6}$$

4. *Form the matrix $V^p \in \mathbb{R}^{2d_p \times d_p}$ whose columns are the d_p eigenvectors of B^p that have positive eigenvalues.*

5. *Then $S^p = [I_{d_p}, iI_{d_p}]V^p$.*

5.4 Computation of real basis functions

In this section, formulas corresponding to the four goals in Section 5.1 are stated in Eqs. 5.8–5.11 and the computation of basis functions satisfying these formulas is then described. The mathematical goal corresponding to Item 4 in Section 5.1 requires the the following definition:

Definition 1. *([28, Eq. 1.26, p. 20]) A basis function that transforms as the nth row ($n \in \{1, \dots, d_p\}$) of the pth rep ($p \in \{1, \dots, N_{\text{rep}}\}$) of the finite group G, denoted by $F_{p,n} \in \mathbb{C}$, is a function such that*

$$F_{p,n}(R_g^{-1}\mathbf{x}/x) = \sum_{m=1}^{d_p} (\Gamma^p(g))_{m,n} F_{p,m}(\mathbf{x}/x) \text{ for all } g \in G, \tag{5.7}$$

where $R_g \in \mathbb{R}^{3\times 3}$ is the 3-D rotation matrix corresponding to $g \in G$ and $\Gamma^p(g)_{g\in G}$ are the unitary irrep matrices of the pth rep.

The basis functions which satisfy the four goals in Section 5.1 have four indices: which irreducible representation (p), which subspace defined by spherical harmonics of fixed order l (l), which vector (n), and which component of the

vector (j). Let $F_{p,l,n,j}$ be a basis function that transforms as the jth row of the irrep matrices and $F_{p,l,n} = (F_{p,l,n,j=1}, \ldots, F_{p,l,n,j=d_p})^T$. Let $Y_{l,m}(\theta, \phi)$ be the spherical harmonic of degree l and order m [92, Section 14.30, pp. 378–379]. Then the goals are to obtain a set of functions such that

$$F_{p,l,n,j}(\theta, \phi) = \sum_{m=-l}^{+l} c_{p,l,n,j,m} Y_{l,m}(\theta, \phi) \tag{5.8}$$

$$F_{p,l,n,j}(\theta, \phi) \in \mathbb{R} \tag{5.9}$$

$$\delta_{p,p'}\delta_{l,l'}\delta_{n,n'}\delta_{j,j'} = \int_{\phi=0}^{2\pi}\int_{\theta=0}^{\pi} F_{p,l,n,j}(\theta, \phi) F_{p',l',n',j'}(\theta, \phi) \sin\theta \mathrm{d}\theta\mathrm{d}\phi \tag{5.10}$$

$$F_{p,l,n}(R_g^{-1}\mathbf{x}/x) = (\Gamma^p(g))^T F_{p,l,n}(\mathbf{x}/x). \tag{5.11}$$

The computation is performed by the projection method of Ref. [28, p. 94] in which various projection operators (Definition 2) are applied to each function of a complete basis for the space of interest. When the various projection operators are defined using real-valued orthonormal irrep matrices (as computed in Section 5.3) and are applied to a real-valued complete orthonormal basis in the subspace spanned by spherical harmonics of degree l (which has dimension $2l + 1$) then the resulting basis for the same subspace is real-valued, complete, and orthonormal [28, Theorems I and II, pp. 92-93] [2].

The remainder of this section has the following organization. First, the projection operators are defined (Definition 2). Second, the initial basis in the subspace is described. Third, the results of applying the projection operators to the basis functions are described in terms of individual functions (Lemma 4) and in terms of sparse matrices of order $(2l + 1) \times (2l + 1)$. Fourth, normalization is discussed (Eq. 5.22). Fifth, too many basis functions are computed by this process, i.e., more than $2l+1$, so Gram-Schmidt orthogonalization is used to extract a subset containing $2l + 1$. Finally, sixth, comments are made on the non-uniqueness

[2] Similar result is proven for Lemma 6 in Appendix A.1.

of the final basis.

Definition 2. *The projection operators $\mathcal{P}^p_{j,k}$ are defined by [28, Eq. 5.2, p. 93]*

$$\mathcal{P}^p_{j,k} = \frac{d_p}{N_g} \sum_{g \in G} (\Gamma^p(g))^*_{j,k} P(g) \tag{5.12}$$

where $\Gamma^p(g) \in \mathbb{C}^{d_p \times d_p}$ for all $g \in G$ are the irrep matrices and $P(g)$ is the abstract rotation operator, specifically,

$$P(g) f(\mathbf{x}) = f(R_g^{-1}\mathbf{x}) \tag{5.13}$$

where $R_g \in \mathbb{R}^{3\times 3}$ with $R_g^{-1} = R_g^T$ and $\det R_g = +1$ is the rotation matrix corresponding to $g \in G$. When $P(g)$ is applied to a vector-valued function, it operates on each component of the vector.

The projection operator is applied to a set of basis functions. One natural choice is the set of spherical harmonics [92, Eq. 14.30.1, p. 378] (denoted by $Y_{l,m}(\theta, \phi)$, where the arguments will routinely be suppressed) because $Y_{l,m}$ have simple rotational properties. However, except for $Y_{l,m=0}$, spherical harmonics are complex valued. Older literature [87, Eq. 10.3.25, p. 1264] used real-valued definitions, e.g.,

$$\check{Y}_{l,m}(\theta, \phi) = \begin{cases} \sqrt{2}\Im Y_{l,m}(\theta, \phi), & m < 0 \\ Y_{l,0}(\theta, \phi), & m = 0 \\ \sqrt{2}\Re Y_{l,m}(\theta, \phi), & m > 0 \end{cases}, \tag{5.14}$$

which retain simple rotational properties. We will derive basis functions that satisfy the four goals of Section 5.1 in terms of $\check{Y}_{l,m}$, because they are real-valued, but also describe our results in terms of $Y_{l,m}$, because much standard software is available. Both $Y_{l,m}$ and $\check{Y}_{l,m}$ are orthonormal systems of functions. The $Y_{l,m}$ functions have the symmetry property $Y_{l,-m}(\theta, \phi) = (-1)^m Y^*_{l,m}(\theta, \phi)$ [92, Eq. 14.30.6, p. 378] and the rotational property

$$P(R) Y_{l,m}(\theta, \phi) = \sum_{m'=-l}^{+l} D_{l,m,m'}(R) Y_{l,m'}(\theta, \phi) \tag{5.15}$$

where (1) R is a rotation matrix ($R \in \mathbb{R}^{3\times3}$ with $R^{-1} = R^T$ and $\det R = +1$), (2) $D_{l,m,m'}(R)$ are the Wigner D coefficients [106, Eq. 4.8, p. 52], and (3) $P(R)$ is the rotation operator $P(R)f(\mathbf{x}) = f(R^{-1}\mathbf{x})$.

Standard computations based on the properties described in the previous paragraph result in Lemma 4.

Lemma 4. *Suppose that the pth rep of a group G is potentially real with the real-valued orthogonal irrep matrices $\Gamma^p_r(g) \in \mathbb{R}^{d_p\times d_p}$ for all $g \in G$. Then, the projection operation on real spherical harmonics $\check{Y}_{l,m}$ for $m \in \{-l,\ldots,l\}$ and $l \in \mathbb{N}$ can be determined by*

$$\mathcal{P}^p_{j,k}\check{Y}_{l,m}(\theta,\phi) = \sum_{m'=-l}^{+l}\check{\mathcal{D}}^p_{j,k;l,m;m'}\check{Y}_{l,m'}(\theta,\phi) \tag{5.16}$$

$$= \sum_{m'=-l}^{+l}\hat{\mathcal{D}}^p_{j,k;l,m;m'}Y_{l,m'}(\theta,\phi) \tag{5.17}$$

where

$$\check{\mathcal{D}}^p_{j,k;l,m;m'} = \frac{d_p}{N_g}\sum_{g\in G}(\Gamma^p_r(g))_{j,k}\check{D}_{l,m,m'}(R_g), \tag{5.18}$$

$$\hat{\mathcal{D}}^p_{j,k;l,m;m'} = \frac{d_p}{N_g}\sum_{g\in G}(\Gamma^p_r(g))_{j,k}\hat{D}_{l,m,m'}(R_g), \tag{5.19}$$

$$\hat{D}_{l,m,m'} = \begin{cases} -\frac{i}{\sqrt{2}}\left(D_{l,m,m'} - (-1)^m D_{l,-m,m'}\right), & m<0 \\ D_{l,0,m'}, & m=0 \\ \frac{1}{\sqrt{2}}\left(D_{l,m,m'} + (-1)^m D_{l,-m,m'}\right), & m>0 \end{cases}, \tag{5.20}$$

and

$$
\begin{aligned}
&\check{D}_{l,m,m'} \\
&= \begin{cases}
\frac{1}{2}\left[D_{l,m,m'} - (-1)^m D_{l,-m,m'} - (-1)^{m'} D_{l,m,-m'} + (-1)^{m+m'} D_{l,-m,-m'}\right], & m<0, m'<0 \\
-\frac{i}{\sqrt{2}}\left[D_{l,m,0} - (-1)^m D_{l,-m,0}\right], & m<0, m'=0 \\
-\frac{i}{2}\left[D_{l,m,m'} - (-1)^m D_{l,-m,m'} + (-1)^{m'} D_{l,m,-m'} - (-1)^{m+m'} D_{l,-m,-m'}\right], & m<0, m'>0 \\
\frac{i}{\sqrt{2}}\left[D_{l,0,m'} - (-1)^{m'} D_{l,0,-m'}\right], & m=0, m'<0 \\
D_{l,0,0}, & m=0, m'=0 \\
\frac{1}{\sqrt{2}}\left[D_{l,0,m'} + (-1)^{m'} D_{l,0,-m'}\right], & m=0, m'>0 \\
\frac{i}{2}\left[D_{l,m,m'} + (-1)^m D_{l,-m,m'} - (-1)^{m'} D_{l,m,-m'} - (-1)^{m+m'} D_{l,-m,-m'}\right], & m>0, m'<0 \\
\frac{1}{\sqrt{2}}\left[D_{l,m,0} + (-1)^m D_{l,-m,0}\right], & m>0, m'=0 \\
\frac{1}{2}\left[D_{l,m,m'} + (-1)^m D_{l,-m,m'} + (-1)^{m'} D_{l,m,-m'} + (-1)^{m+m'} D_{l,-m,-m'}\right], & m>0, m'>0
\end{cases}
\end{aligned}
\tag{5.21}
$$

An alternative view of Lemma 4 is described in this paragraph. Define the vectors $Y_l = (Y_{l,-l}, \ldots, Y_{l,+l})^T \in \mathbb{C}^{2l+1}$ and $\check{Y}_l = (\check{Y}_{l,-l}, \ldots, \check{Y}_{l,+l})^T \in \mathbb{R}^{2l+1}$. There exists a unitary matrix $U_l \in \mathbb{C}^{(2l+1)\times(2l+1)}$ such that $\check{Y}_l(\theta,\phi) = U_l^H Y_l(\theta,\phi)$ where U_l has at most two non-zero entries in any row or any column. The Wigner D coefficients can be grouped into a matrix $D_l(R) \in \mathbb{C}^{(2l+1)\times(2l+1)}$ such that $P(R)Y_l(\theta,\phi) = D_l(R)Y_l(\theta,\phi)$ where $D_l(R)$ is typically a full matrix. In terms of these two matrices, (1) $P(R)\check{Y}_l(\theta,\phi) = \hat{D}_l(R)Y_l(\theta,\phi)$ where $\hat{D}_l(R) \in \mathbb{C}^{(2l+1)\times(2l+1)}$ is defined by $\hat{D}_l(R) = U_l^H D_l(R)$ and (2) $P(R)\check{Y}_l(\theta,\phi) = \check{D}_l(R)\check{Y}_l(\theta,\phi)$ where $\check{D}_l(R) \in \mathbb{C}^{(2l+1)\times(2l+1)}$ is defined by $\check{D}_l(R) = U_l^H D_l(R) U_l$. The matrix equations $\hat{D}_l(R) = U_l^H D_l(R)$ and $\check{D}_l(R) = U_l^H D_l(R) U_l$ are equivalent to Eqs. 5.20 and 5.21, respectively, but Eqs. 5.20 and 5.21 are less expensive to compute because of the sparseness of U_l.

A vector of d_p normalized real basis functions, denoted by $C^p_{k,l,m}(\theta,\phi) \in \mathbb{R}^{d_p}$ and expressed in terms of $Y_{l,m}$ (not $\check{Y}_{l,m}$), can be computed from Lemma 4

(Eq. 5.17) as follows [28, p. 94],

$$C^p_{k,l,m}(\theta,\phi) = \frac{1}{\hat{c}^p_{k,l,m}} \begin{bmatrix} \mathcal{P}^p_{1,k} Y_{l,m}(\theta,\phi) \\ \vdots \\ \mathcal{P}^p_{d_p,k} Y_{l,m}(\theta,\phi) \end{bmatrix} = \hat{\mathcal{D}}^p_{l,m} Y_l(\theta,\phi), \tag{5.22}$$

where $(\hat{\mathcal{D}}^p_{l,m})_{j,m'} = \hat{\mathcal{D}}^p_{j,k,l,m,m'} / \hat{c}^p_{k,l,m}$ for $j \in \{1,\ldots,d_p\}$, $m' \in \{-l,\ldots,l\}$, and $\hat{c}^p_{k,l,m} = \sqrt{\sum_{m'=-l}^{l} |\hat{\mathcal{D}}^p_{k,k,l,m,m'}|^2}$ all for some $k \in \{1,\ldots,d_p\}$ such that $\hat{c}^p_{k,l,m} > 0$.

Note that this procedure computes $2l+1$ coefficient matrices by varying m through the set $\{-l,\ldots,+l\}$, so that a total of $(2l+1)d_p$ basis functions are computed, which is more than is necessary for a basis since the subspace of square-integrable functions on the surface of the sphere where the subspace is defined by degree $l \in \mathbb{N}$ is spanned by $(2l+1)$ basis functions. Through Gram-Schmidt orthogonalization, the set of coefficient matrices, $\hat{\mathcal{D}}^p_{l,m}$ for $m \in \{-l,\ldots,l\}$, shrinks to a smaller set of coefficient matrices, $\hat{\boldsymbol{\mathcal{H}}}^p_{l,n}$ for $n \in \{1,\ldots,N_{p;l} < 2l+1\}$. The value of $N_{p;l} \in \mathbb{N}$ is determined by this process. Replacing $Y_{l,m}$ (Y_l) by $\check{Y}_{l,m}$ ($\check{Y}_l$) and using Lemma 4 (Eq. 5.16) instead of Lemma 4 (Eq. 5.17) leads via the same ideas to a set of real orthonormal coefficient matrices $\{\check{\boldsymbol{\mathcal{H}}}^p_{l,n}\}_{n=1}^{N_{p;l}}$. Finally, two expressions for the vector of d_p orthonormal real basis functions, $F_{p,l,n}(\theta,\phi)$, are

$$F_{p,l,n}(\theta,\phi) = \check{\boldsymbol{\mathcal{H}}}^p_{l,n} \check{Y}_l(\theta,\phi) \;\text{ or }\; \hat{\boldsymbol{\mathcal{H}}}^p_{l,n} Y_l(\theta,\phi), \;\text{ for } n \in \{1,\ldots,N_{p;l}\} \tag{5.23}$$

which differ in whether real- or complex-valued spherical harmonics are used.

Note that the basis is not unique. In the approach of this paper, the nonuniqueness enters in several places, e.g., in the choice of A^p (Eq. 5.3), in the definition of the eigenvectors and the order of the loading of the eigenvectors into the matrix U (both Lemma 3), and in the creation of an orthonormal family of basis functions in the subspace of dimension $2l+1$ which is spanned by the $2l+1$ spherical harmonics of degree l.

5.5 Real basis functions generate and require real irreps

The one result in this section, Lemma 5, states that a real-valued set of orthonormal basis functions of the pth irrep of the finite group exists if and only if a real irrep exists, independent of whether the basis functions are expressed as linear combinations of spherical harmonics of fixed degree l.

Lemma 5. *Real-valued orthonormal basis functions of the pth irrep of the finite group G exist if and only if the pth irrep of G is potentially real.*

Proof. Real-valued functions imply real-valued irreps: Let $\boldsymbol{F}_{p,\zeta}(\mathbf{x}/x)$ for $\zeta \in \{1, \ldots, N_\zeta\}$ be a vector of d_p real-valued orthonormal basis functions where the jth component is the basis function that transforms according to the jth row of the pth irrep matrices of G. Therefore, Eq. 5.11 (the vector form of Eq. 5.7 in Definition 1) is

$$P(g)\boldsymbol{F}_{p,\zeta}(\mathbf{x}/x) = \boldsymbol{F}_{p,\zeta}(R_g^{-1}\mathbf{x}/x) = (\Gamma^p(g))^T \boldsymbol{F}_{p,\zeta}(\mathbf{x}/x). \tag{5.24}$$

Define $J^{p;p'}_{\zeta;\zeta'} \in \mathbb{R}^{d_p \times d_p}$ by

$$J^{p;p'}_{\zeta;\zeta'} = \int \left[P(g)\boldsymbol{F}_{p,\zeta}(\mathbf{x}/x)\right]\left[P(g)\boldsymbol{F}_{p',\zeta'}(\mathbf{x}/x)\right]^T \mathrm{d}\Omega. \tag{5.25}$$

Evaluate $J^{p;p'}_{\zeta;\zeta'}$ twice. In the first evaluation,

$$J^{p;p'}_{\zeta;\zeta'} = \int \boldsymbol{F}_{p,\zeta}(\mathbf{x}/x)\left[\boldsymbol{F}_{p',\zeta'}(\mathbf{x}/x)\right]^T \mathrm{d}\Omega = I_{d_p}\delta_{p,p'}\delta_{\zeta,\zeta'}, \tag{5.26}$$

where the first equality is due to rotation the coordinate system by R_g, and the second equality is due to the fact that the $\{F_{p,\zeta}\}$ are orthonormal.

In the second evaluation, use Eq. 5.24, rearrange, and use the orthonormality

of $\{F_{p,\zeta}\}$ to get

$$
\begin{aligned}
J^{p;p'}_{\zeta;\zeta'} &= \int (\Gamma^p(g))^T \boldsymbol{F}_{p,\zeta}(\mathbf{x}/x) \left[(\Gamma^{p'}(g))^T \boldsymbol{F}_{p';\zeta'}(\mathbf{x}/x)\right]^T \mathrm{d}\Omega && (5.27)\\
&= (\Gamma^p(g))^T \left[\int \boldsymbol{F}_{p,\zeta}(\mathbf{x}/x) \left[\boldsymbol{F}_{p',\zeta'}(\mathbf{x}/x)\right]^T \mathrm{d}\Omega\right] \Gamma^{p'}(g) && (5.28)\\
&= (\Gamma^p(g))^T \left[I_{d_p} \delta_{p,p'} \delta_{\zeta,\zeta'}\right] \Gamma^{p'}(g) && (5.29)\\
&= (\Gamma^p(g))^T \Gamma^{p'}(g) \delta_{p,p'} \delta_{\zeta,\zeta'}. && (5.30)
\end{aligned}
$$

Equating the two expressions for $J^{p;p'}_{\zeta;\zeta'}$ gives

$$(\Gamma^p(g))^T \Gamma^p(g) = I_{d_p}. \tag{5.31}$$

Since $\Gamma^p(g)$ is unitary, multiplying on the right by $(\Gamma^p(g))^H$ implies that $(\Gamma^p(g))^T = (\Gamma^p(g))^H$ so that $\Gamma^p(g)$ is real.

Real-valued irreps imply real-valued functions: This follows from Lemma 4 and Eqs. 5.22–5.23. □

5.6 Application to the rotational polyhedral groups

In this section, the theory of this paper is applied to the three rotational polyhedral groups, which are the tetrahedral T, octahedral O, and icosahedral I groups. Properties of each group and the parameter values which select a specific basis are described in Section 5.6.1 and the numerical results are presented in Section 5.6.2.

5.6.1 Irreps and rotation matrices of rotational polyhedral groups

Unitary complex-valued irrep matrices for the tetrahedral and octahedral groups are available at the Bilbao Crystallographic Server [9, 2, 1]. Unitary complex-valued irrep matrices for the icosahedral group are provided by [80]. The Frobenious-Schur indicator (Section 5.3) implies that all reps of the octahedral and the icosahedral groups are potentially real. Similarly, the tetrahedral group has irreps A and T that are potentially real and irreps ${}^1E$ and ${}^2E$ that are essentially complex. In the reminder of the paper, we refer to the tetrahedral irreps A, ${}^1E$, ${}^2E$ and T as the 1st, 2nd, 3rd and 4th irreps, respectively, and refer to the octahedral irreps A_1, A_2, E, T_1 and T_2 as the 1st, 2nd, 3rd, 4th and 5th irreps, respectively. The basic properties of the groups are tabulated in Table 5.1.

Symmetry Groups	N_g	N_{rep}	d_p	potentially real reps
Tetrahedral	12	4	$\{1, 1, 1, 3\}$	1,4
Octahedral	24	5	$\{1, 1, 2, 3, 3\}$	1,2,3,4,5
Icosahedral	60	5	$\{1, 3, 3, 4, 5\}$	1,2,3,4,5

Table 5.1: Basic properties of the rotational polyhedral groups: the group orders (N_g), the number of reps (N_{rep}), the dimension of the pth irrep (d_p for $p \in \{1, \ldots, N_{\text{rep}}\}$), and the potentially real reps of each group.

For each symmetry operation, a rotation matrix ($R_g \in \mathbb{R}^{3\times3}$ for $g \in G$ which satisfies $R_g^T = R_g^{-1}$, $\det R_g = +1$) is needed. The set of rotation matrices defines the relationship between the symmetries and the coordinate system. Any orthonormal real-valued irrep with $d_p = 3$ can serve as such a set of rotation matrices. For the tetrahedral and octahedral groups, rotation matrices are available at the Bil-

bao Crystallographic Server [9, 2, 1] although the matrices must be re-ordered in order to match the multiplication tables of the irrep matrices and, after re-ordering, they are the 4th irrep of the tetrahedral group and the 4th irrep of the octahedral group. For the icosahedral group, we desire to use the coordinate system in which the z-axis passes through two opposite vertices of the icosahedron and the xz plane includes one edge of the icosahedron [75, 5, 147]. Rotation matrices in this coordinate system are available [144] although the matrices must be reordered to match the multiplication table of the irrep matrices [80]. The reordering and the similarity matrix to match the rotation matrices to either of the two $d_p = 3$ sets of irrep matrices are given in Appendix A.2. The calculations described in this paper use the rotation matrices reordered to match the multiplication table of the 2nd irrep.

For the particular irreps described above, it is necessary to give values for the A^p matrices of Lemma 2. The identity matrix I_{d_p} satisfies the nonsingular and transpose symmetric hypotheses of Lemma 2. However, for the $p = 4$ irrep of the icosahedral group for which $d_4 = 4$, I_4 leads to $Z^4 = 0$ by direct computation. It was not difficult to find a choice for A^p such that all potentially-real irreps of the tetrahedral, octahedral, and icosahedral groups have nonzero Z^p. For instance, the choice of an "exchange permutation" matrix [50, Section 1.2.11, p. 20] for A^p, which is the anti-diagonal matrix with all ones on the anti-diagonal, leads to $Z^p = A^p$ by direct computation. This choice for A^p was used in all computations in this paper.

5.6.2 Numerical results

For the tetrahedral group, the coefficient matrices $\hat{\boldsymbol{\mathcal{H}}}^p_{l,n}$ for degree $l \in \{1, \ldots, 45\}$, $p \in \{1, 4\}$ and $n \in \{1, ..., N_{p;l}\}$, were computed. The total number of rows in the coefficient matrices is $N_{p=1;l} + N_{p=4;l} < 2l+1$ for each l, which is in agreement with the fact that only two of four irreps are potentially real and therefore only two of four irreps are included in our calculation. The resulting basis functions have been numerically verified to be real-valued and orthonormal.

For the octahedral and icosahedral cases, there are numerical checks that can be performed on the basis functions because all irreps are potentially real. Eq. 5.8 is achieved by construction. Eq. 5.9 is achieved by construction for $\hat{\mathcal{H}}^p_{l,m}$ and by testing an array of (θ, ϕ) values for $\check{\mathcal{H}}^p_{l,m}$. Eq. 5.10 is verified by forming the matrices $\check{\boldsymbol{\mathcal{H}}}_l = [(\check{\boldsymbol{\mathcal{H}}}^{p=1}_{l,1})^T, \ldots, (\check{\boldsymbol{\mathcal{H}}}^{p=N_{p;l}}_{l,N_{p;l}})^T, \ldots, (\check{\boldsymbol{\mathcal{H}}}^{p=N_{\text{rep}}}_{l,1})^T, \ldots, (\check{\boldsymbol{\mathcal{H}}}^{p=N_{\text{rep}}}_{l,N_{p;l}})^T]^T$ and $\hat{\boldsymbol{\mathcal{H}}}_l = [(\hat{\boldsymbol{\mathcal{H}}}^{p=1}_{l,1})^T, \ldots, (\hat{\boldsymbol{\mathcal{H}}}^{p=N_{p;l}}_{l,N_{p;l}})^T, \ldots, (\hat{\boldsymbol{\mathcal{H}}}^{p=N_{\text{rep}}}_{l,1})^T, \ldots, (\hat{\boldsymbol{\mathcal{H}}}^{p=N_{\text{rep}}}_{l,N_{p;l}})^T]^T$ and verifying that each is of dimension $(2l+1) \times (2l+1)$, which verifies that the correct number of basis functions have been found ($\sum_{p=1}^{N_{\text{rep}}} d_p N_l^p = 2l+1$), and verifying that $\check{\boldsymbol{\mathcal{H}}}_l$ ($\hat{\boldsymbol{\mathcal{H}}}_l$) is orthonormal (unitary) which verifies that the basis functions are orthonormal. Eq. 5.11 is verified by testing an array of (θ, ϕ) values. The verifications were carried out for $l \in \{0, \ldots, 45\}$.

Example basis functions are shown in Figure 6.2 by visualization of the function

$$\xi_{p,l,n,j}(\mathbf{x}) = \begin{cases} 1, & x \leq \kappa_1 + \kappa_2 F_{p,l,n,j}(\mathbf{x}/x) \\ 0, & \text{otherwise} \end{cases} \tag{5.32}$$

where κ_1 and κ_2 are chosen so that $0.5 \leq \kappa_1 + \kappa_2 I_{p,l,n,j}(\mathbf{x}/x) \leq 1$.

Please contact the corresponding author for software.

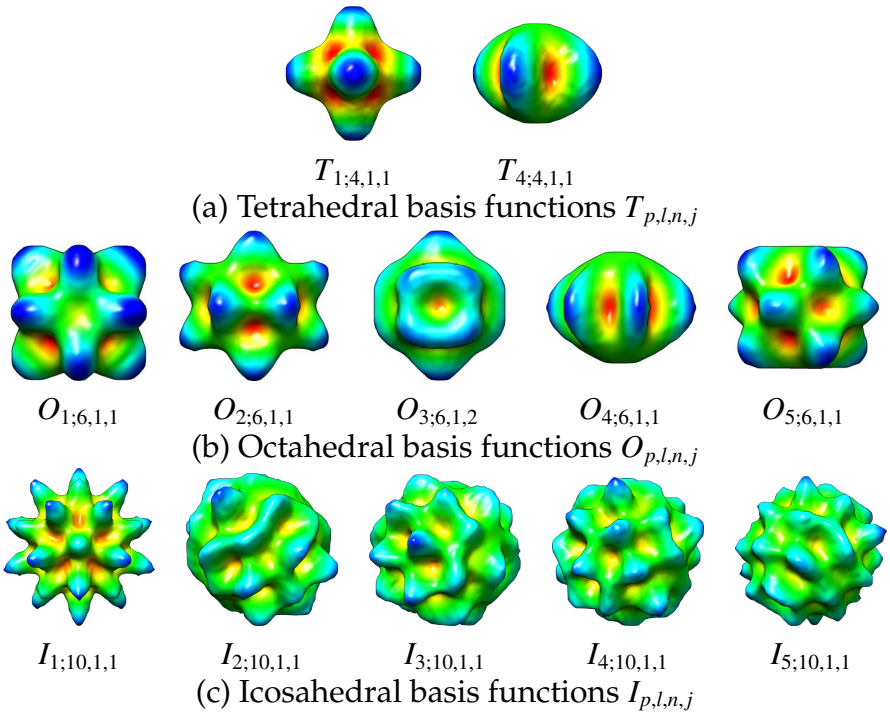

(a) Tetrahedral basis functions $T_{p,l,n,j}$

(b) Octahedral basis functions $O_{p,l,n,j}$

(c) Icosahedral basis functions $I_{p,l,n,j}$

Figure 5.1: Examples of the real basis functions of the three polyhedral groups. The surfaces of 3-D objects defined by Eq. 5.32 are visualized by UCSF Chimera [95] where the color indicates the distance from the center of the object.

5.7 Conclusion

Motivated by cryo electron microscopy problems in structural biology, this paper presents a method for computing real-valued basis functions which transform as the various rows and irreducible representations of a rotational polyhedral group. The method has two steps: (1) compute real-valued orthonormal irreducible representation matrices (Section 5.3) and (2) use the matrices to define projection operators which are applied to a real-valued basis for the desired function space (Section 5.4). The method is applied to the icosahedral, octahe-

dral, and tetrahedral groups where the second step is performed in spherical coordinates using the spherical harmonics basis. The most burdensome part of the calculation for the first step is the solution of a real symmetric eigenvector problem of dimension equal to twice the dimension of the irreducible representation matrices. For these three groups, the largest matrix is of dimension 5 so the calculations are straightforward. Of the remaining rotational polyhedral groups, basis functions for the cyclic groups are more naturally described in cylindrical coordinates using the complex exponential basis and possibly the same is true for the dihedral groups and so the calculations for the second step would be quite different from those described in this paper. However, the calculations in the first step, which apply to any potentially real irreducible representation, would remain relevant.

The resulting basis functions are described by linear combinations of spherical harmonics and a *Mathematica* program to compute the coefficients of the linear combination and a *Matlab* program to evaluate the resulting basis functions have been written and are available from the authors upon request.

CHAPTER 6

3D RECONSTRUCTION OF HETEROGENEOUS VIRUS PARTICLES WITH GEOMETRIC SYMMETRY ON STATISTICS

6.1 Introduction

In virology, discovering the structure of virus particles has been important. The virus particle has a shell of protein, called a "capsid", which surrounds a cavity containing the viral genome. Typical sizes and molecular weights of the virus particles are 10^2–10^3 Å and 10 MDa (10 megadaltons). The capsid is constructed of many repetitions of the same peptide molecule in geometric arrays. The geometry of these spherical viruses is important to their life cycles. Cryo electron microscopy (cryo EM), which has become an important technique for determining the geometry of a particle, leads to 3-D image reconstruction problems for these biological nano-machines Specifically, 10^3 – 10^6 virus particles are flash frozen to cryogenic temperatures and imaged. Each image is basically a highly-noisy (SNR < 0.1) 2-D projection of the 3-D electron scattering intensity distribution of the particle. Only one such image can be taken per particle and its projection orientation is unknown. Therefore, the information from many such images is fused to compute a 3-D reconstruction [66].

In the maturation process, the virus particles can be grouped into a number of discrete classes depending on their geometric forms, sizes, pH values, etc. In [133, 148], a reconstruction approach was presented, which includes both discrete classes and continuous variability of the particles within each class. The existing cryo electron microscopy are able to experimentalize an ensemble of virus particles within one class, which will be the objects to be discussed in the

remainder of this paper.

In cryo-electron microscopy, the 3-D structure of each virus particle is described by the 3-D electron scattering intensity function, denoted by $\rho(\cdot)$. The capsid of a virus particle has been well known to obey certain geometric symmetry [13]. The basic and the most popular assumption of the virus particles within one class [36, 142, 113, 77] is that each instance of the virus particle is identical and exactly obeys the rotational symmetry. In particular,

$$\rho(\mathbf{x}) = \rho_0(\mathbf{x}) \text{ with } \rho_0(\mathbf{x}) = \rho_0(M^{-1}\mathbf{x}), \tag{6.1}$$

where M is the rotational matrix and $\mathbf{x} \in \mathbb{R}^3$ are real-space coordinates. We call this assumption of "identical individuals". The reconstruction algorithm based on this rudimentary assumption is usually called the "homogeneous reconstruction with identical individuals" method (HRII). A sufficient assumption introduced in [133, 148] is that instances are different from each other (for example, due to the inherent flexibility of such a large molecular complex) but still each instance exactly obeys the rotational symmetry. In particular,

$$\rho(\mathbf{x}) = \rho(M^{-1}\mathbf{x}). \tag{6.2}$$

In the remainder of this paper, this assumption is referred as the assumption of "non-identical symmetrical individuals", and the reconstruction algorithm [133, 148] developed based on this assumption is named as the "heterogeneous reconstruction with symmetrical individuals" (HRSI).

In contrast to this previous work, this paper considers a more realistic and sophisticated view: The different instances of the particle are different and it is the *statistics* of the particle that obey the symmetry not the individual instances. In particular, the mean and covariance of the 3-D structure of the virus parti-

cle are invariant under the rotations. This idea is referred as the "symmetrical statistics".

$$\bar{\rho}(M^{-1}\mathbf{x}) = \bar{\rho}(\mathbf{x}) \text{ and } C_\rho(M^{-1}\mathbf{x}, M^{-1}\mathbf{x}') = C_\rho(\mathbf{x}, \mathbf{x}') \tag{6.3}$$

where $\bar{\rho}(\mathbf{x}) = \mathbf{E}[\rho(\mathbf{x})]$ and $C(\mathbf{x}, \mathbf{x}') = \mathbf{E}[\rho(\mathbf{x})\rho(\mathbf{x}')]$. We call the new reconstruction algorithm as "heterogeneous reconstruction with symmetrical statistics" (HRSS). Three possible structures described by each of the three assumptions are demonstrated through an example of four fold symmetry in Fig. 6.1.

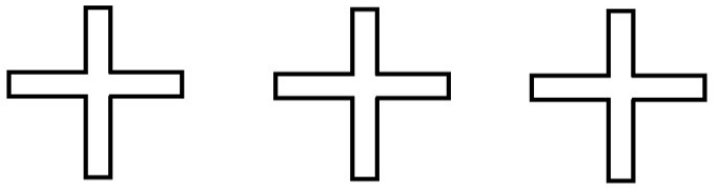

(a) Identical individuals (HRII)

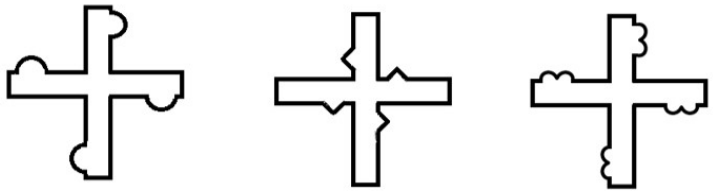

(b) Non-identical symmetrical individuals (HRSI)

(c) Symmetrical statistics (HRSS)

Figure 6.1: Four fold symmetry particles based on the three different assumptions and algorithms.

The largest class of plant and animal viruses is "spherical" viruses. The capsid of spherical virus particles most common is icosahedral symmetry–the symmetry group of an icosahedron–which is invariant under a total of 60 rotational

symmetry operations. In 3-D reality, the structure of a virus particle can be expressed as a linear combination of basis functions where the weights in the linear combination are Gaussian random variables [133, 148]. In particular,

$$\rho(\mathbf{x}) = \sum_{\zeta} F_{\zeta}(\mathbf{x}) c_{\zeta} \tag{6.4}$$

where $F_{\zeta}(\mathbf{x})$ is the basis function, c_{ζ} is the weight, and $\mathbf{x} \in \mathbb{R}^3$ are real-space coordinates. Because $\rho(\cdot)$ is real, it is convenient to have real-valued basis functions and weights.

To describe the situations of both "identical individuals" and "non-identical symmetrical individuals", the complete set of symmetric basis functions of the icosahedral group is sufficient. In the above rudimentary example of 2-D particles with four fold symmetry, these two situations (Fig. 6.1(a) and Fig. 6.1(b)) can be both described by the basis functions $e^{i4n\theta} h_l(r)$, where $h_l(r)$ is spherical Bessel functions for degree $l \in \mathbb{N}$. However, to describe the situation in which particles have asymmetric structures but symmetric statistics, a complete orthonormal set of real-valued basis functions with specific rotational properties under the operation of the icosahedral group is required (Section 6.2).

The maximum likelihood (ML) reconstruction algorithm can estimate the mean vector and covariance matrix of the vector of weights c_{ζ}, which is a generalization of classical ML Gaussian mixture parameter estimation [104]. After choosing appropriate basis functions, the estimates of the mean vector and covariance matrix need to be constrained in order to realize the two statistical symmetries as shown in Eq. 6.3 (Section 6.3). Taking the advantage of the existing reconstruction algorithms, the HRSS algorithm, introduced in this paper, can be developed by adding new basis functions and the additional constrains for the the mean vector and covariance matrix of the weights to the existing HRSI al-

gorithm (Section 6.4). The reconstruction results are demonstrated in constrast to the previous algorithms in Sections 6.5. As a result, HRSS eliminates the long-standing distortions in heterogeneity calculations associated with symmetry axes. The whole chapter is concluded in Section 6.6.

6.2 Real-valued basis functions

Each real-valued basis function $F_\zeta(\mathbf{x})$ is a product of an real-valued angular basis function and a real-valued radial basis function. The real-valued angular basis functions are complete orthonormal square integrable functions on the surface of the sphere, which includes the symmetry properties of the particle. In particular, they are the complete set of real-valued basis functions of the icosahedral group, which were derived and computed in Section 5.6 (Chapter 5) via generalized projection from group theory. Specifically, projection operators are applied to the real-valued spherical harmonics[1] [28, p. 93], which computes a basis function of the icosahedral group as a linear combination of spherical harmonics of a fixed degree l.

A key concept used in this approach is the irreducible representations (irreps) of a finite group, which are sets of 2-D square matrices that are homomorphic under matrix multiplication to the group elements. For the icosahedral group, it is possible to find all irreps matrices that are real-valued, which is required to generate the compete orthonormal basis functions that are real-valued (Chapter 5). Suppose that N_{rep} is the number of irreps of the N_g-order group G.

[1]Spherical harmonics are denoted by $Y_{l,m}(\theta,\phi)$ where the degree l satisfies $l \in \mathbb{N}$, the order m satisfies $m \in \{-l,\ldots,l\}$ and (θ,ϕ) are the angles of spherical coordinates with $0 \leq \theta \leq \pi$ and $0 \leq \phi \leq 2\pi$ [93, Section 14.30, pp. 378–379].

Let the set of real-valued matrices in the pth irrep be denoted by $\Gamma^p(g) \in \mathbb{R}^{d_p \times d_p}$ for all $g \in G$ where $p \in \{1, \ldots, N_{\text{rep}}\}$. For the icosahedral group, $N_{\text{rep}} = 5$, $N_g = 60$, and $d_p = 1, 3, 3, 4, 5$ for $p = 1, 2, 3, 4, 5$, respectively.

The resulting real-valued angular basis functions associated with the degree l and the pth irrep, denoted by $I_{p;l,n}(\mathbf{x}/x)$ for $n \in \{1, \ldots, N_{p;l}\}$, have the following properties.

1. Each $I_{p;l,n}$ is a d_p-dimensional real-valued vector function, i.e., $I_{p;l,n} \in \mathbb{R}^{d_p}$.
2. The $I_{p;l,n}$ functions are orthonormal on the surface of the sphere.
3. The subspace of square integrable functions on the surface of the sphere defined by spherical harmonics of index l, contains a set of $I_{p;l,n}$ functions with a total of $2l + 1$ components.
4. Each $I_{p;l,n}$ function has a specific transformation property under rotations from the icosahedral group [28, p. 20], in particular,

$$I_{p;l,n}(R_g^{-1}\mathbf{x}/x) = (\Gamma^p(g))^T I_{p;l,n}(\mathbf{x}/x) \tag{6.5}$$

   where ^{T} is transpose not Hermitian transpose and R_g is the 3×3 rotation matrix corresponding to the gth element of the group.

These properties were numerically verified from the close relationship between the $I_{p;l,n}$ and spherical harmonics. Furthermore, it follows that the family of $I_{p;l,n}$ is a complete basis for square integrable functions on the surface of the sphere. Examples of $I_{p,j;l,n}$ functions for $l = 15$ are visualized in Figure 6.2. Note that $p = 1$ exhibits all of the symmetries of an icosahedron. The angular basis functions used in the two previous algorithms, HRII and HRSI, are just the angular basis functions at $p = 1$.

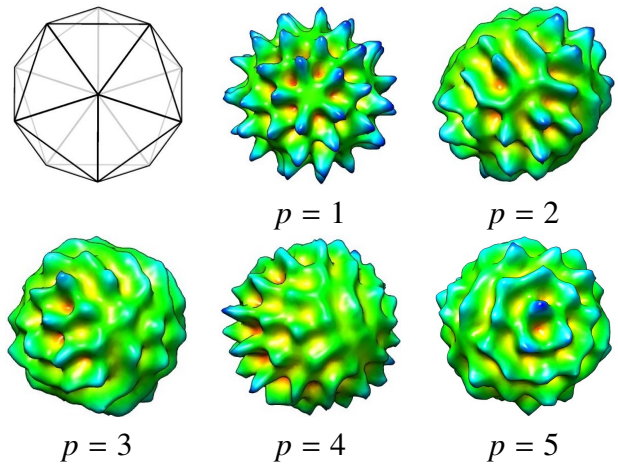

Figure 6.2: An icosahedron with one of each type of symmetry axis (2-, 3-, and 5-fold) shown and example angular basis functions with $l = 10$ and $p \in \{1, \dots N_{\text{rep}}\}$. The surfaces of 3-D objects defined by $\xi(\mathbf{x}) = 1$ for $x \leq \kappa_1 + \kappa_2 I_{p;l,n}(\mathbf{x}/x)$ and 0 otherwise, where κ_1 and κ_2 are chosen so that $\kappa_1 + \kappa_2 I_{p;l,n}(\mathbf{x}/x)$ varies between 0.5 and 1. are visualized by UCSF Chimera where the color indicates the distance from the center of the object.

The radial basis functions $h_{l,q}(x)$ for $q \in \{1, 2, \dots\}$ are exactly the family of Bessel functions used in [146, Section IIIB], which are real-valued and have the orthonormal condition, specifically,

$$\int_{r=0}^{\infty} h_{l,q}(x) h_{l,q'}(x) x^2 \mathrm{d}x = \delta_{q,q'}. \tag{6.6}$$

The reason that $h_{l,q}$ depends on l is that this makes it possible to have symbolic formulas for the 3-D Fourier transform of $\rho(\mathbf{x})$.

Let ζ be the shorthand for l, n, q, which has the total number that associates with the pth irrep of the icosahedral group to be $N_{p;\zeta}$, i.e., $\sum_{\zeta=1}^{N_{p;\zeta}} = \sum_{l=1}^{\infty} \sum_{n=1}^{N_{p;l}} \sum_{q=1}^{\infty}$. Each real-valued basis function, denoted by $F_{p;\zeta}(\mathbf{x})$, is the product of the nth angular basis function and the qth radial basis function that associate with the pth irrep of the icosahedral group and lth degree of spherical harmonics,

specifically, $F_{p;\zeta}(\mathbf{x}) = I_{p;l,n}(\mathbf{x}/x)h_{l,q}(x)$. The real-valued basis functions, $F_{p;\zeta}$ for $p \in \{1, \ldots, N_{\text{rep}}\}$ and $\zeta \in \{1, \ldots, N_{p;\zeta}\}$ have the following properties.

i) Each $F_{p;\zeta}$ is a d_p-dimensional real-valued vector function, i.e, $F_{p;\zeta} \in \mathbb{R}^{d_p}$.

ii) The $F_{p;\zeta}$ functions construct a complete orthonormal basis because of the orthonormality of $I_{p;l,n}$ and $h_{l,q}$, specifically,

$$\int_{\mathbf{x}} F_{p;\zeta}(\mathbf{x}) F^T_{p';\zeta'}(\mathbf{x}) \mathrm{d}\mathbf{x} = I_{d_p} \delta_{p,p'} \delta_{\zeta,\zeta'}. \tag{6.7}$$

(Please see Appendix A for the derivation.)

iii) Each $F_{p;\zeta}$ satisfies the following transformation because of Eq. 6.5, specifically, for all $g \in G$,

$$\begin{aligned} F_{p;\zeta}(R_g^{-1}\mathbf{x}) &= F_{p,l,n}(R_g^{-1}\mathbf{x}/x)h_{l,q}(x) \\ &= (\Gamma^p(g))^T F_{p,l,n}(\mathbf{x}/x)h_{l,q}(x) \\ &= (\Gamma^p(g))^T F_{p;\zeta}(\mathbf{x}). \end{aligned} \tag{6.8}$$

6.3 Constraints on weights caused by symmetrical statistics

The weight corresponding to the basis function $F_{p;\zeta}$, denoted by $c_{p;\zeta}$, is a real-valued vector, i.e., $c_{p;\zeta} \in \mathbb{R}^{d_p}$. Eq. 6.4 can be restated as

$$\rho(\mathbf{x}) = \sum_{p=1}^{N_{\text{rep}}} \sum_{\zeta=1}^{N_{p;\zeta}} F^T_{p;\zeta}(\mathbf{x}) c_{p;\zeta}. \tag{6.9}$$

The index τ in Eq. 6.4 is the shorthand of p and ζ, which has the total number N_τ to satisfy $N_\tau = \sum_{p=1}^{N_{\text{rep}}} N_{p;\zeta}$. The vector of weights $\mathbf{c} = [c_1^T, \ldots, c_{N_\tau}^T]^T = [c^T_{N_{p=1,\zeta}}, ..., c^T_{N_{p=1,\zeta}}, \ldots, c^T_{N_{p=N_{\text{rep}},1}}, ...c^T_{N_{p=N_{\text{rep}},\zeta}}]^T$ has Gaussian distribution $N(\bar{\mathbf{c}}, V)$, where $\bar{\mathbf{c}} = \mathbf{E}[\mathbf{c}] \in \mathbb{R}^{N_\tau \times 1}$ and $V = \mathbf{E}[\mathbf{c}\mathbf{c}^T] \in \mathbb{R}^{N_\tau \times N_\tau}$.

Our assumption of symmetrical statistics for the spherical virus particles is that the mean and the correlation function of the 3-D scattering intensity are invariant under all 60 rotations of the icosahedral group. These two conditions can be translated into the following two conditions, for all $g \in G$,

$$\bar{\rho}(R_g^{-1}\mathbf{x}) = \bar{\rho}(\mathbf{x}), \tag{6.10}$$

$$C_\rho(R_g^{-1}\mathbf{x}, R_g^{-1}\mathbf{x}') = C_\rho(\mathbf{x}, \mathbf{x}'), \tag{6.11}$$

where $\bar{\rho}(\mathbf{x}) = \mathbf{E}[\rho(\mathbf{x})]$, $C(\mathbf{x}, \mathbf{x}') = \mathbf{E}[\rho(\mathbf{x})\rho(\mathbf{x}')]$ and R_g is the gth rotation matrix in group G. These two conditions induce constraints on the weights of basis functions, in particular, the mean vector $\bar{\mathbf{c}}$ and covariance matrix V.

6.3.1 Constraint caused by the first order statistics

The symmetry on the first order statistics (Eq. 6.10) induces a constraint on the mean of the weights. By definition (Eq. 6.9) and the transformation property (Eq. 6.8), the RHS of Eq. 6.10 can be expanded as

$$\begin{aligned} \bar{\rho}(\mathbf{x}) &= \mathbb{E}\left[\sum_p \sum_\zeta F_{p;\zeta}^T(\mathbf{x}) c_{p;\zeta}\right] \\ &= \sum_p \sum_\zeta F_{p;\zeta}^T(\mathbf{x}) \mathbb{E}\left[c_{p;\zeta}\right] \end{aligned} \tag{6.12}$$

and the LHS of Eq. 6.10 becomes

$$\begin{aligned} \bar{\rho}(R_g^{-1}\mathbf{x}) &= \sum_p \sum_\zeta F_{p;\zeta}^T(R_g^{-1}\mathbf{x}) \mathbb{E}\left[c_{p;\zeta}\right] \\ &= \sum_p \sum_\zeta \left(\Gamma^p(g)^T F_{p;\zeta}(\mathbf{x})\right)^T \mathbb{E}\left[c_{p;\zeta}\right] \\ &= \sum_p \sum_\zeta F_{p;\zeta}^T(\mathbf{x}) \Gamma_c^p(g) \mathbb{E}\left[c_{p;\zeta}\right], \end{aligned} \tag{6.13}$$

Equating Eq. 6.13 and Eq. 6.12 to give

$$\sum_{p}\sum_{\zeta} F^{T}_{p;\zeta}(\mathbf{x})(\Gamma^{p}_{c}(g) - I_d)\mathbb{E}\left[c_{p;\zeta}\right] = 0, \tag{6.14}$$

which holds for all $g \in G$. Because only the $\Gamma^{p=1}_{c}(g) = 1$ for all $g \in G$ and $\Gamma^{p\neq 1}_{c}(g)$ for all $g \in G$ are real-valued full matrices, the mean of $c_{p;\zeta}$, needs to satisfy

$$\mathbb{E}\left[c_{p;\zeta}\right] = \mathbb{E}\left[c_{p;\zeta}\right]\delta_{p,1}. \tag{6.15}$$

In other words, the entries of $\bar{\mathbf{c}}$ that corresponding to the pth ($p \neq 1$) irrep are constrained to be zero.

6.3.2 Constraint caused by the second order statistics

The symmetry condition on the second order statistics (Eq. 6.11) can be achieved by constraints on the covariance matrix of the weights.

Similar to the derivation of Eq. 6.12-6.13, the RHS of Eq. 6.11 can be expressed as

$$\begin{aligned} &C_{\rho}(\mathbf{x},\mathbf{x}') \\ &= \mathbb{E}\left[\left(\sum_{p}\sum_{\zeta} F^{T}_{p;\zeta}(\mathbf{x})c_{p;\zeta}\right)\left(\sum_{p'}\sum_{\zeta'} F^{T}_{p';\zeta'}(\mathbf{x}')c_{p';\zeta'}\right)^{T}\right] \\ &= \sum_{p}\sum_{\zeta}\sum_{p'}\sum_{\zeta'} F^{T}_{p;\zeta}(\mathbf{x})\mathbb{E}\left[c_{p;\zeta}c^{T}_{p\,\zeta'}\right]F_{p';\zeta'}(\mathbf{x}'), \end{aligned} \tag{6.16}$$

and the LHS of Eq. 6.11 can be expressed as

$$
\begin{aligned}
& C_\rho(R_g^{-1}\mathbf{x}, R_g^{-1}\mathbf{x}') \\
&= \sum_p \sum_\zeta \sum_{p'} \sum_{\zeta'} F_{p;\zeta}(R_g^{-1}\mathbf{x}) \mathbb{E}\left[c_{p;\zeta} c_{p';\zeta'}^T\right] F_{p';\zeta'}(R_g^{-1}\mathbf{x}) \\
&= \sum_p \sum_\zeta \sum_{p'} \sum_{\zeta'} \left((\Gamma_g^p(g))^T F_{p;\zeta}(\mathbf{x})\right)^T \mathbb{E}\left[c_{p;\zeta} c_{p';\zeta'}^T\right] \left((\Gamma_g^{p'}(g))^T F_{p';\zeta'}(\mathbf{x}')\right) \\
&= \sum_p \sum_\zeta \sum_{p'} \sum_{\zeta'} F_{p;\zeta}^T(\mathbf{x}) \Gamma_g^p(g) \mathbb{E}\left[c_{p;\zeta} c_{p';\zeta'}^T\right] (\Gamma_g^{p'}(g))^T F_{p';\zeta'}(\mathbf{x}')
\end{aligned}
\tag{6.17}
$$

On both sides of the symmetry condition (Eq. 6.11), multiply on the left by $F_{p;\zeta}(\mathbf{x})$ and on the right by $F_{p';\zeta'}^T(\mathbf{x}')$ for random (p, ζ) and (p', ζ'), and integrate over the 3D coordinates $\mathbf{x}$ and $\mathbf{x}'$. Specifically,

$$
\begin{aligned}
& \int_{\mathbf{x}} \int_{\mathbf{x}'} F_{p;\zeta}(\mathbf{x}) C_\rho(\mathbf{x}, \mathbf{x}') F_{p';\zeta'}(\mathbf{x}') \mathrm{d}\mathbf{x}\mathrm{d}\mathbf{x}' \\
&= \int_{\mathbf{x}} \int_{\mathbf{x}'} F_{p;\zeta}(\mathbf{x}) C_\rho(R_g^{-1}\mathbf{x}, R_g^{-1}\mathbf{x}') F_{p';\zeta'}(\mathbf{x}') \mathrm{d}\mathbf{x}\mathrm{d}\mathbf{x}'.
\end{aligned}
\tag{6.18}
$$

Because the basis functions are orthonormal on the 3D space (Eq. 6.7), by inserting Eq. 6.16 and 6.17 into Eq. 6.18, it gives $\mathbb{E}\left[c_{p;\zeta} c_{p';\zeta'}^T\right] = \Gamma^p(g)^T \mathbb{E}\left[c_{p;\zeta} c_{p';\zeta'}^T\right] \Gamma^{p'}(g)$ for all $g \in G$. Therefore, since the irred rep is orthogonal ($\Gamma^p(g)^{-1} = \Gamma^p(g)^T$), it follows that

$$
\Gamma^p(g) \mathbb{E}\left[c_{p;\zeta} c_{p';\zeta'}^T\right] = \mathbb{E}\left[c_{p;\zeta} c_{p';\zeta'}^T\right] \Gamma^{p'}(g) \tag{6.19}
$$

for all $g \in G, \mathbf{x}, \mathbf{x}' \in \mathbb{R}^{3\times 3}$, $p, p' \in \{1, \ldots, N_{\text{rep}}\}$, $\zeta \in \{1, \ldots, N_{p;\zeta}\}$, and $\zeta' \in \{1, \ldots, N_{p';\zeta'}\}$. Since $\Gamma^p(g) \in \mathbb{R}^{d_p \times d_p}$ and $\Gamma^{p'}(g) \in \mathbb{R}^{d_{p'} \times d_{p'}}$ $\mathbb{E}[c_{p,\zeta} c_{p',\zeta'}^T]$ is a $d_p \times d_{p'}$ matrix. Eq. 6.19 has substantial structure because $\Gamma^p(g)$ and $\Gamma^{p'}(g)$ both for all $g \in G$ are irrep matrices. Schur's Lemma [28, Theorem I and II, Section 4.5, p. 80] implies that

$$
\mathbb{E}[c_{p,\zeta} c_{p',\zeta'}^T] = \begin{cases} v_p((\zeta, \zeta') I_{d_p}, & p = p' \\ \mathbf{0}_{d_p, d_{p'}}, & \text{otherwise} \end{cases} \tag{6.20}
$$

for some number $v_p((\zeta, \zeta')$ depending on p, ζ and ζ', where $\mathbf{0}_{i,j}$ is the $i \times j$ zero matrix. Note that the solution of Eq. 6.19 for $\mathbb{E}[c_{p,\zeta} c_{p',\zeta'}^T]$ does not depend on ζ

and ζ' except that unspecified degrees of freedom in the solution could depend on ζ and ζ'.

Suppose that the indices vary from the slowest to the fastest in the order p, ζ, or more specifically, in the order p, l, n, and q. Then p is constant over sequential sets of $d_p N_{p;\zeta}$ rows and columns in covariance matrix V. The matrix $\mathbb{E}[c_{p,\zeta} c_{p',\zeta'}^T]$ constructs the $(p, p')^{th}$ block of the covariance matrix V, denoted by $V_{p:p'}$. Precisely, $\mathbb{E}[c_{p,\zeta} c_{p',\zeta'}^T]$ is the (ζ, ζ')th sub-block of the matrix $V_{p:p'}$. Therefore, implied by Eq. 6.20, the covariance matrix V is a diagonal block matrix with five blocks, corresponding to the five values of p, and off diagonal blocks are zeros, i.e., $V_{p:p' \neq p} = \mathbf{0}_{(d_p N_{p;\zeta}),(d_{p'} N_{p';\zeta'})}$. The pth block itself ($V_{p:p}$) is a Kronecker product of the identity matrix I_{d_p} and a $N_{p;\zeta} \times N_{p;\zeta}$ matrix V_p, which has the (ζ, ζ')th ($\zeta, \zeta' \in \{1, \ldots, N_{p;\zeta}\}$) entry to be $v_p(\zeta, \zeta')$. More explicitly,

$$
\begin{aligned}
& V_{p:p} \\
& = V_p \otimes I_{d_p} \\
& = \begin{bmatrix} v_p(1,1) & v_p(1,2) & \ldots & v_p(1, N_{p;\zeta}) \\ v_p(2,1) & v_p(2,2) & \ldots & v_p(2, N_{p;\zeta}) \\ \vdots & \vdots & \ddots & \vdots \\ v_p(N_{p;\zeta}, 1) & v_p(N_{p;\zeta}, 2) & \ldots & v_p(N_{p;\zeta}, N_{p;\zeta}) \end{bmatrix} \otimes I_{d_p} \\
& = \begin{bmatrix} v_p(1,1) I_{d_p} & v_p(1,2) I_{d_p} & \ldots & v_p(1, N_{p;\zeta}) I_{d_p} \\ v_p(2,1) I_{d_p} & v_p(2,2) I_{d_p} & \ldots & v_p(2, N_{p;\zeta}) I_{d_p} \\ \vdots & \vdots & \ddots & \vdots \\ v_p(N_{p;\zeta}, 1) I_{d_p} & v_p(N_{p;\zeta}, 2) I_{d_p} & \ldots & v_p(N_{p;\zeta}, N_{p;\zeta}) I_{d_p} \end{bmatrix}.
\end{aligned}
\tag{6.21}
$$

The covariance matrix V constructed from all of the $V_{p:p}$ blocks must be a real-valued positive semidefinite matrix, which requires each of the blocks is a real-valued positive semidefinite matrix. In order to make Eq. 6.21 be real-

valued and positive semidefinite, it is necessary that $v_p(\zeta, \zeta') \in \mathbb{R}^+ \cup \{0\}$ for all $\zeta, \zeta' \in \{1, \ldots, N_{\text{rep}}\}$ and $p \in \{1, \ldots, N_{\text{rep}}\}$.

6.4 Heterogeneous reconstruction with symmetrical statistics (HRSS)

The 3D reconstruction process of heterogeneous virus particles which realize the symmetrical statistics is described in this section. In particular, the first two order statistics of the weights $\bar{\mathbf{c}}$ and V are solved by a constrained maximum likelihood estimator.

Suppose that a image stack includes N_y numbers of 2D projection images. Through the projection slice theorem, the model for the 3D structure of the virus particle (Eq. 6.4) can be linearly transformed into a model for the 2D projection images, specifically [148],

$$\mathbf{y}_i = L(z_i)\mathbf{c}_i + \mathbf{w}_i, \mathbf{w}_i \sim N(0, Q) \tag{6.22}$$

where $\mathbf{y}_i$ is the ith 2D projection image in the reciprocal space, z_i is a vector of nuisance parameters which include the projection orientation of the ith image and the projection location of the particle in the ith image, $\mathbf{c}_i \in \mathbb{R}^{N_\tau}$ is the vector of weights of the ith image[2], $L(z_i)$ is the transformation matrix from weights to the ith reciprocal-space image which is transformed from the real-valued basis functions by projection slice theorem, and $\mathbf{w}_i$ is the white Gaussian noise of the ith image which has zero mean and a covariance Q. Based on our assumption, the vector of weights is Gaussian distributed, specifically, $\mathbf{c}_i \sim N(\bar{\mathbf{c}}, V)$, where $\bar{\mathbf{c}}$ and V are the parameters to be determined.

[2]The weights $\mathbf{c}_i$ in Eq. 6.22 are identical to the weights in the 3D model (Eq. 6.4).

We use a maximum likelihood estimator, as is described in [148], to determine $\bar{\mathbf{c}}$ and V. The maximum likelihood estimator is computed by an expectation-maximization algorithm with the nuisance parameters $\{z_i\}_{i=1}^{N_y}$. Three quantities are updated, the *a priori* distribution of the ensemble of virus particle, the mean $\bar{\mathbf{c}}$ and the covariance V of the weights. In our problem, the two quantities, $\bar{\mathbf{c}}$ and V, are updated alternatively in the expectation-maximization algorithm.

The previous algorithm HRSI [133, 124], which only used a subset of the proposed angular basis functions (just $p = 1$), used Matlab's `fmincon` (option "trust-region-reflective") with symbolic cost, gradient of the cost, and Hessian of the cost. We desired to modify the software to include the full set of basis functions described in Section 6.2. The constraint on the mean vector (Eq. 6.15) requires its entries to be zero if $p \neq 1$. Let the V matrix to be a diagonal matrix. The constraints on the covariance matrix V (Eq. 6.21) require certain matrix elements to be equal. To implement the above constraints, the method of computing the gradient and Hessian of the cost is modified based on the chain rule: if f is the cost then

$$\frac{\partial f}{\partial \zeta_{p;l,n,q}} = \sum_{j=1}^{d_p} \frac{\partial f}{\partial \nu_{p,j;l,n,q}},$$

$$\frac{\partial^2 f}{\partial \zeta_{p_1;l_1,n_1,q_1} \partial \zeta_{p_2;l_2,n_2,q_2}} = \sum_{j_1=1}^{d_{p_1}} \sum_{j_2=1}^{d_{p_2}} \frac{\partial^2 f}{\partial \nu_{p_1,j_1;l_1,n_1,q_1} \partial \nu_{p_2,j_2;l_2,n_2,q_2}}.$$

These equations compute the necessary gradient and Hessian in terms of larger vectors and matrices which are then reduced in size. While this approach fits the software easily, more efficient approaches may be possible.

In comparison to the two existing algorithms (HRII [148] and HRSI [133, 148]), the new algorithm HRSS strictly generalizes both HRII and HRSI since (1)

HRII uses only the $p = 1$ angular basis functions and has no constraints on the mean vector of the weights but has the covariance matrix to be zero, i.e., $V = 0$, and (2) HRSI uses only the $p = 1$ angular basis functions and has no constraints on the mean vector or covariance matrix of the weights, and (3) HRSS uses all $p \in \{1, 2, 3, 4, 5\}$ angular basis functions and has the constraint of Eq. 6.15 on the mean vector and the constraint of Eq. 6.21 on the covariance matrix. In other words, HRSS strictly contains both HRII and HRSI as special cases. In terms of computation, all three algorithms estimate the same number of parameters for the mean vector $\bar{\mathbf{c}}$. Only HRSI and HRSS estimate the parameters for the covariance matrix V. Because the number of parameters to be estimated for V corresponds to the number of basis functions to be used, HRSS needs to estimate much more parameters than HRSI does to compute V.

6.5 Reconstruction Results

The performance of the proposed algorithm, HRSS, is evaluated in this section. The reconstruction process has been performed both on a simulated data (Section 6.5.2) and on the experimental data of a Virus Like Particle (VLP) derived from bacteriophage HK97 Prohead I^{+pro} (Section 6.5.3). The VLP is essentially the bacteriophage minus the bacteriophage's tail leaving only the icosahedrally symmetric capsid. The average outer radius of the capsid is 254 Å.

6.5.1 Data processing

Two sets of 1200 cryo-EM images were separately processed. Each image containing one bacteriophage HK97 Prohead I^{+pro} particle, was randomly selected from a larger stack. Each 2-D cryo-EM image measuring 200×200 pixels with a pixel size of 2.76Å. Due to limitations of our computer hardware (computational speed and memory size), it is not practical to process the entire stack. The image selection algorithm [133] guarantees on non-overlapping sets of images. For each data set, following the preprocessing procedure in [133, 148], the 1200 cryo-EM images were transformed into 1200 2-D images in real and reciprocal space, and the reciprocal space images are the input to reconstruction algorithms.

The reconstruction is achieved in the following two steps.

(a) The mean vector of the weights, denoted by $\bar{\mathbf{c}}_0$, is first computed by the *homogeneous reconstruction* algorithm (HRII) described in [148] which has $V_0 = 0$.

(b) These results $\bar{\mathbf{c}}_0$ and V_0 are used as the initial condition for the *heterogeneous reconstruction* (HRSI or HRSS) in the second step to compute the final results for $\bar{\mathbf{c}}$ and V.

Both HRSI and HRSS are tested. When testing on the existing heterogeneous reconstruction model (HRSI), due to the computing limitation, basis functions with l up to 55 and q up to 20 were employed in both Step (a) (HRII) and Step (b) (HRSI). The number of parameters to be estimated in Step (b) for either $\bar{\mathbf{c}}$ or V is 1060. When testing on the proposed heterogeneous reconstruction model

(HRSS) which use the complete basis functions, we aim to achieve a similar scale of parameters to be estimated. Basis functions with l up to 10 and q up to 20 were employed in both Step (a) (HRII) and Step (b) (HRSS). The number of parameters to be estimated in Step (b) for $\bar{\mathbf{c}}$ or V is 2020.

6.5.2 Performances on the simulated data

The simulated 2D projection images in reciprocal space are generated through the same reconstruction forward model (Eq.6.22). The input of the simulator is the HRSS reconstruction results $\bar{c}$ and V, which are called the "ground truth" in the stimulation study. The parameters to be determined ahead of the simulation process include the resolution (e.g., the pixel size in Å and the total number of pixels) and the signal-to-noise ratio (SNR) of the image. The method of generating the simulated 2D images is described in Algorithm 1. Let the image have

---

Data: The HRSS results $\bar{\mathbf{c}}$ and V
Result: a stack of 2D projection simulated images $\{y_i\}_{i=1}^N$

for $i = 1; i <= N; i++$ **do**
  1. generate $\mathbf{c}_i \sim N(\bar{\mathbf{c}}, V)$ and pick z_i
  2. compute the 2D image:
    (reciprocal space) $\mathbf{y}_i = L(z_i)\mathbf{c}_i$
    (real space) $\mathbf{y}_i \rightarrow Real(\mathbf{y}_i)$ [148]
  3. construct the white noise:
    compute sample variances of $Real(\mathbf{y}_i)$, denoted by s^2
    generate $w_i \sim N(0, Q)$, where $Q = \frac{s^2}{SNR} I$
  4. generate simulated images (Eq.6.22):
    (reciprocal space)$\mathbf{y}_i = L(z_i)\mathbf{c}_i + w_i$
    (real space) $\mathbf{y}_i \rightarrow Real(\mathbf{y}_i)$ [148]
end

Algorithm 1: Generation of N simulated 2D images.

100×100 pixels with a pixel size of 5.52 Å and let $SNR = 0.5$. A stack of 1200

simulated 2D projection images of HK97 is generated. Examples of the simulated real space 2D images of HK97 are shown in Fig. 6.3. With this input, the two-step reconstruction with the use of HRSS is performed. By using the same parameter settings in the reconstruction with the experimental images as the input, basis functions with l up to 10 and q up to 20 were employed in both Step (a) (HRII) and Step (b) (HRSS).

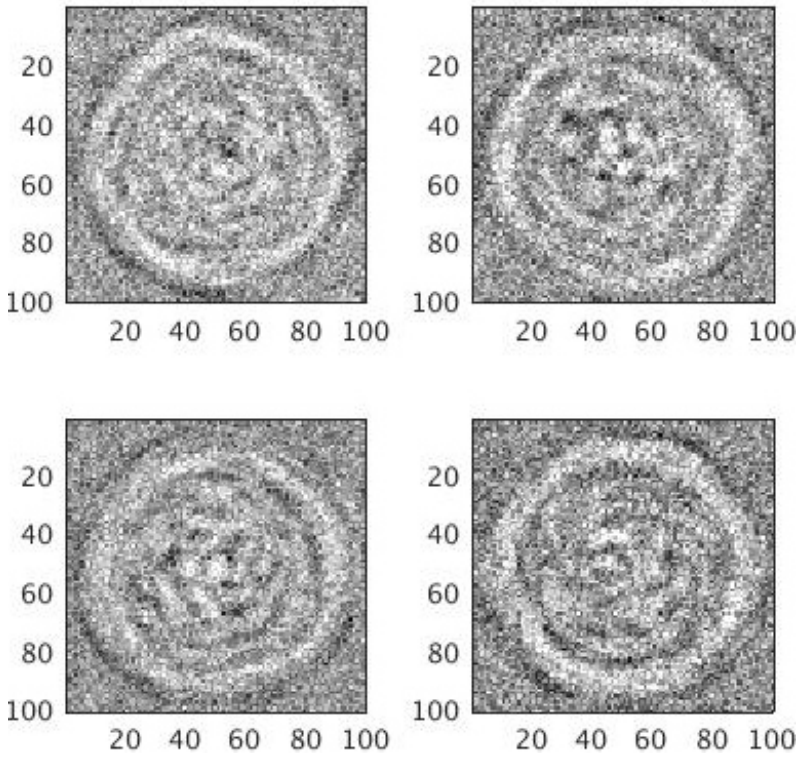

Figure 6.3: Four simulated real space 2D images of HK97.

The standard measure of performance in structural biology is the Fourier shell correlation (FSC) ([129], Eq. 2; [55], Eq. 17; [12], p. 879) between two structures (the two estimates of mean electron scattering intensity) computed from the disjoint stacks of images. The final reconstruction ($\bar{\mathbf{c}}$ and V) is compared with the "ground truth". Their FSC curve and energy curve (the denominators of FSC calculation) are shown in Fig. 6.4. The results show that the Fourier Shell

Correlation (FSC) between the reconstruction result and the "ground truth" are almost 1 for more than the range $k \leq 0.186\text{Å}^{-1}$ and therefore the structures are essentially identical for more than the range $k \leq 0.186\text{Å}^{-1}$. The energy in both structures drops around 5 at 0.186Å^{-1}, which is greater than 0. Therefore, the FSC analysis in the range $k \leq 0.186\text{Å}^{-1}$ is meaningful.

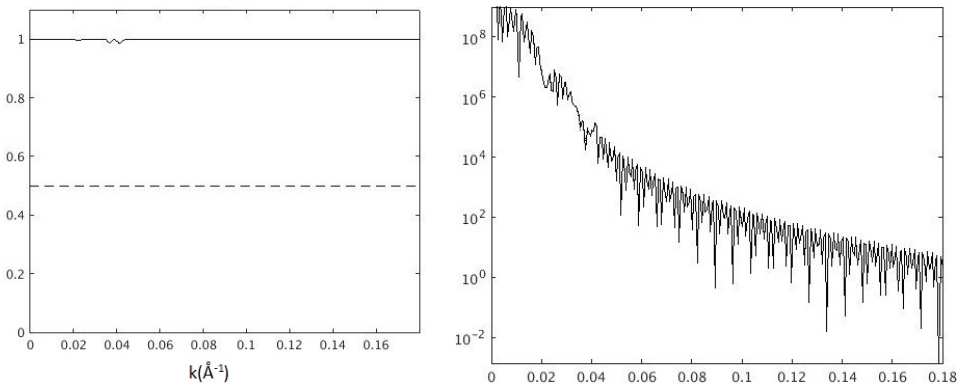

(a) FSC curve (b) Energy curve

Figure 6.4: FSC and energy curves between the "ground truth" and the reconstruction results of the simulated data.

6.5.3 Performances on the experimental data

From the mean vector $\bar{\mathbf{c}}$ and the covariance matrix V, it is possible to compute the mean function [148, Eq. 16], $\bar{\rho}(\mathbf{x}) = E[\rho(\mathbf{x})]$, and covariance function [148, Eq. 18], $C_\rho(\mathbf{x}_1, \mathbf{x}_2) = E[(\rho(\mathbf{x}_1) - \bar{\rho}(\mathbf{x}_1))(\rho(\mathbf{x}_2) - \bar{\rho}(\mathbf{x}_2))]$, of the electron scattering intensity $\rho(\mathbf{x})$ of the particle. We often visualize $s_\rho(\mathbf{x}) = \sqrt{C_\rho(\mathbf{x}, \mathbf{x})}$ which has the same units as $\bar{\rho}(\mathbf{x})$. Through Eq. 6.9, the mean vectors $\bar{\mathbf{c}}$ computed by HRSI and HRSS in Step (b) were used to compute two mean functions $\bar{\rho}(\mathbf{x})$. Similarly, the two covariance matrices V computed by HRSI and HRSS were used to compute two standard deviation functions $s_\rho(\mathbf{x})$. We computed FSC between the reconstructions of the two data sets for both HRSI and HRSS, which are shown in

Fig. 6.5. In the case of HRSI (Fig. 6.5 (a)), the resolution is determined by the fact that the FSC curve crosses the 0.5 level at 0.061 $Å^{-1}$, which gives a resolution of 16.442 Å. In the case of HRSS (Fig. 6.5 (b)), the FSC between the two reconstructions are almost 1 for more than the range $k \leq 0.186Å$ and therefore the structures are essentially identical.

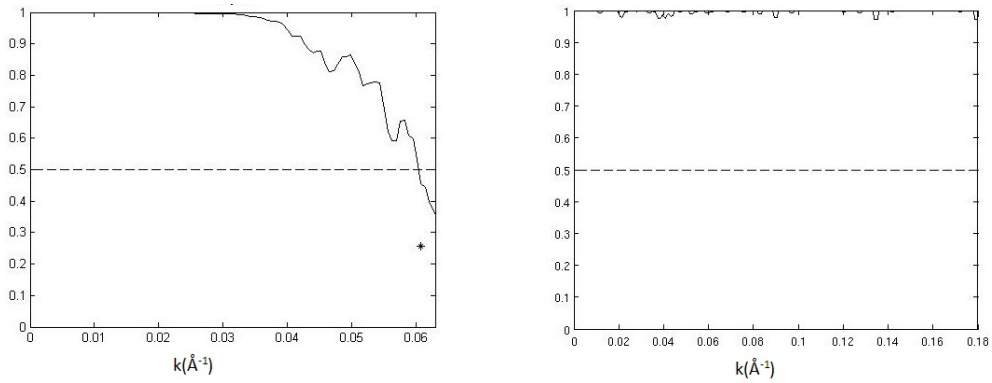

(a) symmetrical individuals (HRSI) (b) symmetrical statistics (HRSS)

Figure 6.5: FSC curves between the reconstructions of the two experimental data sets for HRSI (a) and HRSS (b).

Fig. 6.6 (b) and (c) show the standard deviation $s_\rho(\mathbf{x})$ computed by HRSI and HRSS, respectively. In Fig. 6.7, $\bar{\rho}(\mathbf{x})$ computed by HRSI and the two heterogeneous solutions $s_\rho(\mathbf{x})$ computed by HRSI and HRSS are jointly visualized by computing a 3-D surface of constant value of $\bar{\rho}(\mathbf{x})$ and coloring the surface by $s_\rho(\mathbf{x})$. The cubes of $\bar{\rho}$ and s_ρ in Fig. 6.6–6.7 have the same orientation as shown in Fig. 6.6 (a), in which the x-z plane contains the two fold symmetry of the icosahedron. We call Fig. 6.6 (a) as the two fold axes.

Fig. 6.8 shows six different cross sections of the standard deviation function $s_\rho(\mathbf{x})$ in three different axes the two fold, the three fold and the five fold symmetry axes. The two fold symmetry, the three fold symmetry and the five fold

symmetry of the icosahedron are sitting along the Z axis, as shown in the top row of Fig. 6.8, where the center of the s_ρ cube has the coordinate (300, 300, 300).

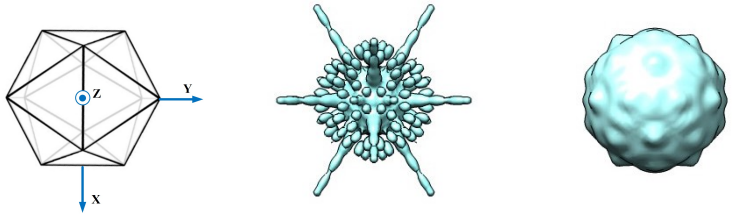

(a) two fold symmetry axes (b) symmetrical individuals (HRSI) (c) symmetrical statistics (HRSS)

Figure 6.6: 3-D reconstructions of the standard deviation s_ρ for HK97 Prohead I^{Pro+}. The shape is a surface of constant intensity (0.0038) of the standard deviation $s_\rho(\mathbf{x})$, which is visualized by UCSF Chimera [95].

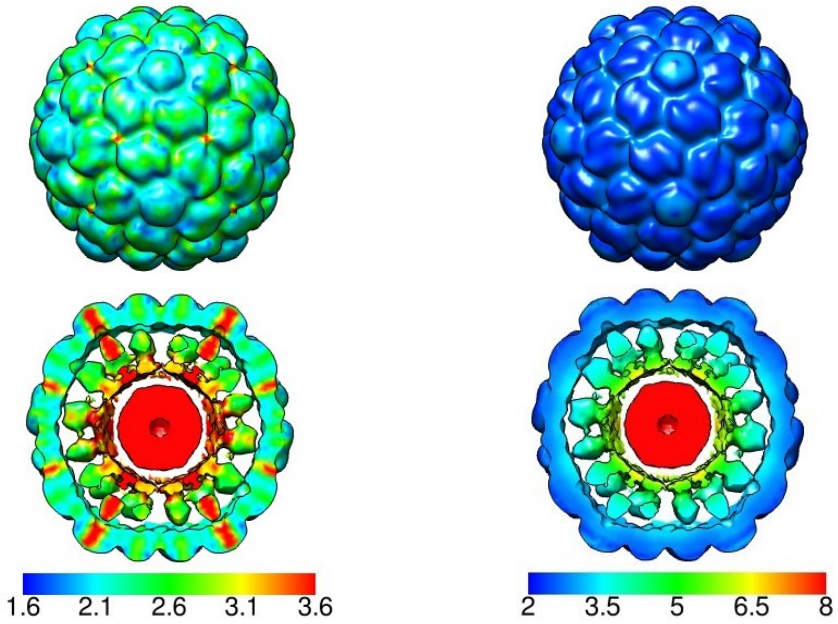

(a) symmetrical individuals (HRSI) (b) symmetrical statistics (HRSS)

Figure 6.7: 3-D reconstructions of $\bar{\rho}$ for HK97 Prohead I^{+pro} (different colormap). The shape is a surface of constant intensity (5×10^{-4}) of $\bar{\rho}(\mathbf{x})$ colored by the standard deviation $s_\rho(\mathbf{x})$, which is visualized by UCSF Chimera [95]. The HRSI and HRSS reconstructions use different color maps. All markings are scaled by 10^{-3}.

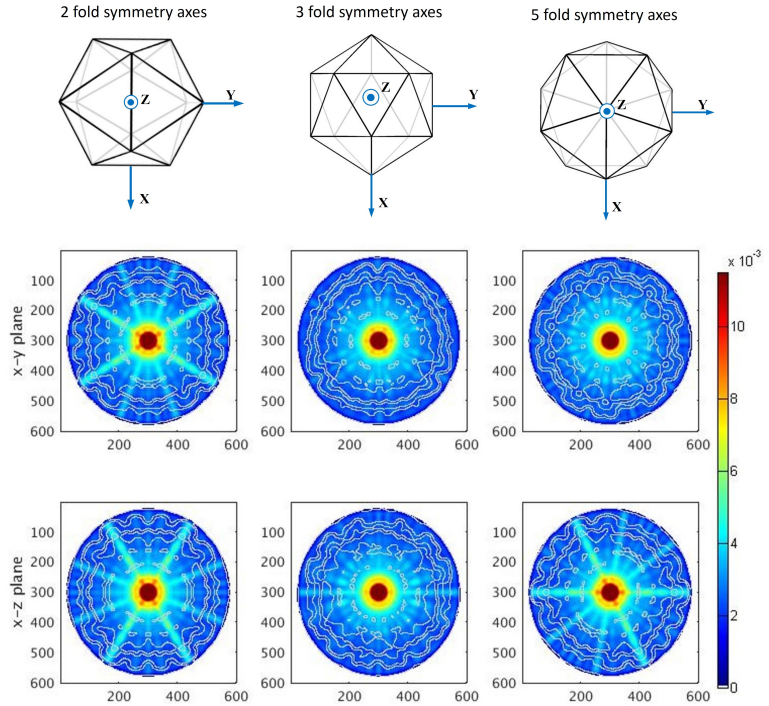

(a) symmetrical individuals (HRSI)

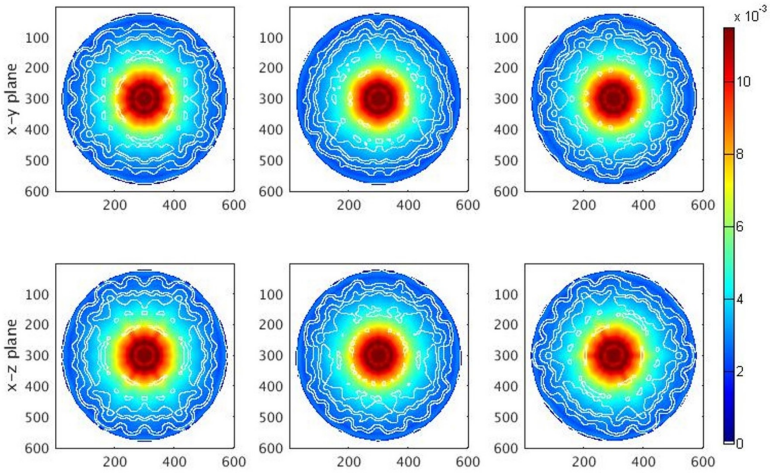

(b) symmetrical statistics (HRSS)

Figure 6.8: Cross section of the standard deviation function $s_\rho(\mathbf{x})$ for HK97 Prohead I^{+pro} using both HRSI and HRSS and displayed with a common color map. The white lines depict the contour levels of the virus particles. The geometrical orientation of the cubes are shown in the top row. (a) shows the reconstruction results based on symmetrical individuals, i.e., HRSI, whereas (b) shows the reconstruction results based on symmetrical statistics, i.e., HRSS. For each orientation, cross sections in x-y and x-z planes are displayed. The center of the s_ρ cube has the coordinate (300, 300, 300).

As shown in Fig. 6.6 (b) and Fig. 6.7 (a), the existing algorithm HRSI estimates a standard deviation function that is organized in radially-directed rays, which has no biological explanation. Specifically, HRSI introduced artifical spikes laying on the symmetry axes of the icosahedron. In fact, this artificial pattern in standard deviation or variance analysis of spherical virus particles has been recognized as a well-known problem of all existing reconstruction algorithms [82, p. 173], including the standard algorithms EMAN2 [123] and SPIDER [115].

In contrast, HRSS gives a standard deviation function that is organized in *annular* structures as shown in Fig. 6.6 (c) and more obviously in Fig. 6.7 (b). Such an annular structure obtained by HRSS matches the physical organization of the particle, for instances, the outer protein shell and the inner core of nucleic acid. This makes more biological sense than the estimates of HRSI and other reconstruction algorithms. Such a distinction can be further seen in Fig. 6.8, in which Fig. 6.8 (a) has light blue radial lines, whereas the Fig. 6.8 (b) shows the detailed annular structure of the virus. In the previous analyses with the use of HRSI, features like high values located along radially directed lines averaged out leaving interpretable information, but as we try to increase the spatial detail of our interpretation, such behavior is difficult to understand.

6.6 Conclusion

In this paper, we proposed a novel approach HRSS for 3-D reconstruction of nanoscale virus particles from noisy 2-D projection images. Realistic assumption on the heterogeneous virus particles requires sophisticated tools. HRSS

incorprates the complete basis functions to realize the sophisticated situation of symmetrical statistics, which eliminates the long-standing distortions in heterogeneity calculations associated with symmetry axes, and provides estimates that make more biological sense than the previous estimates. This implies that the variability in the particles is such that individual particles lack symmetry and only the first and second order *statistics* obey the symmetry. This is natual for such large objects as viruses (10^2 – 10^3Å, 10 Megadalton) in the absence of the additional geometric constraints that occur in the crystal of an x-ray crystallography experiments.

CHAPTER 7

STATISTICAL CHARACTERIZATION OF ENSEMBLES OF ICOSAHEDRALLY SYMMETRIC VIRUS PARTICLES FROM ELECTRON MICROSCOPE IMAGES: INVESTIGATION ON THE BACTERIOPHAGE HK97 PROHEAD I

7.1 Introduction

A virus particle transforms into continuous heterogeneous structures along its maturation process. As the structure determines properties of a virus, i.e., being infectious or not, it has been a important topic to understand the structure as well as the dynamics of the maturation process of a virus particle. The maturation process of virus particles is characterized by a sequence of intermediates. Virus-like particles (VLPs) derived from the bacteriophage HK97, which have several of these intermediates stabilized and isolated, i.e., HK97 Prohead I and HK97 Prohead II, have been used as the exemplary particles to study the maturation of double stranded (ds) DNA bacteriophage. Our work is focusing on the statistical characterization of two intermediates of HK97 Prohead I, in particular, the Prohead I with protease (PhI^{Pro+}) and the Prohead I without protease (PhI^{Pro-}).

The VLP HK97 Prohead I (PhI^{Pro+}) contains a protein capsid and approximately 100 viral protease molecules where the protease molecules have been rendered non-functional by modification of the viral protease gene. A second VLP of HK97 Prohead I can also be produced which simply lacks the viral protease molecule, and this second VLP is denoted by PhI^{Pro-}. Both cryo-EM structures of PhI^{Pro+} and PhI^{Pro-} have been previously reported [130] and they are

both icosahedral particles. Using the same data set, [51] characterizes the spatial dynamics of PhI^{Pro+} and PhI^{Pro-} through analyzing the variances by using the existing algorithm, heterogeneous reconstruction with symmetrical individuals (the HRSI algorithm introduced in [148, 133]). Comparing these two different particles (PhI^{Pro+} and PhI^{Pro-}), biochemical experiments suggested that PhI^{Pro+} was more resistant to the disassembly conditions. The previous variance analysis using HRSI [51] further showed that PhI^{Pro-} had roughly twice the standard deviation of PhI^{Pro+}, especially in the δ-domain. Therefore, PhI^{Pro+} particle had a greater stability. When the standard deviation map is visualized, there are peaks in the standard deviation map that are located in the neighborhood of the icosahedral symmetry axes of the particle and which extend from the center of the particle to the surface [51]. There is no biological explanation of the peaks. This pattern is a well-known problem of variance analysis of particles with symmetries [82], which has no biological explanation.

The VLP HK97 Prohead I includes a central core of DNA nucleic acid and an capsid of protein. In HK97 we are particularly interested in how events on the inner surface of the capsid (the so-called δ domain where the viral protease cleaves 104 Å from the capsid protein during maturation) are related to the remainder of the capsid. However, extracting biological understanding from the covariance function $C_\rho(\mathbf{x}, \mathbf{x}')$ is challenging. Existing software, e.g., EMAN2 [123] and HRSI [148] can only compute the variance map of the particle. For example, in the previous analyses of NωV [133, 124] and HK97 [51], spherical averages of the variance map, where the variance map is defined by $D_\rho(\mathbf{x}) = C_\rho(\mathbf{x}, \mathbf{x})$, have played a major role. The cryo-EM experiment suggested that the δ-domain contains a disordered δ-domain which merges into the central core, and a partially ordered δ-domain which is between the disordered δ-domain and the or-

dered capsid, which is the outer surface of the capsid. The formation and maturation of the capsid has long been discussed, e.g., [49, 68, 51].

In this Chapter, we used a new reconstruction algorithm, heterogeneous reconstruction with symmetrical statistics (HRSS), to investigate the statistics of the structure of HK97 PhI^{Pro+} and PhI^{Pro-}. The variance map estimated by HRSS eliminates the false maxima in heterogeneity near symmetry axes of symmetrical particles. In addition, HRSS avoids the artificial peaks in the disordered δ-domain which exists in previous calculations [51]. Furthermore, for the first time, an analysis on covariance is enabled by HRSS to investigate the interaction between the selected points in the capsid and the remainder particle.

7.2 Mathematical models

7.2.1 The model of reconstruction

The reconstruction process conceptually includes three models. Specifically, a model of the 2D image formation (Eq. 30 in [138]), a model of the structure of the 3D particle (Eq. 3 in [138]) and a model based on the projection theorem, which performs the transformation between 2D and 3D. The third model is detailed in [133, 51].

7.2.2 Covariance and variance analysis

The interaction between two remote locations in the particle can be characterized by computing the covariance between these two locations. In particular,

$$\begin{aligned} C_\rho(\mathbf{x},\mathbf{x}') &= \mathbb{E}[\rho(\mathbf{x})\rho(\mathbf{x}')] \\ &= \mathbb{E}[\left(\sum_\zeta F_\zeta(\mathbf{x})c_\zeta\right)\left(\sum_{\zeta'} F_{\zeta'}(\mathbf{x}')c_{\zeta'}\right)] \\ &= \sum_\zeta\sum_{\zeta'} \mathbb{E}[c_\zeta c_{\zeta'}]F_\zeta(\mathbf{x})F_{\zeta'}(\mathbf{x}') \\ &= \sum_\zeta\sum_{\zeta'} V(\zeta,\zeta')F_\zeta(\mathbf{x})F_{\zeta'}(\mathbf{x}') \\ &= \sum_\zeta\sum_{\zeta'} V(\zeta,\zeta')\left(h_\zeta(r)I_\zeta(\theta,\phi)\right)\left(h_{\zeta'}(r')I_{\zeta'}(\theta',\phi')\right) \\ &= \sum_\zeta\sum_{\zeta'} V(\zeta,\zeta')h_\zeta(r)h_{\zeta'}(r')I_\zeta(\theta,\phi)I_{\zeta'}(\theta',\phi') \end{aligned} \tag{7.1}$$

where F_ζ is the basis function which includes the angular part I_ζ and a radial part h_ζ as is described in Section 3 [138], and $V(\zeta,\zeta')$ is the (ζ,ζ')'s entry of the covariance matrix V of the coefficients c_ζ. The variance map is Eq. 7.1 evaluated at $\mathbf{x}' = \mathbf{x}$. Specifically,

$$D_\rho(\mathbf{x}) = \mathbb{E}[\rho(\mathbf{x})^2] = \sum_\zeta\sum_{\zeta'} V(\zeta,\zeta')h_\zeta(r)h_{\zeta'}(r)I_\zeta(\theta,\phi)I_{\zeta'}(\theta,\phi). \tag{7.2}$$

The correlation between two locations is computed by

$$\bar{C}_\rho(\mathbf{x},\mathbf{x}') = \frac{C_\rho(\mathbf{x},\mathbf{x}')}{s_\rho(\mathbf{x})s_\rho(\mathbf{x}')}, \tag{7.3}$$

where $s_\rho(\mathbf{x})$ is the standard deviation computed by $s_\rho(\mathbf{x}) = \sqrt{D_\rho(\mathbf{x})}$.

Note that Eq. 7.1 is a function of two three-dimensional vectors, i.e., a cube in 6-D which is difficult to visualize. Because the function of the materials inside of a virus particle differentiates roughly along the radius, we are also interested in the covariance function at two locations at different radii but along the same

radially-directed line, i.e., $x = r\hat{u}$ and $x' = r'\hat{u}$ where $\hat{u}$ is a radially-directed unit vector, i.e., $\hat{u} = \hat{r}$ in spherical coordinates or $\hat{u}$= $(\sin\theta\cos\phi,\ \sin\theta\sin\phi,\ \cos\theta)$ in rectangular coordinates. Averaging the covariance (Eq. 7.1) over the surface of a sphere gives

$$\begin{aligned} z_\rho(r,r') &= \frac{1}{4\pi}\int C_\rho(\mathbf{x},\mathbf{x}')d\Omega \\ &= \frac{1}{4\pi}\int_{\theta=0}^{2\pi}\int_{\phi=0}^{\pi} C_\rho(x,x')\sin\theta \mathrm{d}\theta\mathrm{d}\phi \\ &= \frac{1}{4\pi}\int_{\theta=0}^{2\pi}\int_{\phi=0}^{\pi} C_\rho(x,x')\sin\theta \mathrm{d}\theta\mathrm{d}\phi \\ &= \sum_\zeta\sum_{\zeta'} V(\zeta,\zeta')h_\zeta(r)h_{\zeta'}(r')\left(\frac{1}{4\pi}\int_{\theta=0}^{2\pi}\int_{\phi=0}^{\pi} I_\zeta(\theta,\phi)I_{\zeta'}(\theta',\phi')\sin\theta\mathrm{d}\theta\mathrm{d}\phi\right) \\ &= \sum_\zeta\sum_{\zeta'} V(\zeta,\zeta')h_\zeta(r)h_{\zeta'}(r') \end{aligned} \tag{7.4}$$

based on the orthonormality of the angular functions. The function $z_\rho(r,r')$ can be easily visualized as a 2-D image. We also make plots for the square root of the spherical average of the variance for each particle, specifically,

$$\begin{aligned} \bar{s}_\rho(r) &= \sqrt{\frac{1}{4\pi}\int D_\rho(\mathbf{x})\mathrm{d}\Omega} \\ &= \sqrt{\sum_\zeta\sum_{\zeta'} V(\zeta,\zeta')h_\zeta(r)h_{\zeta'}(r)}, \end{aligned} \tag{7.5}$$

which is referred as the spherical average of the standard deviation in the remainder of the paper. To compare the difference of the standard deviation between two different particles numerically, we compute the difference between the two spherical average of the standard deviations, i.e.,

$$\bar{d}_\rho(r) = \frac{\bar{s}_\rho^{(1)}(r) - \bar{s}_\rho^{(2)}(r)}{\frac{1}{R_2-R_1}\int_{r=R_1}^{R_2} s_\rho^{(2)}(r)r\mathrm{d}r}. \tag{7.6}$$

Here, the two particles are assumed to have the following relation, $\frac{1}{R_2-R_1}\int_{r=R_1}^{R_2} s_\rho^{(2)}(r)r\mathrm{d}r < \frac{1}{R_2-R_1}\int_{r=R_1}^{R_2} s_\rho^{(1)}(r)r\mathrm{d}r$.

7.3 Results and Analysis

By using the same image stack provided in [130] and used in [51], two sets of 1200 cryo-EM images were selected for both PhI^{Pro+} and PhI^{Pro-}. Following the same data processing as is described in Section 6.5.1, the following reconstructions were computed:

1. Homogeneous solutions in low resolution (basis functions with $p = 1$, l up to 10 and q up to 20) computed by HRII. There are four such homogeneous solutions computed from the two data sets of PhI^{Pro+} and the two data sets of PhI^{Pro-}.
2. Heterogeneous solutions using the complete basis functions (basis functions with all p's, l up to 10 and q up to 20) computed by HRSS. The four heterogeneous solutions were computed by using the four homogeneous solutions in 1 as the initial condition.
3. Homogeneous solutions in high resolution (basis functions with $p = 1$, l up to 55 and q up to 20) computed by HRII. Two solutions were computed. One was computed from the one of the two data sets of PhI^{Pro+}, and the other was computed from one of the data sets of PhI^{Pro-}.
4. Masked high resolution homogeneous solutions. The two mean electron scattering intensity (the 3D structures) computed in 3 are denoised by applying a masking procedure Specifically, all values that are in the radius range of $R \geq 268$ are replaced to be zeros, because the largest radii of the atomic coordinates from the X-ray crystallography structure of Prohead-I [60] (3p8q) is 268 Å.

7.3.1 Analysis of mean electron scattering intensity (the structure)

The FSC of the mean electron scattering intensity was computed based on the homogeneous solution in high resolution (Result 3), which is shown in the left panel of Fig. 7.1. The resolutions are determined by the fact that the FSC curve crosses the 0.5 level which is at 0.061 $Å^{-1}$ for PhI^{Pro+}, at 0.056 $Å^{-1}$ for PhI^{Pro-}, and at 0.053 $Å^{-1}$ for PhI^{Pro+} v.s. PhI^{Pro-}. Therefore, the resolution for the above three cases is 16.39 Å, 17.86 Å and 18.87 Å, respectively. The corresponding energy curves (the denominators of the FSC calculation) are shown in the right panel of Fig. 7.1.

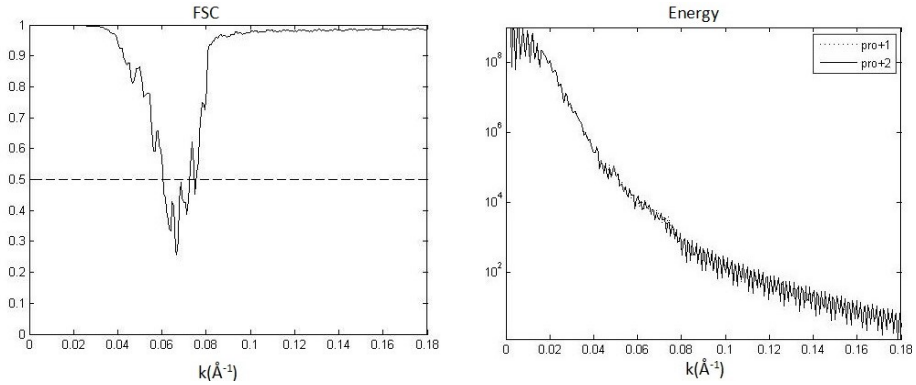

(a) two sets of PhI^{Pro+}

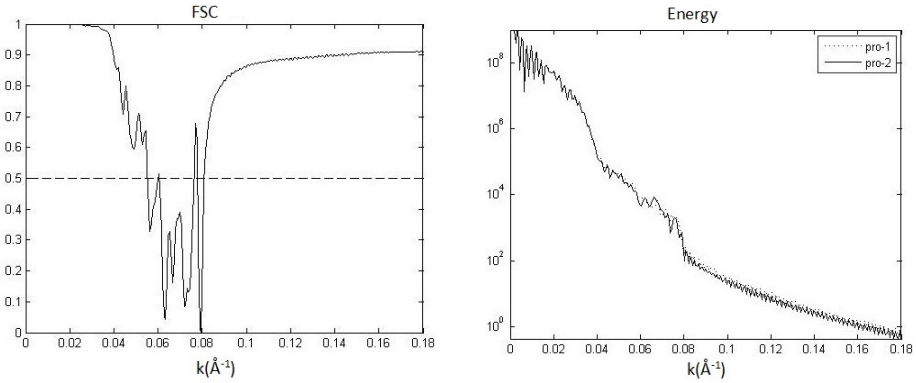

(b) two sets of PhI^{Pro-}

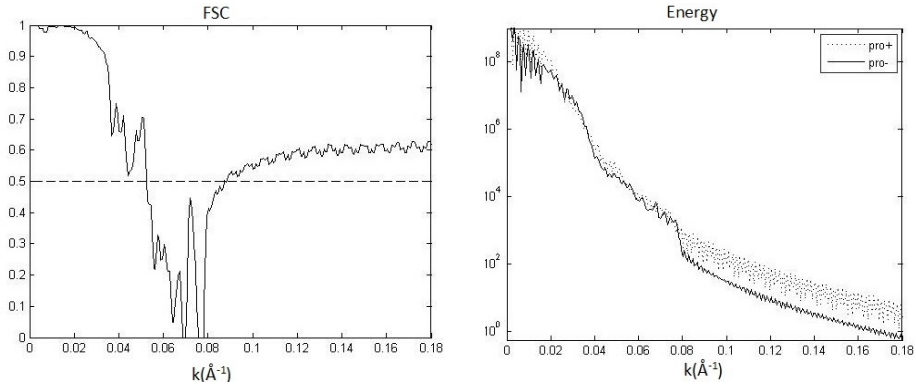

(c) PhI^{Pro+} v.s. PhI^{Pro-}

Figure 7.1: FSC (left) and Energy (right) of the mean electron scattering intensity for the homogeneous solutions. (a) comparison between the two calculations of PhI^{Pro+}, (b) comparison between the two calculations of PhI^{Pro-}, and (c) comparison between one calculation of PhI^{Pro+} and one calculation of PhI^{Pro-}.

7.3.2 Analysis on variance (heterogeneity dynamics)

The variance analysis of HRSS is shown in this Section. Our result is compared with the previous HRSI result provided in [51]. The heterogeneity of HK97 PhI^{Pro+} and PhI^{Pro-} are visualized in Figs. 7.2 and 7.3. Fig. 7.2 shows the outer surface of the mean electron scattering intensity (which is the structure), and Fig. 7.3 shows a cross section of the mean electron scattering intensity. All structures are colorized by the standard deviation (which characterizes the heterogeneity) provided in [51] in (a) and computed by HRSS in (b).

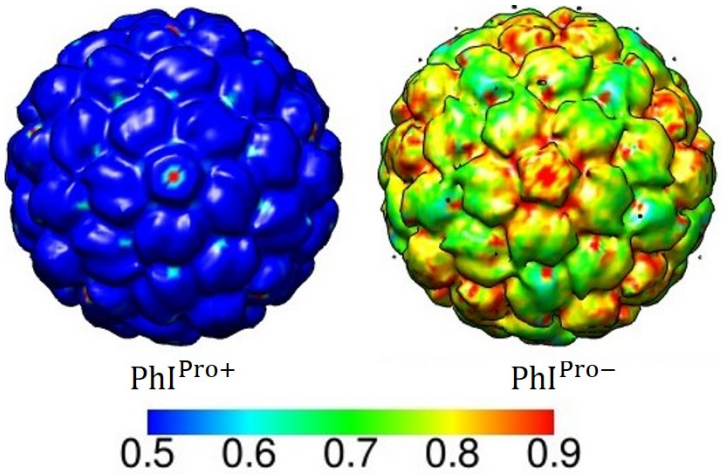

(a) HRSI results provided in [51]

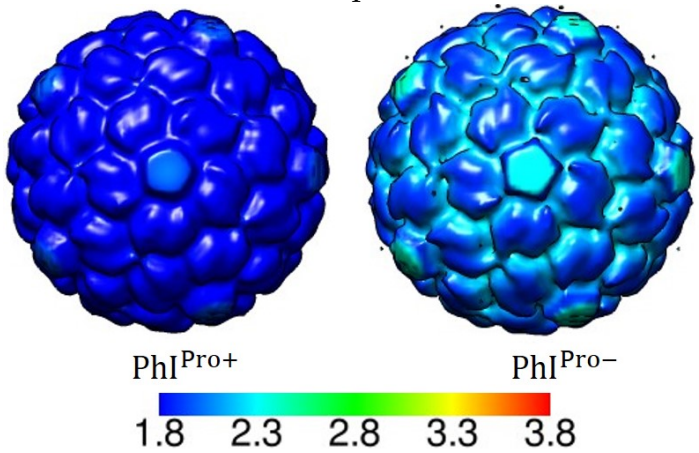

(b) HRSS results

Figure 7.2: Visualization of the heterogeneity: external surface of the mean electron scattering intensity (which is the structure) at volume level 3.5e-4 with colors determined by the standard deviation (which is the characterization of heterogeneity). Both the HRSI calculation provided in [51] and the HRSS calculation show that the PhI^{Pro-} structure has greater heterogeneity than the PhI^{Pro+} structure which is emphasized through warmer color in the right column. The structures are the high resolution homogeneous solutions of electron scattering intensity for PhI^{Pro+} (the left column) and PhI^{Pro-} (the right column). This Visualizations are computed by UCSF Chimera [95]. All markings are scaled by 10^{-3}.

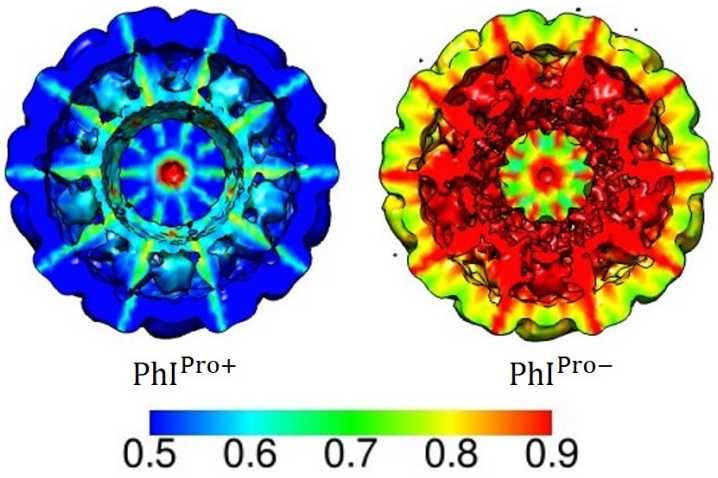

(a) HRSI results provided in [51]

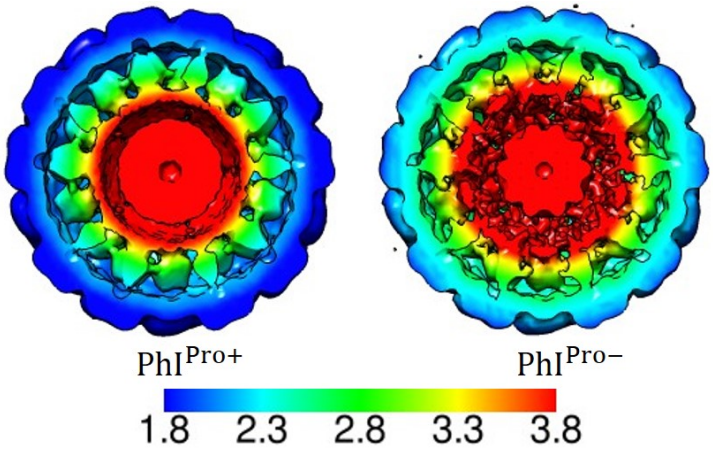

(b) HRSS results

Figure 7.3: Visualization of the heterogeneity: cross section of the mean electron scattering intensity (which is the structure) at volume level 3.5e-4 with colors determined by the standard deviation (which is the characterization of heterogeneity). The $\text{PhI}^{\text{Pro-}}$ structure has greater heterogeneity than the $\text{PhI}^{\text{Pro-}}$ structure which is emphasized in the second column of visualizations where both columns share the same color bar. The standard deviation $s_\rho(\mathbf{x})$ computed by HRSI [51] introduces artificial spikes that radiate from the center core to the external surface of the particle. HRSS computes a $s_\rho(\mathbf{x})$ has the dynamical heterogeneity in consistent to the biological structure of the virus particle. Visualizations are computed by UCSF Chimera [95]. All markings are scaled by 10^{-3}.

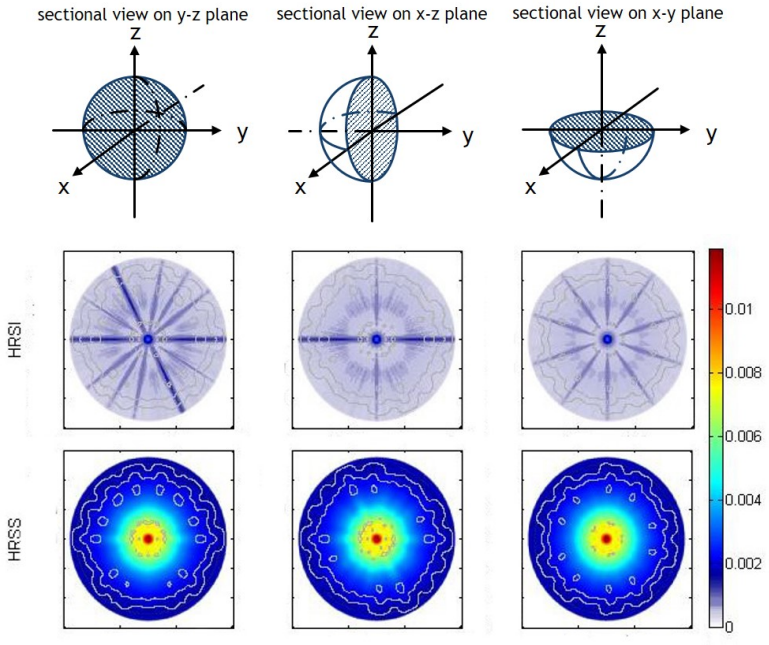

(a) PhI$^{\text{Pro+}}$

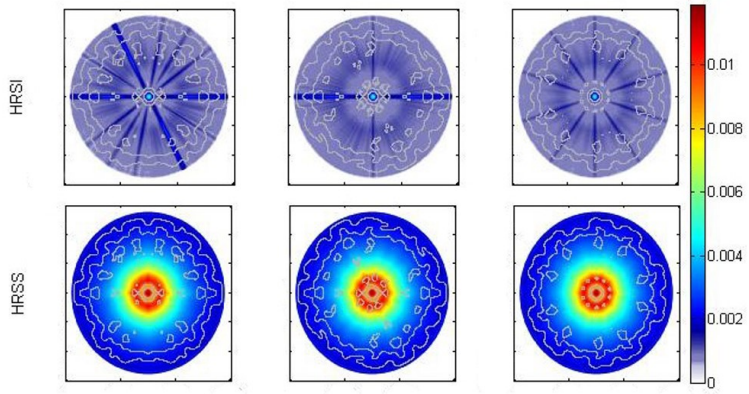

(b) PhI$^{\text{Pro-}}$

Figure 7.4: Cross section of the standard deviation function $s_\rho(\mathbf{x})$ for PhI$^{\text{Pro+}}$ and PhI$^{\text{Pro-}}$ using both HRSI and HRSS which are displayed in a common color map. The standard deviation is superimposed on contours of the structure at contour level 1. The top row shows the three perpendicular cross sections that are used where the x–y contour, which is the third contour, is perpendicular to a 5-fold symmetry axis. The standard deviation computed by HRSI introduces artificial peaks that extend from the central core to the external surface of the particle as well as more isolated peaks within the disordered δ–domain [51] of the particle. In contrast, the standard deviation computed by HRSS lacks the artificial peaks, is organized in annular shells that match the known structure of HK97, and has a larger range of values.

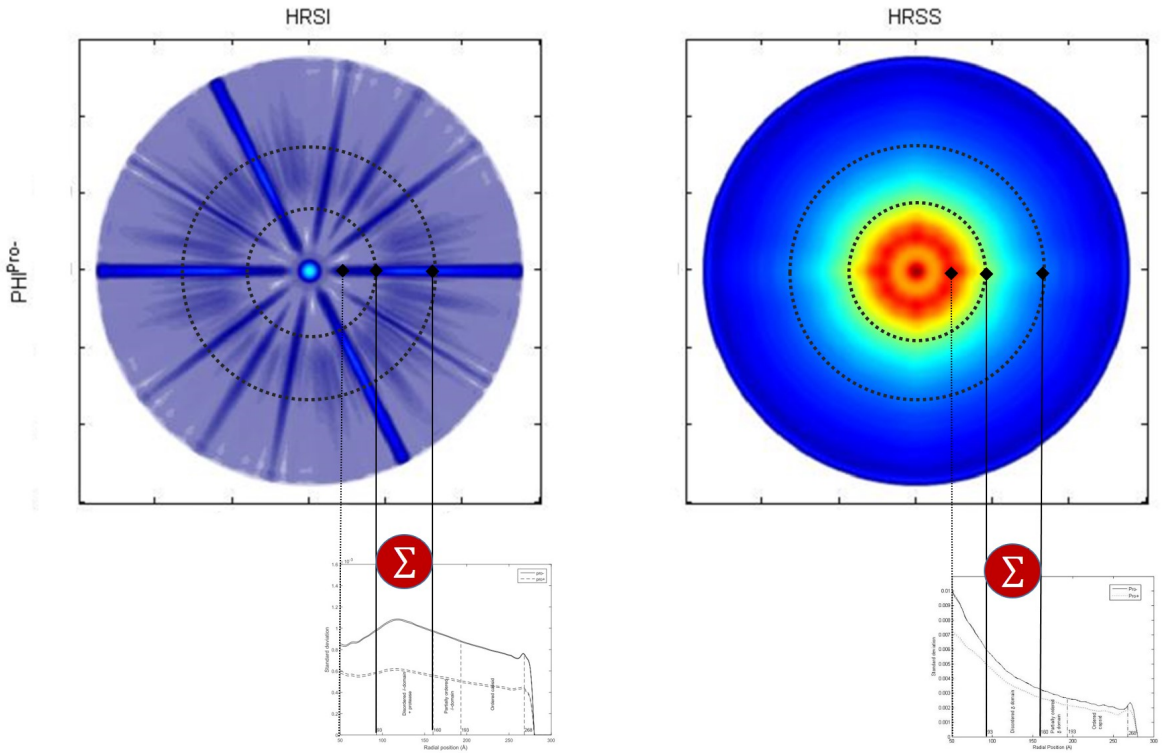

Figure 7.5: Generation of the spherical average of the standard deviations for PhI^{Pro-}. HRSI computes artificial spikes in the disordered δ-domain which introduces a peak for the spherical average of the standard deviation curve in the disordered δ-domain. HRSS results suggest that the material merging to the DNA nucleic acid from the disordered δ-domain has a even higher standard deviation value.

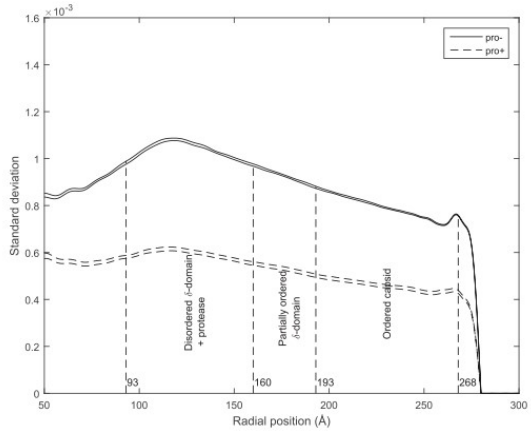

(a) PhI$^{\text{Pro-}}$ v.s. PhI$^{\text{Pro+}}$ (HRSI, Fig.3 (a) in [51])

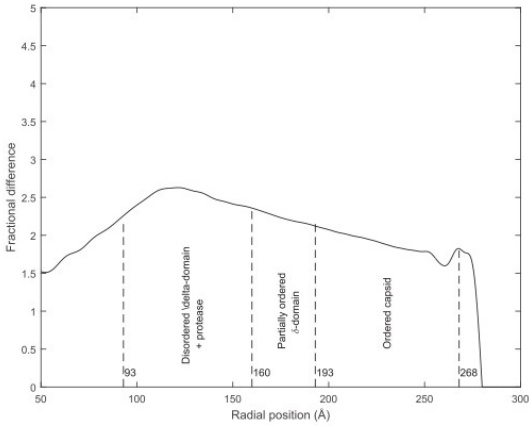

(b) Fraction of PhI$^{\text{Pro-}}$ and PhI$^{\text{Pro+}}$ (HRSI, Fig.3 (b) in [51])

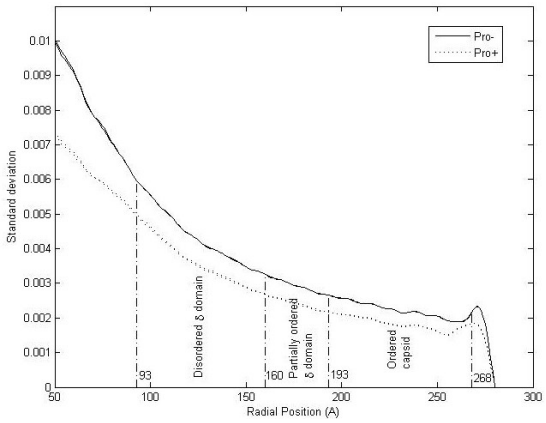

(c) PhI$^{\text{Pro-}}$ v.s. PhI$^{\text{Pro+}}$ (HRSS)

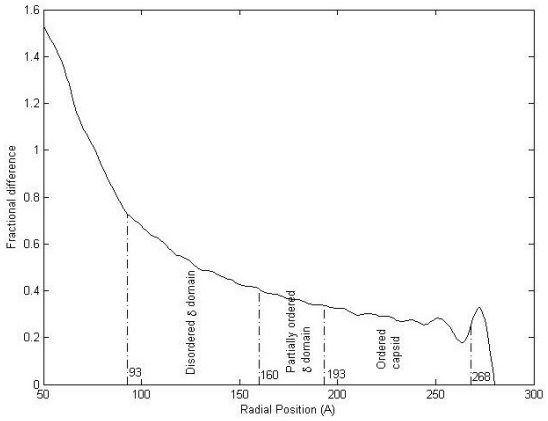

(d) fraction of PhI$^{\text{Pro-}}$ and PhI$^{\text{Pro+}}$ (HRSS)

Figure 7.6: The radial distribution of heterogeneity as described by the spherical average of the standard deviation. The left column show four curves of spherical average, $s_\rho(r)$, for the data sets 1 and 2 for PhI$^{\text{Pro+}}$ and for PhI$^{\text{Pro-}}$. The right column show the one curve of the fraction difference of the spherical average, $\bar{d}(r)$ (Eq. 7.6), after averaging the result for data sets 1 and 2 for PhI$^{\text{Pro+}}$ and for PhI$^{\text{Pro-}}$. Specifically, $\bar{s}_\rho^{(1)}(r)$ in Eq. 7.6 is the average of the two curves of PhI$^{\text{Pro-}}$ and $\bar{s}_\rho^{(2)}(r)$ in Eq. 7.6 is the average of the two curves of PhI$^{\text{Pro+}}$. Several radii are marked. The largest and smallest radii of the atomic coordinates from the X-ray crystallography structure of Prohead-I [60] (3p8q) are 268 Å and 193 Å. The smallest radius of the pseudo-atomic coordinates from the cryo EM structure [130], which includes 20% of the δ-domain, is 160 Å. The radius of the inner surface of the region of highest heterogeneity is 93 Å. Both HRSS and HRSI show that heterogeneity of PhI$^{\text{Pro-}}$ is substantially greater than the heterogeneity of PhI$^{\text{Pro+}}$ at all radii. The amount by which the heterogeneity of PhI$^{\text{Pro-}}$ exceeds the heterogeneity of PhI$^{\text{Pro+}}$ is depicted in the fractional plot.

Four primary distinctions are observed. First, for both PhI$^{\text{Pro+}}$ and PhI$^{\text{Pro-}}$, HRSI gives a covariance function that is organized in radially-directed rays (Fig. 7.3 (a)), whereas HRSS gives a covariance function that is organized in *annular* structures (Fig. 7.3 (b)). Such an annular structure, as is obtained by HRSS, matches the physical structure of the particle: the outer protein shell and the inner core of nucleic acid. This makes more biological sense than the estimates from HRSI. Such a distinction can also be seen in Fig. 7.4, in which the first row of both (a) and (b) have dark blue radial lines, whereas the second rows show the detailed annular structure of the virus. In the previous analyses using HRSI [51], features like high values located along radially directed lines were averaged out leaving interpretable information, but as we try to increase the spatial detail of our interpretation, such behavior is difficult to understand.

Second, HRSS gives a covariance function with larger dynamic range (0–12×10^{-3} for both PhI$^{\text{Pro+}}$ and PhI$^{\text{Pro-}}$) than the earlier HRSI (0–3.1×10^{-3} for PhI$^{\text{Pro+}}$ and 0–4.8×10^{-3} for PhI$^{\text{Pro-}}$). This can be clearly seen in Fig. 7.4 where the same color map is used for both HRSS and HRSI and for both PhI$^{\text{Pro-}}$ and PhI$^{\text{Pro+}}$. The standard deviation estimated by HRSI is essentially pure blue at the lowest level of the color map, while HRSS contributes to a broader range of colors. This is due to the fact that HRSI uses a larger family of basis functions than is used by HRSI and therefore can represent features that HRSI averages away.

Third, heterogeneity dynamics, which is characterized by the standard deviation ($\bar{s}_\rho(r)$ in Eq. 7.5 and $\bar{d}_\rho(r)$ in Eq. 7.6) computed by HRSI and HRSS, show that the PhI$^{\text{Pro-}}$ structure has greater heterogeneity than the PhI$^{\text{Pro+}}$ structure which is emphasized in the second columns of Figs. 7.2–7.3 and 7.6. Comparing

the calculation of HRSI and the calculation of HRSS, e.g., Fig. 7.6 (b) and (d), such a distinction is more substantial in HRSI's calculation [51]. This is caused by the higher resolution in HRSI's calculation than in HRSS's calculations.

Fourth, the previous calculation of HRSI [51] introduces extra spikes encircled in the disordered δ-domain for both PhI^{Pro+} and PhI^{Pro-} as shown in Fig. 7.4–7.6, which suggests the dynamical behavior in the disordered δ-domain disconnected to the center core. In the contrast, the continuous annular structure estimated by HRSS, e.g., Fig. 7.4–7.6, suggests an active interaction between the center core of DNA nucleic acid and the disordered δ-domain. The amount of heterogeneity of PhI^{Pro-} exceeds the heterogeneity of PhI^{Pro-} reaching a maximum at about a radius of 50 Å.

7.3.3 Analysis of covariance

The particle

Two sets of five distant regions on the virus particle are selected. One set aligns with a 2-fold symmetry axis of a icosahedron. The other set aligns with the same radially-directed line which is not any symmetry axis of a icosahedron. For each set of five regions, two of them sit in the ordered capsid domain; one sits in the partially-ordered δ-domain, and the other two sit in the disordered δ-domain. The covariances between each of these five regions and the rest of the particle are computed by Eq. 7.1 (as shown in Supplemental Fig. 7.11 for the five regions off the symmetry axis), which are further normalized into correlation values by Eq. 7.3. The cross section of the correlation map is shown in Fig. 7.7 for both sets of five selected regions.

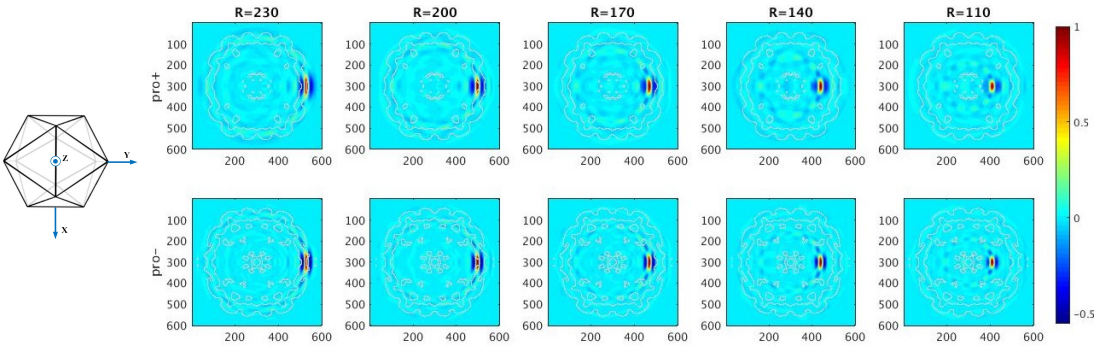

(a) Five selected regions on the 2-fold symmetry axes. The two fold symmetry of the icosahedron is sitting along the Z axis (Left), and the correlation maps (Eq. 7.3) on x-z plane are displayed and masked by the structure at a contour level of 1 (Right).

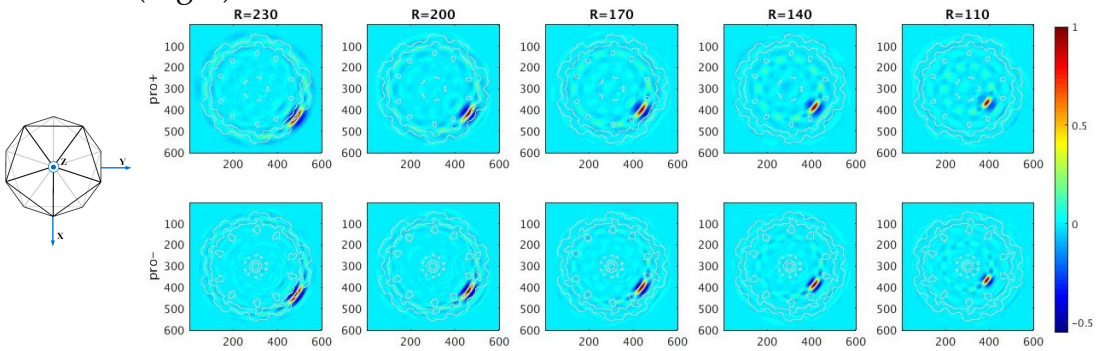

(b) Five selected regions off any symmetry axes. The five fold symmetry of the icosahedron is sitting along the Z axis (Left), and the correlation maps (Eq. 7.3 in Eq. 7.3) on x-y plane are displayed and masked by the structure at a contour level of 1 (Right).

Figure 7.7: Correlation ($\bar{C}_\rho(\mathbf{x}, \mathbf{x}')$ in Eq. 7.3) between selected region and regions of rest of the particle for PhI$^{\text{Pro+}}$ and PhI$^{\text{Pro-}}$. The large red regions in the first two columns of the right panels validate the fact that this domain of the capsid is well-ordered. The irregular small dots in last two columns (R=140 Å and R=110 Å) and the middle sized red region at R=170 Å validate the fact that the δ-domain near the central core is disordered and it becomes more ordered when it's merging to the ordered capsid domain.

Each highly correlated (red) region in Fig. 7.7 depicts the small piece of material which the selected region belongs to. Comparing Fig. 7.7 (a) and (b), the materials in the virus particle are formed indifferently on the same radius in the

capsid, but are formed differently on different radius in the capsid. In particular, as the radius decreases, the red region in Fig. 7.7 transforms from a large regular half spheroid to small irregular half spheroid. This transition is indifferent to the regions on or off the symmetry axis of a icosahedron, which is biologically reasonable. Fig. 7.12 in the Supplementary material suggests that comparing to the rest of the particle, the selected regions are strongly correlated to regions in the same annulus. Comparing to PhI$^{\text{Pro-}}$, the regions on the same annulus in PhI$^{\text{Pro+}}$ appears to be more strongly correlated. This result verifies the annular structure in the capsid of a virus particle, as well as the hypothesis that PhI$^{\text{Pro+}}$ has a more stable annular structure than PhI$^{\text{Pro-}}$.

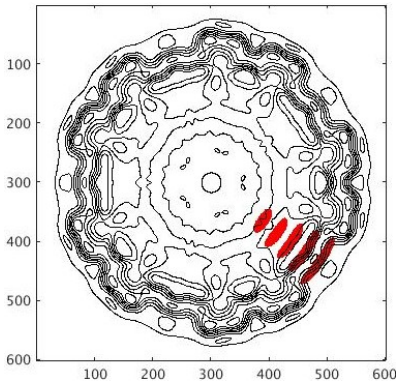

(a) selected proteins masked by the contour level of the virus particle

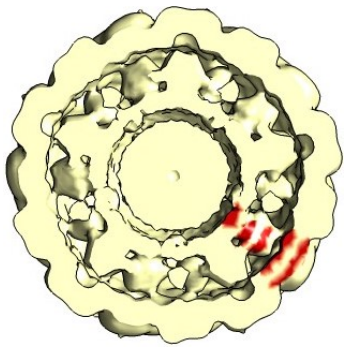

(b) selected proteins in the 3D structure of the virus particle

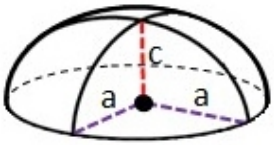

(c) The contour of highly correlated protein

Figure 7.8: Selected pieces of protein in different radial domain in the capsid of PhI$^{\text{Pro+}}$. Each protein piece is determined by the binarized correlation map which has 1 if $\bar{C}_\rho(\mathbf{x}, \mathbf{x}') \geq 0.4$ and 0 if $\bar{C}_\rho(\mathbf{x}, \mathbf{x}') < 0.4$. Proteins in the capsid transit from a disordered form to an ordered form from the inner to the outer surface. The contour of each highly correlated protein piece can be emulated by a half spheroid.

Through a filtering technique, the correlation maps of the five off symmetry axes regions (Fig. 7.8 (b)) are binarized to 1 if $\bar{C}_\rho(\mathbf{x}, \mathbf{x}') \geq 0.4$, and to 0 if $\bar{C}_\rho(\mathbf{x}, \mathbf{x}') < 0.4$. Then, five pieces of protein in the capsid are determined by these five binarized correlation maps. These protein pieces in the capsid of PhI^{Pro+} are then jointly displayed in Fig. 7.8 (a) and (b). The volume of each of these protein pieces is tabulated in Table 7.1. The contour of each of these protein pieces can be emulated by a half spheroid (Fig. 7.8 (c)), which has the semi-axis lengths tabulated in Table 7.1.

Distance from the center of spheroid to the origin R (Å)	230	200	170	140	110
volume ($Å^3$)	92752	73442	54140	38417	24275
semi-axis a (Å)	72	63	55.5	45	36.5
semi-axis c (Å)	9.5	10.5	11	11.5	11

Table 7.1: The size and shape of the selected pieces of protein in the capsid of PhI^{Pro+}. The size and the shape are characterized by the volume and semi-axis lengths of the half spheriod.

The results numerically validate the transition in the orderedness of materials in different domains of the capsid. In particular, as the radius increases from the inner to the outer surface of the capsid, the structure of the protein in the capsid transits from a disordered form to an ordered form. This transition appears to be continuous along the radius.

The spherical average of the covariance (Eq. 7.4) is computed and plotted in Fig. 7.13 in the Supplementary material.

The ribbon diagram

In this section, the covariance analysis for the ribbon diagram is described. Specifically, a fixed location is selected in δ-domain by averaging spatial coordinates of all regions on the four alpha helices, so its spatial location is in the center of the alpha helices that point downwards. Covariance ($C_\rho(\mathbf{x}, \mathbf{x}')$ in Eq. 7.1) between this fixed location and all regions on the ribbon is computed for both PhI$^{\text{Pro+}}$ and PhI$^{\text{Pro-}}$.

In Fig. 7.9, the ribbon is colored by the covariance values which are saturated the covariance 0.5 (red) or -0.5 (blue). A wider color range is used and shown in Fig. 7.14 in the Supplementary material. However, comparing to the narrower color range, the wider one (Fig. 7.14) shows much less details about the interaction between the δ-domain and the ordered capsid.

Suggested by the higher covariance between the fixed point in δ-domain and the ordered capsid (Fig. 7.9 (a)), PhI$^{\text{Pro+}}$ is demonstrating allosteric connections between the fixed location and the surface of the capsid while PhI$^{\text{Pro-}}$ is not. The distinction between PhI$^{\text{Pro+}}$ and PhI$^{\text{Pro-}}$ demonstrates that the binding protease causes a correlation of movement between delta domain and outer region that does not exist without protease. This agrees with the previous experimental results [130], which suggests that the binding protease cause a different H/D distribution from not binding protease that includes effects at a distance (A loop near the surface) from the primary binding site (delta domain). Furthermore, our result also numerical validates the previous hypothesis of mechanical models e.g., Fig. 4 in [49] and Fig. 3 in [68]. In particular, interactions of the delta domains cause the distortions in the tertiary structure of the subunit on the outer

surface (action at a distance).

Both experiments and models as well as the novel covariance analysis suggest that the entire structure is sufficiently dynamic without protease that the subtleties of the change that interacting delta domains make on the tertiary structure are difficult to discern, but binding protease "freezes" these changes so that they can be measured by both H/D and covariance. This is a very neat outcome because after the delta domains have been cleaved off (prohead II), the changes to the outer regions induced by the delta domain interactions before cleavage are now frozen (stabilized by capsid quaternary structure) with sufficient robustness that we could see them at better than 4Å resolution by crystallography. Of course this makes prohead II metastable and makes maturation a "down hill" process energetically. Similar results were observed in the calculation of the second non-overlapping set of 1200 images as shown in Fig. 7.15 in the Supplementary material, which demonstrates the robustness of these effects.

Comparing to previous methods and analysis, the the novel covariance analysis illustrates structural changes that are sufficiently subtle that they are not discernible from direct observation of electron scattering density, but are visible with the derived statistical analysis.

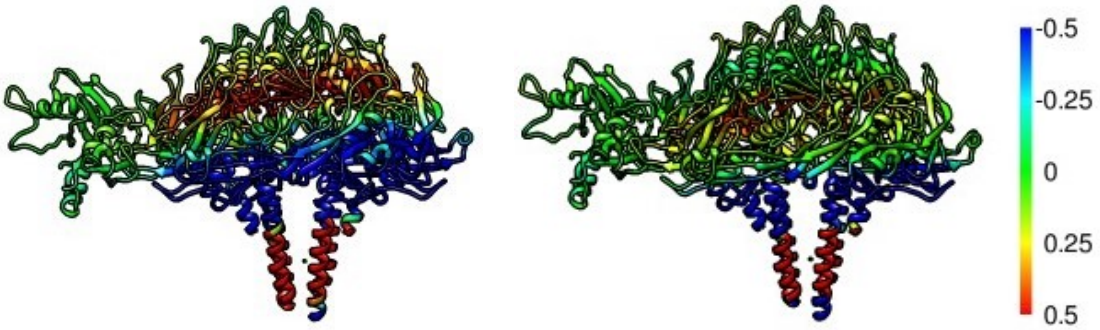

(a) $\text{PhI}^{\text{Pro+}}$ (Dataset 1) (b) $\text{PhI}^{\text{Pro-}}$ (Dataset 1)

Figure 7.9: A ribbon diagram from the x-ray crystallography structure of HK97 augmented with part of the δ domain from the cryo EM structure [130] colored by the 3-D covariance ($C_\rho(\mathbf{x}, \mathbf{x}')$ in Eq. 7.1) where the fixed location is at the black dot in the δ domain (in the center of helices). The view is tangential to the capsid with the outer surface of the capsid at the top. The smaller domain to the left is extending to a 5-fold symmetry axis. Both $\text{PhI}^{\text{Pro+}}$ (b) and $\text{PhI}^{\text{Pro-}}$ (c) are shown. Panels (b–c) use a color map with a narrow range (saturation occurs at 0.5 (red) and -0.5 (blue) and 13.44% of all carbon atoms are saturated) which, however, provides good contrast in the order region of the capsid. In both $\text{PhI}^{\text{Pro+}}$ and $\text{PhI}^{\text{Pro-}}$, the δ domain is saturated at 0.5 (red) or -0.5 (blue) with a small amount of green as it transitions between the two saturated regions. However, $\text{PhI}^{\text{Pro+}}$ and $\text{PhI}^{\text{Pro-}}$ have different behaviors in the ordered capsid. In particular, in $\text{PhI}^{\text{Pro+}}$, the outer part of the capsid is yellow to red (covariance 0.25 to 0.5) but in $\text{PhI}^{\text{Pro-}}$ the ordered capsid is green (some barely yellow) (covariance 0 to barely 0.25). In summary, there is stronger positive covariance between the fixed location in the δ domain and the surface of the capsid in $\text{PhI}^{\text{Pro+}}$ rather than $\text{PhI}^{\text{Pro-}}$.

7.4 Supplemental

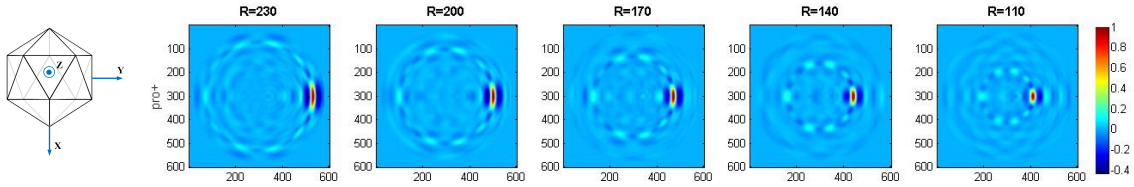

(a) Five selected regions on the 3-fold symmetry axes. The three fold symmetry of the icosahedron is sitting along the Z axis (Left), and the correlation maps (Eq. 7.3) on x-z plane are displayed.

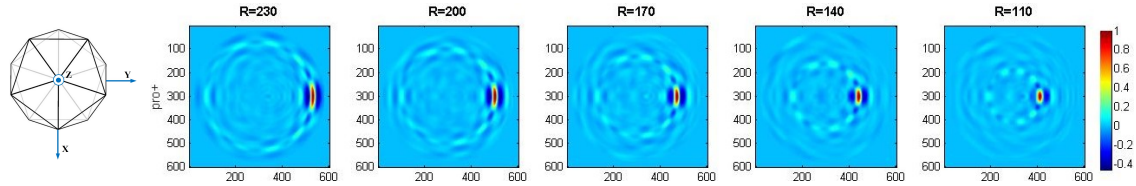

(b) Five selected regions on the 5-fold symmetry axes. The five fold symmetry of the icosahedron is sitting along the Z axis (Left), and the correlation maps (Eq. 7.3) on x-y plane are displayed.

Figure 7.10: Correlation ($\bar{C}_\rho(\mathbf{x}, \mathbf{x}')$ in Eq. 7.3) between selected region and regions of rest of the particle for $\text{PhI}^{\text{Pro+}}$.

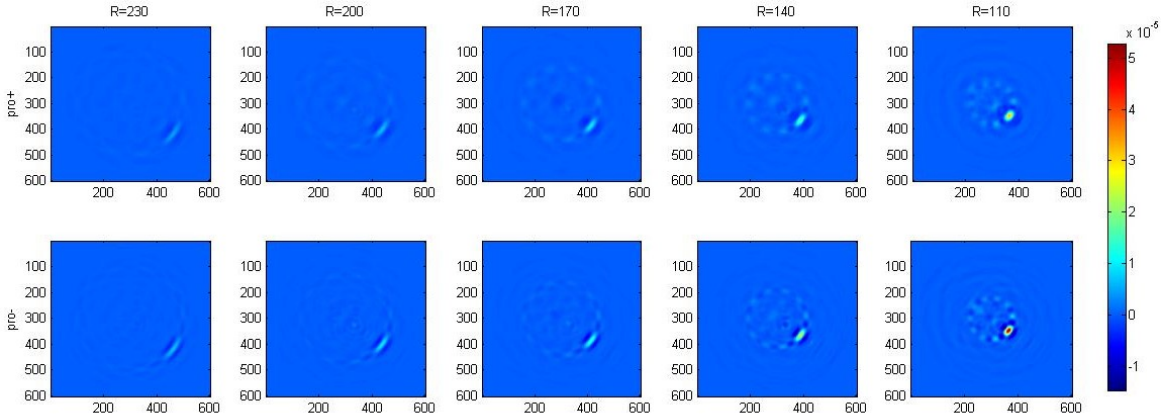

Figure 7.11: Covariance ($C_\rho(\mathbf{x}, \mathbf{x}')$ in Eq. 7.1) between selected region off any symmetry axis and regions of rest of the particle for PhI^{Pro+} and PhI^{Pro-}.The ring of small maxima, that is especially prominent in each of the two R=110 images, is due to the truncation of the orthonormal expansion (Eq. 6.4) to a finite number of terms.

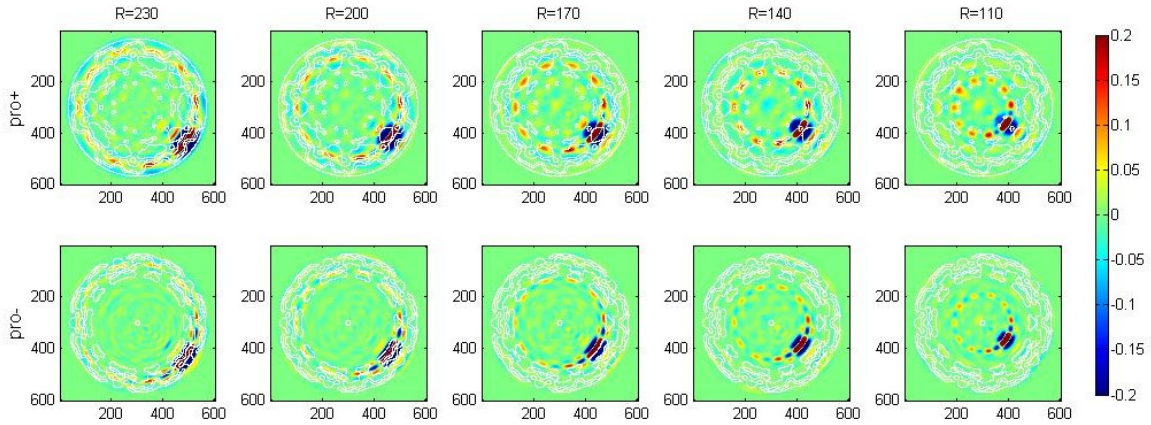

Figure 7.12: Correlation ($\bar{C}_\rho(\mathbf{x}, \mathbf{x}')$ in Eq. 7.3) between selected region off any symmetry axis and regions of rest of the particle for PhI^{Pro+} and PhI^{Pro-} in a saturated colormap in the range [-0.2, 0.2]. The large red regions in the first two columns validate the fact that this domain of the capsid is well-ordered. The irregular small dots in last two columns (R=140 Å and R=140 Å) and the middle sized red region around R=170 Å validate fact that the δ-domain near the central core is disordered and it becomes more ordered when it's merging to the ordered capsid domain. The ring of small maxima in each image is due to the truncation of the orthonormal expansion (Eq. 6.4) to a finite number of terms. Particles are viewed in the cross sections of the x-y plane.

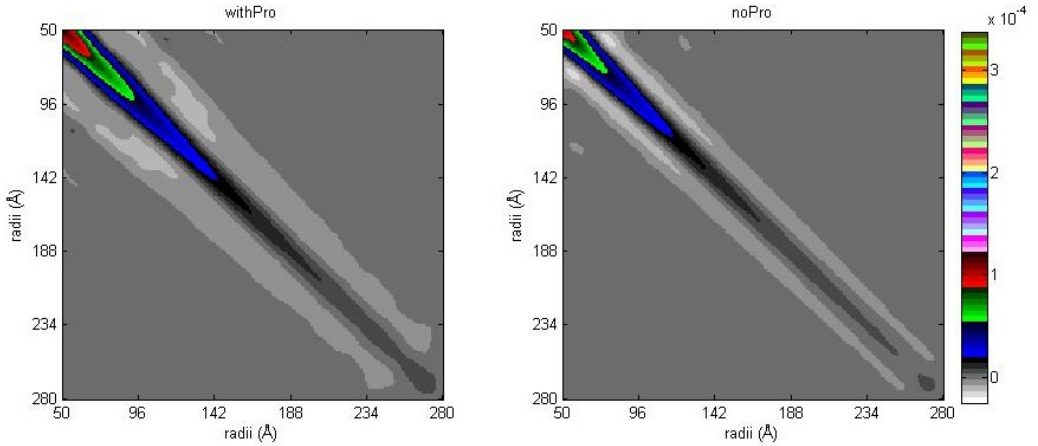

Figure 7.13: Spherical average of the covariance (Eq. 7.4) for both PhI^{Pro+} and PhI^{Pro-}.

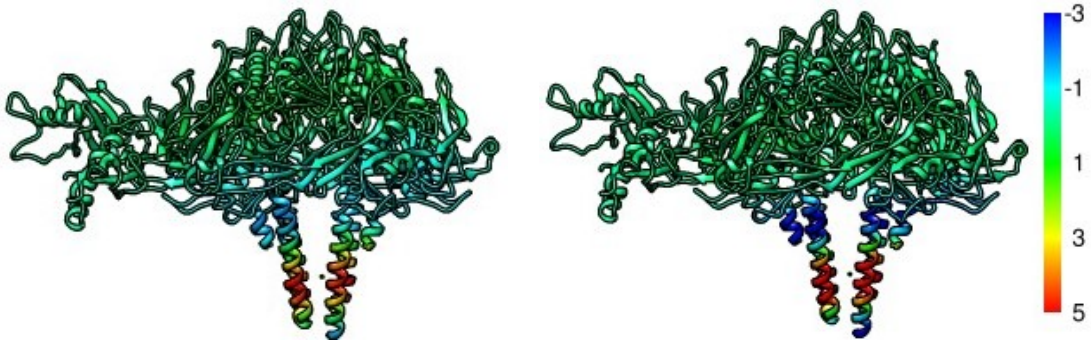

(a) PhI^{Pro+} (Dataset 1) (b) PhI^{Pro-} (Dataset 1)

Figure 7.14: Covariance ($C_\rho(\mathbf{x}, \mathbf{x}')$ in Eq. 7.1) between the a fixed location in δ-domain (the black dot) and all regions on the ribbon for both PhI^{Pro+} and PhI^{Pro-}. The color is saturated at the value of covariance 5 (red) or -3 (blue). Most of the ordered capsid is compressed into green-blue for both PhI^{Pro+} and PhI^{Pro-}.

(a) The fixed location (the black dot) in δ-domain

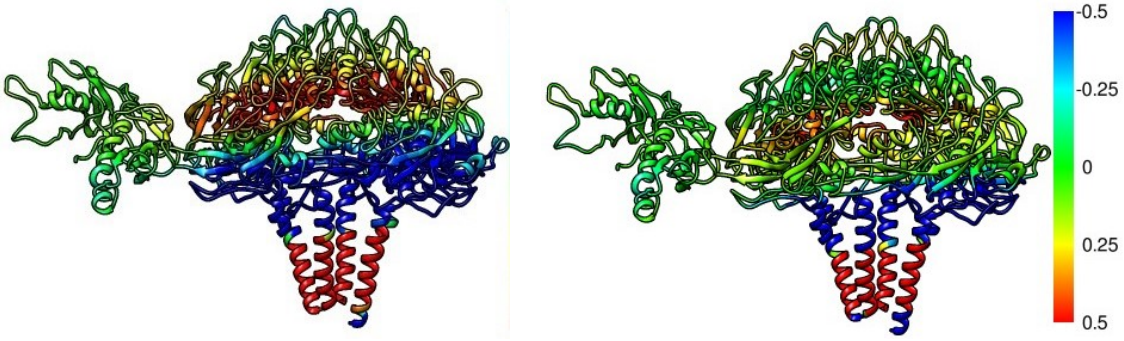

(b) PhI$^{\text{Pro+}}$ (Dataset 2) (c) PhI$^{\text{Pro-}}$ (Dataset 2)

Figure 7.15: Covariance ($C_\rho(\mathbf{x}, \mathbf{x}')$ in Eq. 7.1) between the a fixed location in δ-domain (a) and all regions on the ribbon for both PhI$^{\text{Pro+}}$ and PhI$^{\text{Pro-}}$. The color is saturated at covariance 0.5 (red) or -0.5 (blue) and 12.89% of the all carbon atoms are saturated. The δ domain is saturating at 0.5 (red) or -0.5 (blue) with a tiny amount of green when it zooms from positive to negative. Comparing PhI$^{\text{Pro+}}$ and PhI$^{\text{Pro-}}$, different behavior in the ordered capsid is identified. In particular, in PhI$^{\text{Pro+}}$ the outer part of the capsid is yellow to red (covariance 0.25 to 0.5) but in PhI$^{\text{Pro-}}$ the ordered capsid is green (some barely yellow) (covariance 0 to barely 0.25). This suggests that PhI$^{\text{Pro+}}$ is demonstrating allosteric connections between the fixed location and the surface of the capsid while PhI$^{\text{Pro-}}$ is not.

CHAPTER 8

FUTURE DIRECTIONS

Two applications are investigated in this thesis: resting-state functional magnetic resonance imaging (rs-fMRI) and structural biology of viruses via cryo electron microscopy (cryo EM).The cryo EM work is fundamentally statistical in nature while the rs-fMRI work attempts to avoid statistical assumptions because of the uncertain statistical character of the MRI signals.

There are several future directions for the cryo EM work. (1) More efficient software is needed so that calculations can be carried out at higher resolution. For instance, distributed memory parallelism opportunities exist but are not exploited in the current software. In addition, more efficient optimization algorithm than EM algorithm could be used. (2) Other rotational point group symmetries beyond icosahedral symmetry occur in structural biology. Expansion on the software is required for other symmetries with real-valued irrep matrices. For symmetries where such real-valued irreps do not exist, theoretical development is necessary, in particular, to work with complex-valued basis functions and impose the fact that the electron scattering intensity is real valued by some additional mechanism.

There are also several future directions for the rs-fMRI work. (1) Only pairwise interactions among the regions of interest (ROIs) are considered in this work. Consideration of multiple ROIs simultaneously may be useful when A effects both B and C and it is difficult to distinguish between the true situation and a situation where $A \rightarrow B \rightarrow C$ or $A \rightarrow C \rightarrow B$. (2) The approach used is to compute a prediction and correlate the prediction and the measured signal. More sophisticated predictors could be used, such as nonlinear predictors and

predictors with sparse dependence on the past of the signal from which the prediction is made.

For both the rs-fMRI and cryo EM work, more detailed application of these algorithms to experimental data is sure to yield insights into the functioning of the algorithms and how the algorithms can be improved, as well as providing novel inferences into the biological processes.

APPENDIX A

APPENDIX OF CHAPTER 5

A.1 Proofs of Lemmas

Proof of Lemma 1. Eq. 5.1 implies Eq. 5.2) Γ_r^p is real by definition so that

$$\Gamma_r^p(g) = (\Gamma_r^p(g))^*$$

. Since $\Gamma_r^p = (S^p)^H \Gamma_c^p(g) S^p$, it follows that

$$\Gamma_r^p = (S^p)^H \Gamma_c^p(g) S^p = \left((S^p)^H \Gamma_c^p(g) S^p\right)^* = (S^p)^T (\Gamma_c^p(g))^* (S^p)^*.$$

Multiply on the left by $((S^p)^H)^T = ((S^p)^{-1})^T = ((S^p)^T)^{-1}$ and on the right by $((S^p)^H)^* = (S^p)^T$ to get

$$((S^p)^T)^{-1}(S^p)^H \Gamma_c^p(g) S^p (S^p)^T = (\Gamma_c^p(g))^*,$$

which, since $(S^p)^H = (S^p)^{-1}$, implies that

$$[S^p(S^p)^T]^{-1} \Gamma_c^p(g) [S^p(S^p)^T] = (\Gamma_c^p(g))^*.$$

Therefore $\Gamma_c^p(g)$ is similar to $(\Gamma_c^p(g))^*$.

Eq. 5.2 implies Eq. 5.1) Multiplying by $(S^p)^T$ on the left and $(S^p)^*$ on the right of Eq. 5.2 gives

$$(S^p)^T [S^p(S^p)^T]^{-1} \Gamma_c^p(g) [S^p(S^p)^T] (S^p)^* = (S^p)^T (\Gamma_c^p(g))^* (S^p)^*$$

which can be reorganized using the assumption that S^p is unitary to get

$$[(S^p)^T (S^p)^*] (S^p)^{-1} \Gamma_c^p(g) S^p [(S^p)^T (S^p)^*] = (S^p)^T (\Gamma_c^p(g))^* (S^p)^*.$$

Then, also since S^p is unitary, it follows that

$$(S^p)^{-1} \Gamma_c^p(g) S^p = \left[(S^p)^{-1} \Gamma_c^p(g) S^p\right]^*.$$

Since the left and the right hand sides of the above equation are complex conjugates of each other, it follows that each is real, i.e., $\Gamma_r^p(g) = (S^p)^{-1}\Gamma_c^p(g)S^p$ is a real-valued matrix. □

Proof of Lemma 2. Property 1: Because the irrep is unitary, Z^p can be written in the form

$$Z^p = \frac{1}{N_g}\sum_{g\in G}\Gamma_c^p(g)A^p(\Gamma_c^p(g))^T. \tag{A.1}$$

Then, Property 1 follows from a direct computation.

Properties 2 and 3: For any arbitrary $g' \in G$, we have

$$\begin{aligned}
\Gamma_c^p(g')Z^p(\Gamma_c^p(g'))^T &= \Gamma_c^p(g')\frac{1}{N_g}\sum_{g\in G}\Gamma_c^p(g)A^p(\Gamma_c^p(g))^T(\Gamma_c^p(g'))^T \\
&= \frac{1}{N_g}\sum_{g\in G}[\Gamma_c^p(g')\Gamma_c^p(g)]A^p[\Gamma_c^p(g')\Gamma_c^p(g))]^T \\
&= \frac{1}{N_g}\sum_{g\in G}\Gamma_c^p(g'g)A^p(\Gamma_c^p(g'g))^T \\
&= \frac{1}{N_g}\sum_{g\in G}\Gamma_c^p(g)A^p(\Gamma_c^p(g))^T \\
&= Z^p
\end{aligned} \tag{A.2}$$

where the forth equivalence follows from the Rearrangement Theorem [28, Theorem II, p. 24]. Because the irrep is unitary, rearranging Eq. A.2 gives $\Gamma_c^p(g')Z^p = Z^p(\Gamma_c^p(g'))^*$. Because g' is arbitrary,

$$\Gamma_c^p(g)Z^p = Z^p(\Gamma_c^p(g))^*, \text{ for all } g \in G. \tag{A.3}$$

Property 2 follows from Ref. [28, Theorem II, p. 128] because the irrep Γ_c^p is potentially real.

Note that both Γ_c^p and $(\Gamma_c^p)^*$ are unitary irreps of dimension d_p of the group G. Schur's Lemma [28, Theorem I, p. 80] applied to Eq. A.3 implies that either

$Z^p = 0$ or $\det Z^p \neq 0$. Because of the assumption $Z^p \neq 0$, Z^p is nonsingular. Therefore, Z^p is a similarity transform from $\Gamma_c^p(g)$ to $(\Gamma_c^p(g))^*$ for all $g \in G$ which proves Property 3. □

Proof of Lemma 3. For simplicity, let $Q_1 = \mathfrak{R}Q$ and $Q_2 = \mathfrak{I}Q$.

Property 1: The matrices Q_1, Q_2, and B are all real and symmetric. Since $B \in \mathbb{R}^{2n\times 2n}$ and $B^T = B$, B has $2n$ real eigenvalues (possibly repeated) and $2n$ real orthonormal eigenvectors [59, Theorem 2.5.6, p. 104]. Define M by

$$M = \begin{bmatrix} I & -iI \\ 0 & I \end{bmatrix} B \begin{bmatrix} I & 0 \\ iI & I \end{bmatrix} = \begin{bmatrix} 0 & Q_2 + iQ_1 \\ Q_2 - iQ_1 & -Q_1 \end{bmatrix}.$$

Then,

$$\det(B) = \det(M) = \det((Q_2 + iQ_1)(Q_2 - iQ_1) - 0(-Q_1) = \det(QQ^*) = |\det(Q)|^2 > 0$$

because Q is non-singular. Hence, B is non-singular.

Property 2:

$$B\begin{bmatrix} x \\ -y \end{bmatrix} = \lambda \begin{bmatrix} x \\ -y \end{bmatrix}$$

$$\iff \begin{cases} Q_1 x - Q_2 y &= \lambda x \\ Q_2 x + Q_1 y &= -\lambda y \end{cases} \iff \begin{cases} Q_2 y - Q_1 x &= -\lambda x \\ Q_2 x + Q_1 y &= -\lambda y \end{cases}$$

$$\iff B\begin{bmatrix} x \\ y \end{bmatrix} = -\lambda \begin{bmatrix} x \\ y \end{bmatrix}.$$

Property 3: Define the matrices

$$\begin{aligned} X &= [x_1, \ldots, x_n] \in \mathbb{R}^{n\times n} \\ Y &= [y_1, \ldots, y_n] \in \mathbb{R}^{n\times n} \\ \Lambda &= \operatorname{diag}(\lambda_1, \ldots, \lambda_n) \in \mathbb{R}^{n\times n} \\ U &= X - iY \in \mathbb{C}^{n\times n}. \end{aligned} \tag{A.4}$$

The equation

$$B\left[\begin{smallmatrix} x_k \\ -y_k \end{smallmatrix}\right] = \lambda_k \left[\begin{smallmatrix} x_k \\ -y_k \end{smallmatrix}\right] \text{ for } k\{1, \ldots, n\}$$

is equivalent to

$$B\begin{bmatrix} X \\ -Y \end{bmatrix} = \begin{bmatrix} Q_1 & Q_2 \\ Q_2 & -Q_1 \end{bmatrix}\begin{bmatrix} X \\ -Y \end{bmatrix} = \begin{bmatrix} X \\ -Y \end{bmatrix}\Lambda$$

which is equivalent to $\begin{cases} Q_1X - Q_2Y &= X\Lambda \\ Q_2X + Q_1Y &= -Y\Lambda \end{cases}$.

Multiplying the second equation by i and adding to the first equation gives

$$\begin{aligned} U\Lambda &= (X - iY)\Lambda = (Q_1X - Q_2Y) + i(Q_2X + Q_1Y) \\ &= (Q_1 + iQ_2)X + (iQ_1 - Q_2)Y = (Q_1 + iQ_2)X + (Q_1 + iQ_2)iY \\ &= (Q_1 + iQ_2)(X + iY) = QU^*. \end{aligned}$$

Therefore $x_k - iy_k$ and $+\lambda_k$ are the coneigenvectors and coneigenvalues of Q, respectively.

Property 4: Because $QQ^* = I_n$ by assumption, the eigenvalues of QQ^* are the eigenvalues of I_n which all have value 1. By Ref. [59, Proposition 4.6.6, p. 246], ξ is an eigenvalue of QQ^* if and only if $+\sqrt{\xi}$ is a coneigenvalue of Q. Therefore, all the coneigenvalues of Q have value 1.

Property 5: Let the columns of $V \in \mathbb{R}^{2n\times 2n}$ be the $2n$ real orthonormal eigenvectors of B, i.e.,

$$V = \left[\begin{bmatrix} x_1 \\ -y_1 \end{bmatrix}, \ldots, \begin{bmatrix} x_n \\ -y_n \end{bmatrix}, \begin{bmatrix} y_1 \\ x_1 \end{bmatrix}, \ldots, \begin{bmatrix} y_n \\ x_n \end{bmatrix}\right]. \tag{A.5}$$

Then, $V^TV = VV^T = I_{2n}$ and $V^HV = VV^H = I_{2n}$.

Define $L \in \mathbb{C}^{n\times 2n}$ by $L = [I_n, iI_n]$ and $\tilde{U} \in \mathbb{C}^{2\times 2n}$ by $\tilde{U} = LV$. Then $\tilde{U}\tilde{U}^H = (LV)(LV)^H = LVV^HL^H = LI_{2n}L^H = LL^H = I_n + I_n = 2I_n$. But also, $\tilde{U} = LV = [x_1 - iy_1, \ldots, x_n - iy_n, y_1 + ix_1, \ldots, y_n + ix_n] = [x_1 - iy_1, \ldots, x_n - iy_n, i(x_1 - iy_1), \ldots, i(x_n - iy_n)] = [U, iU]$ and $\tilde{U}\tilde{U}^H = [U, iU]\begin{bmatrix} U^H \\ -iU^H \end{bmatrix} = UU^H + UU^H = 2UU^H$. Therefore, $UU^H = I_n$.

Property 6: Property 6 follows immediately from Properties 3–5 since Property 3 states that $QU^* = U\Lambda$, Property 4 states that $\Lambda = I_n$, and Property 5 states that $(U^*)^{-1} = U^T$. □

Lemma 6. *If all reps of a finite group G that is a subgroup of SO_3 are potentially real, then the union over reps of the group G of the set of real-valued basis functions that transform as a particular rep is a complete orthonormal system on the surface of the sphere. Equivalently, given $l \in \mathbb{N}$, the orthonormal functions $\{\{\{F_{p,l,n,j}(\theta,\phi)\}_{j=1}^{d_p}\}_{n=1}^{N_{p;l}}\}_{p=1}^{N_{\text{rep}}}$ span the subspace of square-integrable functions on the surface of the sphere defined by degree l, i.e., $\sum_{p=1}^{N_{\text{rep}}} d_p N_{p;l} = 2l + 1$.*

Proof of Lemma 6. The union of the sets of basis functions that transform according to the pth irrep of a finite group G over all values of p are a complete basis for square-integrable functions on the surface of the sphere in $\mathbb{R}^3$ [28, Theorem I, p. 92]. In addition, the basis functions computed by the projection operator approach (Eq. 5.12) are guaranteed to have [28, Theorem II, p. 93]

$$\begin{aligned}\int \left[\mathcal{P}^p_{j,k}\check{Y}_{l,m}(\mathbf{x})\right]\left[\mathcal{P}^{p'}_{j',k'}\check{Y}_{l',m'}(\mathbf{x})\right]d\mathbf{x} &= \delta_{p,p'}\delta_{k,j'}\int \left[\mathcal{P}^p_{j,k'}\check{Y}_{l,m}(\mathbf{x})\right]\check{Y}_{l',m'}(\mathbf{x})d\mathbf{x} \\ &= \delta_{p,p'}\delta_{k,j'}\delta_{l,l'}\delta_{m,m'}.\end{aligned}$$

Therefore, basis functions $F_{p,l,n,j}$ with different values of p, i.e., from different reps, are orthogonal. □

A.2 Relationships between icosahedral $d_p = 3$ irreps

Let R_g be the rotation matrices of Ref. [144] which are also a real orthonormal irrep of dimension 3. Let $\Gamma^p(g)$ be the complex unitary irreps of Ref. [80] where $p = 2$ and $p = 3$ are of dimension 3. With different permutations, R_g can be made similar to both $\Gamma^{p=2}(g)$ and $\Gamma^{p=3}(g)$. In particular, $\Gamma^p(g) = (S^p)^H R_{\gamma^p(g)} S^p$ for $p \in \{2, 3\}$ where the permutation $\gamma^p(g)$ and the complex unitary matrices $S^p \in \mathbb{C}^{3\times3}$ are given in Table A.1 and Eq. A.6, respectively.

$$S^{p=2} = \begin{bmatrix} -1/\sqrt{2} & 0 & -1/\sqrt{2} \\ -i/\sqrt{2} & 0 & i/\sqrt{2} \\ 0 & 1 & 0 \end{bmatrix} \quad S^{p=3} = \begin{bmatrix} -1/\sqrt{2} & 0 & -1/\sqrt{2} \\ i/\sqrt{2} & 0 & -i/\sqrt{2} \\ 0 & 1 & 0 \end{bmatrix}. \tag{A.6}$$

g	1	2	3	4	5	6	7	8	9	10
$\gamma^2(g)$	1	2	5	9	17	10	27	13	21	18
$\gamma^3(g)$	1	4	3	36	52	38	42	49	60	54
g	11	12	13	14	15	16	17	18	19	20
$\gamma^2(g)$	24	15	26	3	4	48	45	56	54	49
$\gamma^3(g)$	56	48	45	2	5	24	18	15	26	21
g	21	22	23	24	25	26	27	28	29	30
$\gamma^2(g)$	60	36	52	42	38	14	16	47	40	46
$\gamma^3(g)$	13	10	27	17	9	46	55	22	8	25
g	31	32	33	34	35	36	37	38	39	40
$\gamma^2(g)$	55	41	53	20	29	6	12	57	39	8
$\gamma^3(g)$	28	20	29	53	41	40	47	12	6	39
g	41	42	43	44	45	46	47	48	49	50
$\gamma^2(g)$	22	44	58	28	25	11	31	59	33	30
$\gamma^3(g)$	57	16	14	44	58	50	31	11	32	43
g	51	52	53	54	55	56	57	58	59	60
$\gamma^2(g)$	19	43	35	34	37	23	7	50	32	51
$\gamma^3(g)$	51	19	33	35	7	59	37	23	34	30

Table A.1: Permutations relating the 3 dimensional icosahedral irreps of Refs. [144, 80].

APPENDIX B

APPENDIX OF CHAPTER 6

B.1 Derivation of Eq. 6.7

The orthonormal condition of angular basis functions $I_{p;l,n}$ (Property 2 in Section 6.2) explicitly is

$$\int_{\theta=0}^{\pi}\int_{\phi=0}^{2\pi} I^T_{p;l,n}(\mathbf{x}/x) I_{p';l',n'}(\mathbf{x}/x)\mathrm{d}\theta\mathrm{d}\phi = I_{d_p}\delta_{p,p'}\delta_{l,l'}\delta_{n,n'}, \tag{B.1}$$

where $\mathbf{x}/x$ is shorthand for (θ,ϕ) (Section 5.1). By Eq. B.1 and Eq. 6.6 (the orthonomality of radial basis functions), the LHS of 6.7 can be expressed as

$$\begin{aligned}
&\int_{\mathbf{x}} F_{p;\zeta}(\mathbf{x}) F^T_{p';\zeta'}(\mathbf{x})\mathrm{d}\mathbf{x} \\
&= \int_{\mathbf{x}} \Big(I_{p;l,n}(\mathbf{x}/x)h_{l,q}(x)\Big)\Big(I_{p';l',n'}(\mathbf{x}/x)h_{l',q'}(x)\Big)^T \mathrm{d}\mathbf{x} \\
&= \int_{\theta=0}^{\pi}\int_{\phi=0}^{2\pi}\int_{x=0}^{\infty} \Big(I_{p;l,n}(\mathbf{x}/x)h_{l,q}(x)\Big)\Big(I_{p';l',n'}(\mathbf{x}/x)h_{l',q'}(x)\Big)^T \mathrm{d}x\mathrm{d}\phi\mathrm{d}\theta \\
&= \int_{\theta=0}^{\pi} I_{p;l,n}(\mathbf{x}/x)\left(\int_{\phi=0}^{2\pi} h_{l,q}(x)h^T_{l',q'}(x)\mathrm{d}x\right) I^T_{p';l',n'}(\mathbf{x}/x)\mathrm{d}\phi\mathrm{d}\theta \\
&= \Big(\delta_{l,l'}\delta_{q,q'}\Big)\int_{\theta=0}^{\pi} I_{p;l,n}(\mathbf{x}/x) I^T_{p';l,n'}(\mathbf{x}/x)\mathrm{d}\phi\mathrm{d}\theta \\
&= I_{d_p}\delta_{p,p'}\delta_{l,l'}\delta_{n,n'}\delta_{q,q'} \\
&= I_{d_p}\delta_{p,p'}\delta_{\zeta,\zeta'}
\end{aligned} \tag{B.2}$$

BIBLIOGRAPHY

[1] The octahedral group tables. http://www.cryst.ehu.es/cgi-bin/rep/programs/sam/point.py?sg=207&num=30. Accessed: 2015-06-03.

[2] The tetrahedral group tables. http://www.cryst.ehu.es/cgi-bin/rep/programs/sam/point.py?sg=195&num=28. Accessed: 2015-06-03.

[3] Hirotugu Akaike. Statistical predictor identification. *Annals of the Institute of Statistical Mathematics*, 22(1):203–217, 1970.

[4] Hirotugu Akaike. A new look at the statistical model identification. *IEEE Transactions on Automatic Control*, 19(6):716–723, December 1974.

[5] S. L. Altmann. On the symmetries of spherical harmonics. *Proc. Camb. Phil. Soc.*, 53:343–367, 1957.

[6] S. L. Altmann and C. J. Bradley. The band structure of hexagonal close-packed metals: I. The cellular method. *Proceedings of the Physical Society*, 86(5):915, 1965.

[7] S. L. Altmann and A. P. Cracknell. Lattice harmonics I. Cubic groups. *Rev. Mod. Phys.*, 37:19–32, Jan 1965.

[8] Mark A. Armstrong. *Groups and Symmetry*. Springer, 1997.

[9] Mois I. Aroyo, Asen Kirov, Cesar Capillas, J. M. Perez-Mato, and Hans Wondratschek. Bilbao crystallographic server. II. Representations of crystallographic point groups and space groups. *Acta Cryst.*, A62:115–128, 2006. http://dx.doi.org/10.1107/S0108767305040286.

[10] F Babiloni, Febo Cincotti, C Babiloni, F Carducci, D Mattia, Laura Astolfi, A Basilisco, PM Rossini, L Ding, Yicheng Ni, et al. Estimation of the cortical functional connectivity with the multimodal integration of high-resolution eeg and fmri data by directed transfer function. *Neuroimage*, 24(1):118–131, 2005.

[11] Xiao-chen Bai, Greg McMullan, and Sjors H. W. Scheres. How cryo-EM is revolutionizing structural biology. *Trends in Biochemical Sciences*, 40(1):49–57, January 2015. http://dx.doi.org/10.1016/j.tibs.2014.10.005.

[12] T. S. Baker, N. H. Olson, and S. D. Fuller. Adding the third dimension to virus life cycles: Three-dimensional reconstruction of icosahedral viruses from cryo-electron micrographs. *Microbiology and Molecular Biology Reviews*, 63(4):862–922, December 1999.

[13] Samuel Baron. *Epidemiology–Medical Microbiology*. University of Texas Medical Branch at Galveston, 1996.

[14] Danielle S Bassett and Michael S Gazzaniga. Understanding complexity in the human brain. *Trends in cognitive sciences*, 15(5):200–209, 2011.

[15] Bharat Biswal, F Zerrin Yetkin, Victor M Haughton, and James S Hyde. Functional connectivity in the motor cortex of resting human brain using echo-planar mri. *Magnetic resonance in medicine*, 34(4):537–541, 1995.

[16] Bharat B Biswal, Maarten Mennes, Xi-Nian Zuo, Suril Gohel, Clare Kelly, Steve M Smith, Christian F Beckmann, Jonathan S Adelstein, Randy L Buckner, Stan Colcombe, et al. Toward discovery science of human brain

function. *Proceedings of the National Academy of Sciences*, 107(10):4734–4739, 2010.

[17] KJ Blinowska, B Trzaskowski, M Kaminski, and R Kus. Multivariate autoregressive model for a study of phylogenetic diversity. *Gene*, 435(1):104–118, 2009.

[18] Richard B Buxton and Lawrence R Frank. A model for the coupling between cerebral blood flow and oxygen metabolism during neural stimulation. *Journal of Cerebral Blood Flow & Metabolism*, 17(1):64–72, 1997.

[19] Richard B Buxton, Eric C Wong, and Lawrence R Frank. Dynamics of blood flow and oxygenation changes during brain activation: the balloon model. *Magnetic resonance in medicine*, 39(6):855–864, 1998.

[20] D. L. D. Caspar and A. Klug. Physical principles in the construction of regular viruses. *Cold Spring Harbor Symposium on Quantitative Biology*, 27:1–24, 1962.

[21] Joseph E Cavanaugh. Unifying the derivations for the Akaike and corrected Akaike information criteria. *Statistics & Probability Letters*, 33(2):201–208, 1997.

[22] Gang Chen, Daniel R Glen, Ziad S Saad, J Paul Hamilton, Moriah E Thomason, Ian H Gotlib, and Robert W Cox. Vector autoregression, structural equation modeling, and their synthesis in neuroimaging data analysis. *Computers in biology and medicine*, 41(12):1142–1155, 2011.

[23] Yifan Cheng. Single-particle cryo-EM at crystallographic resolution. *Cell*, 161:450–457, 23 Apr 2015. `http://dx.doi.org/10.1016/j.cell.2015.03.049`.

[24] Yifan Cheng, Nikolaus Grigorieff, Pawel A. Penczek, and Thomas Walz. A primer to single-particle cryo-electron microscopy. *Cell*, 161:438–449, 23 Apr 2015. http://dx.doi.org/10.1016/j.cell.2015.03.050.

[25] Norah V. Cohan. The spherical harmonics with the symmetry of the icosahedral group. *Proc. Camb. Phil. Soc.*, 54:28–38, 1958.

[26] Michael W Cole, Danielle S Bassett, Jonathan D Power, Todd S Braver, and Steven E Petersen. Intrinsic and task-evoked network architectures of the human brain. *Neuron*, 83(1):238–251, 2014.

[27] R. Conte, Jacques Raynal, and E. Soulie. Determination of point group harmonics for arbitrary j by a projection method. I. Cubic group, quantization along an axis of order 4. *J. Math. Phys.*, 25(5):1176–1186, May 1984.

[28] J. F. Cornwell. *Group Theory in Physics*, volume 1. Academic Press, London, 1984.

[29] Francis H. C. Crick and James D. Watson. Structure of small viruses. *Nature*, 177(4506):473–475, 1956. http://dx.doi.org/10.1038/177473a0.

[30] R. A. Crowther. *The Molecular Replacement Method: A Collection of Papers on the Use of Non-Crystallographic Symmetry*, chapter The Fast Rotation Function, pages 173–178. Gordon and Breach, 1972.

[31] J. Daunizeau, K.J. Friston, and S.J. Kiebel. Variational bayesian identification and prediction of stochastic nonlinear dynamic causal models. *Physica D: Nonlinear Phenomena*, 238(21):2089 – 2118, 2009.

[32] Justin Dauwels, François Vialatte, Toshimitsu Musha, and Andrzej Cichocki. A comparative study of synchrony measures for the early diagnosis of Alzheimer's disease based on eeg. *NeuroImage*, 49(1):668–693, 2010.

[33] Richard A Davis, Pengfei Zang, and Tian Zheng. Sparse vector autoregressive modeling. *Journal of Computational and Graphical Statistics*, (just-accepted):1–53, 2015.

[34] Debra Ann Dawson, Kuwook Cha, Lindsay B Lewis, Janine D Mendola, and Amir Shmuel. Evaluation and calibration of functional network modeling methods based on known anatomical connections. *NeuroImage*, 67:331–343, 2013.

[35] Mingzhou Ding, Steven L Bressler, Weiming Yang, and Hualou Liang. Short-window spectral analysis of cortical event-related potentials by adaptive multivariate autoregressive modeling: data preprocessing, model validation, and variability assessment. *Biological cybernetics*, 83(1):35–45, 2000.

[36] Peter C. Doerschuk and John E. Johnson. *Ab initio* reconstruction and experimental design for cryo electron microscopy. *IEEE Transactions on Information Theory*, 46(5):1714–1729, August 2000. `http://dx.doi.org/10.1109/18.857786`.

[37] L. Elcoro, J. M. Perez-Mato, and G. Madariaga. Determination of quasicrystalline structures: a refinement program using symmetry-adapted parameters. *Acta Cryst.*, A50:182–193, 1994.

[38] G. W. Fernando, M. Weinert, R. E. Watson, and J. W. Davenport. Point

group symmetries and Gaussian integration. *J. Computational Physics*, 112:282–290, 1994.

[39] Brett L. Foster, Vinitha Rangarajan, William R. Shirer, and Josef Parvizi. Intrinsic and task-dependent coupling of neuronal population activity in human parietal cortex. *Neuron*, 86(2):578–590, 2015.

[40] Kenneth Fox and Irving Ozier. Construction of tetrahedral harmonics. *The Journal of Chemical Physics*, 52(10):5044–5056, 1970.

[41] Michael D Fox, Abraham Z Snyder, Justin L Vincent, Maurizio Corbetta, David C Van Essen, and Marcus E Raichle. The human brain is intrinsically organized into dynamic, anticorrelated functional networks. *Proceedings of the National Academy of Sciences of the United States of America*, 102(27):9673–9678, 2005.

[42] Joachim Frank, Michael Radermacher, Pawel Penczek, Jun Zhu, Yanhong Li, Maheiddine Ladjadj, and Ardean Leith. SPIDER and WEB: Processing and visualization of images in 3D electron microscopy and related fields. *J. Struct. Biol.*, 116:190–199, 1996.

[43] Karl J Friston. Functional and effective connectivity: A review. *Brain Connectivity*, 1(1):13–36, 2011.

[44] Karl J Friston, Lee Harrison, and Will Penny. Dynamic causal modelling. *Neuroimage*, 19(4):1273–1302, 2003.

[45] Karl J Friston, Andrea Mechelli, Robert Turner, and Cathy J Price. Nonlinear responses in fmri: the balloon model, volterra kernels, and other hemodynamics. *NeuroImage*, 12(4):466–477, 2000.

[46] William Fulton. *Young tableaux: with applications to representation theory and geometry*, volume 35. Cambridge University Press, 1997.

[47] Kathleen M Gates and Peter CM Molenaar. Group search algorithm recovers effective connectivity maps for individuals in homogeneous and heterogeneous samples. *Neuroimage*, 63(1):310–319, 2012.

[48] Linda Geerligs, Richard N Henson, et al. Functional connectivity and structural covariance between regions of interest can be measured more accurately using multivariate distance correlation. *NeuroImage*, 135:16–31, 2016.

[49] Ilya Gertsman, Lu Gan, Miklos Guttman, Kelly Lee, Jeffrey A Speir, Robert L Duda, Roger W Hendrix, Elizabeth A Komives, and John E Johnson. An unexpected twist in viral capsid maturation. *Nature*, 458(7238):646–650, 2009.

[50] Gene H. Golub and Charles F. Van Loan. *Matrix Computations*. The Johns Hopkins University Press, Baltimore, 3nd edition, 2013.

[51] Yunye Gong, David Veesler, Peter C. Doerschuk, and John E. Johnson. Effect of the viral protease on the dynamics of bacteriophage HK97 maturation intermediates characterized by variance analysis of cryo EM particle ensembles. *Journal of Structural Biology*, 193(3):188–195, March 2016.

[52] Evan M Gordon, Andrew L Breeden, Stephanie E Bean, and Chandan J Vaidya. Working memory-related changes in functional connectivity persist beyond task disengagement. *Human brain mapping*, 35(3):1004–1017, 2014.

[53] Evan M Gordon, Timothy O Laumann, Babatunde Adeyemo, Jeremy F Huckins, William M Kelley, and Steven E Petersen. Generation and evaluation of a cortical area parcellation from resting-state correlations. *Cerebral cortex*, 26(1):288–303, 2016.

[54] Michael D Greicius, Ben Krasnow, Allan L Reiss, and Vinod Menon. Functional connectivity in the resting brain: a network analysis of the default mode hypothesis. *Proceedings of the National Academy of Sciences*, 100(1):253–258, 2003.

[55] George Harauz and Marin van Heel. Exact filters for general geometry three dimensional reconstruction. *Optik*, 73(4):146–156, 1986.

[56] Karl T. Hecht. Vibration-rotation energies of tetrahedral XY4 molecules. *Journal of Molecular Spectroscopy*, 5(1):390–404, 1961.

[57] Eberhard Heuser-Hofmann and Wolf Weyrich. Three-dimensional reciprocal form factors and momentum densities of electrons from Compton experiments: I. Symmetry-adapted series expansion of the electron momentum density. *Z. Naturforsch.*, 40a:99–111, 1985.

[58] Joerg F Hipp and Markus Siegel. Bold fMRI correlation reflects frequency-specific neuronal correlation. *Current Biology*, 25(10):1368–1374, 2015.

[59] Roger A. Horn and Charles R. Johnson. *Matrix Analysis*. Cambridge University Press, 1985.

[60] Rick K Huang, Reza Khayat, Kelly K Lee, Ilya Gertsman, Robert L Duda, Roger W Hendrix, and John E Johnson. The prohead-i structure of bacteriophage hk97: implications for scaffold-mediated control of particle assembly and maturation. *Journal of molecular biology*, 408(3):541–554, 2011.

[61] Clifford M Hurvich and Chih-Ling Tsai. Regression and time series model selection in small samples. *Biometrika*, 76(2):297–307, 1989.

[62] Clifford M Hurvich and Chih-Ling Tsai. A corrected Akaike information criterion for vector autoregressive model selection. *Journal of time series analysis*, 14(3):271–279, 1993.

[63] Aapo Hyvärinen and Stephen M Smith. Pairwise likelihood ratios for estimation of non-gaussian structural equation models. *The Journal of Machine Learning Research*, 14(1):111–152, 2013.

[64] A. Jack and S. C. Harrison. On the interpretation of small-angle x-ray solution scattering from spherical viruses. *J. Mol. Biol.*, 99:15–25, 1975.

[65] H. A. Jahn. A new coriolis perturbation in the methane spectrum. I. Vibrational-rotational hamiltonian and wave functions. *Proceedings of the Royal Society of London A: Mathematical, Physical and Engineering Sciences*, 168(935):469–495, 1938.

[66] Grant J. Jensen, editor. *Cryo-EM, Parts A–C*, volume 481–483 of *Methods in Enzymology*. Elsevier Inc., 2010.

[67] Hang Joon Jo, Stephen J. Gotts, Richard C. Reynolds, Peter A. Bandettini, Alex Martin, Robert W. Cox, and Ziad S. Saad. Effective preprocessing procedures virtually eliminate distance-dependent motion artifacts in resting state fmri. *J. Applied Mathematics*, 2013:935154:1–935154:9, 2013.

[68] John E Johnson. Virus particle maturation: insights into elegantly programmed nanomachines. *Current opinion in structural biology*, 20(2):210–216, 2010.

[69] Mikko Kara and Kaarle Kurki-Suonio. Symmetrized multipole analysis of orientational distributions. *Acta Cryst.*, A37:201–210, 1981.

[70] Jieun Kim, Wei Zhu, Linda Chang, Peter M Bentler, and Thomas Ernst. Unified structural equation modeling approach for the analysis of multisubject, multivariate functional MRI data. *Human Brain Mapping*, 28(2):85–93, 2007.

[71] Anna Korzeniewska, Piotr J Franaszczuk, Ciprian M Crainiceanu, Rafał Kuś, and Nathan E Crone. Dynamics of large-scale cortical interactions at high gamma frequencies during word production: event related causality (erc) analysis of human electrocorticography (ecog). *Neuroimage*, 56(4):2218–2237, 2011.

[72] Rafal Kus, Maciej Kaminski, and Katarzyna J Blinowska. Determination of eeg activity propagation: pair-wise versus multichannel estimate. *IEEE transactions on Biomedical Engineering*, 51(9):1501–1510, 2004.

[73] Juha M Lahnakoski, Enrico Glerean, Juha Salmi, Iiro P Jääskeläinen, Mikko Sams, Riitta Hari, and Lauri Nummenmaa. Naturalistic fmri mapping reveals superior temporal sulcus as the hub for the distributed brain network for social perception. *Frontiers in human neuroscience*, 6, 2012.

[74] Andrea Lancichinetti and Santo Fortunato. Community detection algorithms: A comparative analysis. *Phys. Rev. E*, 80:056117, Nov 2009.

[75] Otto Laporte. Polyhedral harmonics. *Z. Naturforschg.*, 3a:447–456, 1948.

[76] Timothy O Laumann, Evan M Gordon, Babatunde Adeyemo, Abraham Z Snyder, Sung Jun Joo, Mei-Yen Chen, Adrian W Gilmore, Kathleen B McDermott, Steven M Nelson, Nico UF Dosenbach, et al. Functional system

and areal organization of a highly sampled individual human brain. *Neuron*, 87(3):657–670, 2015.

[77] Junghoon Lee, Peter C. Doerschuk, and John E. Johnson. Exact reduced-complexity maximum likelihood reconstruction of multiple 3-D objects from unlabeled unoriented 2-D projections and electron microscopy of viruses. *IEEE Transactions on Image Processing*, 16(11):2865–2878, November 2007. http://www.ncbi.nlm.nih.gov/pubmed/18092587.

[78] Tomasz S Ligeza, Miroslaw Wyczesany, Agnieszka D Tymorek, and Maciej Kamiński. Interactions between the prefrontal cortex and attentional systems during volitional affective regulation: an effective connectivity reappraisal study. *Brain topography*, 29(2):253–261, 2016.

[79] Martin A Lindquist, Ji Meng Loh, Lauren Y Atlas, and Tor D Wager. Modeling the hemodynamic response function in fmri: efficiency, bias and mis-modeling. *Neuroimage*, 45(1):S187–S198, 2009.

[80] Fa Liu, Jia-Lun Ping, and Jin-Quan Chen. Application of the eigenfunction method to the icosahedral group. *J. Math. Phys.*, 31(5):1065–1075, 1990.

[81] S. J. Ludtke, P. R. Baldwin, and W. Chiu. EMAN: semiautomated software for high-resolution single-particle reconstructions. *J. Struct. Biol.*, 128(1):82–97, Dec. 1 1999.

[82] SJ Ludtke. Chapter seven-single-particle refinement and variability analysis in eman2. 1. *Methods in Enzymology*, 579:159–189, 2016.

[83] Daniel Marcus, John Harwell, Timothy Olsen, Michael Hodge, Matthew Glasser, Fred Prior, Mark Jenkinson, Timothy Laumann, Sandra Curtiss,

and David Van Essen. Informatics and data mining tools and strategies for the human connectome project. *Frontiers in neuroinformatics*, 5:4, 2011.

[84] Burnett Meyer. On the symmetries of spherical harmonics. *Canadian J. Math.*, 135:135–157, 1954.

[85] R Chris Miall and Edwin M Robertson. Functional imaging: is the resting brain resting? *Current Biology*, 16(23):R998–R1000, 2006.

[86] Anish Mitra, Abraham Z. Snyder, Tyler Blazey, and Marcus E. Raichle. Lag threads organize the brain's intrinsic activity. *Proceedings of the National Academy of Sciences of the United States of America*, 112(17):E2235–E2244, April 2015.

[87] Philip M. Morse and Herman Feshbach. *Methods of Theoretical Physics*. McGraw-Hill, New York, 1953.

[88] F. M. Mueller and M. G. Priestley. Inversion of cubic de Haas-van Alphen data, with an application to palladium. *Phys. Rev.*, 148:638–643, Aug 1966.

[89] Jürg Muggli. Cubic harmonics as linear combinations of spherical harmonics. *Zeitschrift für angewandte Mathematik und Physik ZAMP*, 23(2):311–317, 1972.

[90] Jeanette A Mumford and Joseph D Ramsey. Bayesian networks for fMRI: a primer. *Neuroimage*, 86:573–582, 2014.

[91] Kevin Murphy, Rasmus M. Birn, Daniel A. Handwerker, Tyler B. Jones, and Peter A. Bandettini. The impact of global signal regression on resting state correlations: Are anti-correlated networks introduced? *NeuroImage*, 44(3):893–905, 2009.

[92] Frank W. J. Olver, Daniel W. Lozier, Ronald F. Boisvert, and Charles W. Clark. *NIST Handbook of Mathematical Functions*. Cambridge University Press, Cambridge, UK, 2010.

[93] Frank W. J. Olver, Daniel W. Lozier, Ronald F. Boisvert, and Charles W. Clark, editors. *NIST Handbook of Mathematical Functions*. Cambridge University Press, Cambridge, UK, 2010.

[94] H Desmond Patterson and Robin Thompson. Recovery of inter-block information when block sizes are unequal. *Biometrika*, 58(3):545–554, 1971.

[95] E. F. Pettersen, T. D. Goddard, C. C. Huang, G. S. Couch, D. M. Greenblatt, E. C. Meng, and T. E. Ferrin. UCSF Chimera—A visualization system for exploratory research and analysis. *J. Comput. Chem.*, 25(13):1605–1612, 2004.

[96] Jonathan D Power, Kelly A Barnes, Abraham Z Snyder, Bradley L Schlaggar, and Steven E Petersen. Spurious but systematic correlations in functional connectivity MRI networks arise from subject motion. *Neuroimage*, 59(3):2142–2154, 2012.

[97] Jonathan D Power, Alexander L Cohen, Steven M Nelson, Gagan S Wig, Kelly Anne Barnes, Jessica A Church, Alecia C Vogel, Timothy O Laumann, Fran M Miezin, Bradley L Schlaggar, et al. Functional network organization of the human brain. *Neuron*, 72(4):665–678, 2011.

[98] Jonathan D Power, Bradley L Schlaggar, Christina N Lessov-Schlaggar, and Steven E Petersen. Evidence for hubs in human functional brain networks. *Neuron*, 79(4):798–813, 2013.

[99] H. Puff. Contribution to the theory of cubic harmonics. *Physica Status Solidi (B)*, 41(1):11–22, 1970.

[100] Dale Purves, Roberto Cabeza, Scott A Huettel, Kevin S LaBar, Michael L Platt, Marty G Woldorff, and Elizabeth M Brannon. *Cognitive Neuroscience*. Sunderland: Sinauer Associates, Inc, 2008.

[101] Joseph D Ramsey, Stephen José Hanson, and Clark Glymour. Multi-subject search correctly identifies causal connections and most causal directions in the dcm models of the smith et al. simulation study. *NeuroImage*, 58(3):838–848, 2011.

[102] Joseph D Ramsey, Stephen José Hanson, Catherine Hanson, Yaroslav O Halchenko, Russell A Poldrack, and Clark Glymour. Six problems for causal inference from fMRI. *Neuroimage*, 49(2):1545–1558, 2010.

[103] Jacques Raynal and Robert Conte. Determination of point group harmonics for arbitrary j by a projection method. III. Cubic group, quantization along a ternary axis. *J. Math. Phys.*, 25(12):3375–3381, December 1984.

[104] Richard A. Redner and Homer F. Walker. Mixture densities, maximum likelihood and the EM algorithm. *SIAM Review*, 26(2):195–239, April 1984.

[105] Jorma Rissanen. Modeling by shortest data description. *Automatica*, 14(5):465–471, 1978.

[106] Morris E. Rose. *Elementary Theory of Angular Momentum*. John Wiley and Sons, New York, 1957.

[107] Srikanth Ryali, Tianwen Chen, Kaustubh Supekar, Tao Tu, John Kochalka, Weidong Cai, and Vinod Menon. Multivariate dynamical systems-based

estimation of causal brain interactions in fmri: Group-level validation using benchmark data, neurophysiological models and human connectome project data. *Journal of neuroscience methods*, 268:142–153, 2016.

[108] Ziad S. Saad, Stephen J. Gotts, Kevin Murphy, Gang Chen 0008, Hang Joon Jo, Alex Martin, and Robert W. Cox. Trouble at rest: How correlation patterns and group differences become distorted after global signal regression. *Brain Connectivity*, 2(1):25–32, 2012.

[109] Sepideh Sadaghiani, Jean-Baptiste Poline, Andreas Kleinschmidt, and Mark DEsposito. Ongoing dynamics in large-scale functional connectivity predict perception. *Proceedings of the National Academy of Sciences*, 112(27):8463–8468, 2015.

[110] Alexander Schaefer, Daniel S Margulies, Gabriele Lohmann, Krzysztof J Gorgolewski, Jonathan Smallwood, Stefan J Kiebel, and Arno Villringer. Dynamic network participation of functional connectivity hubs assessed by resting-state fMRI. *Frontiers in human neuroscience*, 8, 2014.

[111] Björn Schelter, Matthias Winterhalder, and Jens Timmer. *Handbook of time series analysis: recent theoretical developments and applications*. John Wiley & Sons, 2006.

[112] Sjors H. W. Scheres. RELION: Implementation of a Bayesian approach to cryo-EM structure determination. *J. Struct. Biol.*, 180:519–530, 2012.

[113] Sjors H. W. Scheres, Haixiao Gao, Mikel Valle, Gabor T. Herman, Paul P. B. Eggermont, Joachim Frank, and Jose-Maria Carazo. Disentangling conformational states of macromolecules in 3D-EM through likelihood optimization. *Nature Methods*, 4(1):27–29, January 2007.

[114] Gideon Schwarz. Estimating the dimension of a model. *The Annals of Statistics*, 6(2):461–464, 1978.

[115] Tanvir R Shaikh, Haixiao Gao, William T Baxter, Francisco J Asturias, Nicolas Boisset, Ardean Leith, and Joachim Frank. Spider image processing for single-particle reconstruction of biological macromolecules from electron micrographs. *Nature protocols*, 3(12):1941–1974, 2008.

[116] Stephen M Smith. The future of fmri connectivity. *Neuroimage*, 62(2):1257–1266, 2012.

[117] Stephen M Smith, Karla L Miller, Gholamreza Salimi-Khorshidi, Matthew Webster, Christian F Beckmann, Thomas E Nichols, Joseph D Ramsey, and Mark W Woolrich. Network modelling methods for fMRI. *Neuroimage*, 54(2):875–891, 2011.

[118] Olaf Sporns. The human connectome: a complex network. *Annals of the New York Academy of Sciences*, 1224(1):109–125, 2011.

[119] W Dale Stevens, Randy L Buckner, and Daniel L Schacter. Correlated low-frequency bold fluctuations in the resting human brain are modulated by recent experience in category-preferential visual regions. *Cerebral cortex*, page bhp270, 2009.

[120] W Dale Stevens and R Nathan Spreng. Resting-state functional connectivity mri reveals active processes central to cognition. *Wiley Interdisciplinary Reviews: Cognitive Science*, 5(2):233–245, 2014.

[121] Nariaki Sugiura. Further analysts of the data by Akaike's information criterion and the finite corrections: Further analysts of the data by Akaike's. *Communications in Statistics-Theory and Methods*, 7(1):13–26, 1978.

[122] Arielle Tambini, Nicholas Ketz, and Lila Davachi. Enhanced brain correlations during rest are related to memory for recent experiences. *Neuron*, 65(2):280–290, 2010.

[123] Guang Tang, Liwei Peng, Philip R Baldwin, Deepinder S Mann, Wen Jiang, Ian Rees, and Steven J Ludtke. Eman2: an extensible image processing suite for electron microscopy. *Journal of structural biology*, 157(1):38–46, 2007.

[124] Jinghua Tang, Bradley M. Kearney, Qiu Wang, Peter C. Doerschuk, Timothy S. Baker, and John E. Johnson. Dynamic and geometric analyses of *Nudaurelia capensis* ω virus maturation reveal the energy landscape of particle transitions. *J. Molecular Recognition*, 27(4):230–237, 10 February 2014. `http://www.ncbi.nlm.nih.gov/pubmed/24591180`.

[125] WA Thompson Jr. The problem of negative estimates of variance components. *The Annals of Mathematical Statistics*, pages 273–289, 1962.

[126] Pedro A Valdés-Sosa, Jose M Sánchez-Bornot, Agustín Lage-Castellanos, Mayrim Vega-Hernández, Jorge Bosch-Bayard, Lester Melie-García, and Erick Canales-Rodríguez. Estimating brain functional connectivity with sparse multivariate autoregression. *Philosophical Transactions of the Royal Society B: Biological Sciences*, 360(1457):969–981, 2005.

[127] Martijn P Van Den Heuvel and Hilleke E Hulshoff Pol. Exploring the brain network: a review on resting-state fMRI functional connectivity. *European Neuropsychopharmacology*, 20(8):519–534, 2010.

[128] David C Van Essen, Kamil Ugurbil, E Auerbach, D Barch, TEJ Behrens, R Bucholz, A Chang, Liyong Chen, Maurizio Corbetta, Sandra W Cur-

tiss, et al. The human connectome project: a data acquisition perspective. *Neuroimage*, 62(4):2222–2231, 2012.

[129] Marin van Heel. Similarity measures between images. *Ultramicroscopy*, 21:95–100, 1987.

[130] David Veesler, Reza Khayat, Srinath Krishnamurthy, Joost Snijder, Rick K Huang, Albert JR Heck, Ganesh S Anand, and John E Johnson. Architecture of a dsdna viral capsid in complex with its maturation protease. *Structure*, 22(2):230–237, 2014.

[131] Christopher S Wallace and David M Boulton. An information measure for classification. *The Computer Journal*, 11(2):185–194, 1968.

[132] Huifang E Wang, Christian G Bénar, Pascale P Quilichini, Karl J Friston, Viktor K Jirsa, and Christophe Bernard. A systematic framework for functional connectivity measures. *Frontiers in neuroscience*, 8:405, 2014.

[133] Qiu Wang, Tsutomu Matsui, Tatiana Domitrovic, Yili Zheng, Peter C. Doerschuk, and John E. Johnson. Dynamics in cryo EM reconstructions visualized with maximum-likelihood derived variance maps. *J. Struct. Biol.*, 181(3):195–206, March 2013.

[134] Gagan S. Wig, Bradley L. Schlaggar, and Steven E. Petersen. Concepts and principles in the analysis of brain networks. *Annals of the New York Academy of Sciences*, 1224(1):126–146, 2011.

[135] Gagan S Wig, Bradley L Schlaggar, and Steven E Petersen. Concepts and principles in the analysis of brain networks. *Annals of the New York Academy of Sciences*, 1224(1):126–146, 2011.

[136] Christopher Wilke, Lei Ding, Bin He, et al. Estimation of time-varying connectivity patterns through the use of an adaptive directed transfer function. *IEEE transactions on biomedical engineering*, 55(11):2557–2564, 2008.

[137] Nan Xu and Peter C. Doerschuk. Reconstruction for stochastic 3-d signals with symmetric statistics in noise: Electron microscopy of virus particles. In *2015 IEEE International Conference on Image Processing, ICIP 2015, Quebec City, QC, Canada, September 27-30, 2015*, pages 1444–1447, 2015.

[138] Nan Xu and Peter C Doerschuk. Cryo electron microscopy: 3-d reconstruction of stochastic objects having statistics with geometric symmetry from 2-d noisy conditionally-linear imaging. *[submitted to] IEEE Transactions on Computational Imaging*, 2016.

[139] Nan Xu, R. Nathan Spreng, and Peter C. Doerschuk. Directed interactivity of large-scale brain networks: introducing a new method for estimating resting-state effective connectivity MRI. In *Image Processing (ICIP), 2014 21st IEEE International Conference on*, pages 3508–3512, Oct 2014.

[140] Nan Xu, R Nathan Spreng, and Peter C Doerschuk. Initial validation for the estimation of resting-state fmri effective connectivity by a generalization of the correlation approach. *Frontiers in Neuroscience*, 11:271, 2017.

[141] BT Thomas Yeo, Fenna M Krienen, Jorge Sepulcre, Mert R Sabuncu, Danial Lashkari, Marisa Hollinshead, Joshua L Roffman, Jordan W Smoller, Lilla Zöllei, Jonathan R Polimeni, et al. The organization of the human cerebral cortex estimated by intrinsic functional connectivity. *Journal of neurophysiology*, 106(3):1125–1165, 2011.

[142] Zhye Yin, Yili Zheng, Peter C. Doerschuk, Padmaja Natarajan, and John E. Johnson. A statistical approach to computer processing of cryo electron microscope images: Virion classification and 3-D reconstruction. *J. Struct. Biol.*, 144(1/2):24–50, 2003. http://www.ncbi.nlm.nih.gov/pubmed/14643207.

[143] Andrew Zalesky, Alex Fornito, and Ed Bullmore. On the use of correlation as a measure of network connectivity. *Neuroimage*, 60(4):2096–2106, 2012.

[144] Yibin Zheng and Peter C. Doerschuk. Symbolic symmetry verification for harmonic functions invariant under polyhedral symmetries. *Comput. in Phys.*, 9(4):433–437, July/August 1995.

[145] Yibin Zheng and Peter C. Doerschuk. Explicit orthonormal fixed bases for spaces of functions that are totally symmetric under the rotational symmetries of a Platonic solid. *Acta Cryst.*, A52:221–235, 1996.

[146] Yibin Zheng and Peter C. Doerschuk. 3D image reconstruction from averaged Fourier transform magnitude by parameter estimation. *IEEE Transactions on Image Processing*, 7(11):1561–1570, November 1998.

[147] Yibin Zheng and Peter C. Doerschuk. Explicit computation of orthonormal symmetrized harmonics with application to the identity representation of the icosahedral group. *SIAM Journal on Mathematical Analysis*, 32(3):538–554, 2000. http://dx.doi.org/10.1137/S0036141098341770.

[148] Yili Zheng, Qiu Wang, and Peter C. Doerschuk. 3-D reconstruction of the statistics of heterogeneous objects from a collection of one projection image of each object. *J. Opt. Soc. Am. A*, 29(6):959–970, June 2012.